HAL
open science

Fonctionnalisation de fibres optiques par des grenats pour les applications magnéto-optiques

Issatay Nadinov

To cite this version:

Issatay Nadinov. Fonctionnalisation de fibres optiques par des grenats pour les applications magnéto-optiques. Physics [physics]. Université de Strasbourg, 2019. English. NNT : 2019STRAE051 . tel-03157296

HAL Id: tel-03157296

https://theses.hal.science/tel-03157296v1

Submitted on 3 Mar 2021

HAL is a multi-disciplinary open access archive for the deposit and dissemination of scientific research documents, whether they are published or not. The documents may come from teaching and research institutions in France or abroad, or from public or private research centers.

L'archive ouverte pluridisciplinaire **HAL**, est destinée au dépôt et à la diffusion de documents scientifiques de niveau recherche, publiés ou non, émanant des établissements d'enseignement et de recherche français ou étrangers, des laboratoires publics ou privés.

UNIVERSITÉ DE STRASBOURG

ÉCOLE DOCTORALE DE PHYSIQUE ET CHIMIE-PHYSIQUE (182)

THÈSE présentée par :

Issatay NADINOV

soutenue le : **6 décembre 2019**

pour obtenir le grade de: **Docteur de l'université de Strasbourg**

Discipline/ Spécialité: Physique

Fonctionnalisation de fibres optiques par des grenats pour les applications magnéto-optiques

DIRECTEUR DE THÈSE :

MAGER Loïc	Chargé de recherche HDR, IPCMS (UMR 7504)

RAPPORTEURS :

ESTOURNES Claude	Directeur de recherche, CIRIMAT (UMR 5085)
ROYER François	Professeur, LHC (UMR 5516)

EXAMINATEURS :

CHARRIER Joël	Maître de Conférences HDR, FOTON (UMR 6082)
PETIT Corinne	Professeur, ICPEES (UMR 7515)

INVITES :

BERLING Dominique	Professeur, IS2M (UMR 7361)
REHSPRINGER Jean-Luc	Directeur de recherche, IPCMS (UMR 7504)

DEDICATION

This thesis is dedicated:

to my beautiful wife *Aliya*, my beautiful daughter *Jasmine,*

and to my brother *Bauyrzhan* and his family.

In the memory of my beloved parents *Urazbai Nadinov* and *Akhalam Nadinova*.

Thank you for your endless love, invaluable support during my whole life. You are the reasons for my becoming the person I am today. I love you.

Acknowledgment

I would like to express my sincere gratitude to my supervisor, Dr. Loïc Mager for his support during my Ph.D. studies and research. His patience, immense knowledge and enthusiasm have been motivating me during the whole project. This thesis and subsequent publications reflect his perfect guidance in this research. I cannot imagine having a better mentor than him for my graduate work.

Also, I would like to express my sincere gratitude to my co-supervisor, Dr. Jean-Luc Rehspringer for his teaching and assisting me in the chemical part of the project, specifically, in the preparation of Bi: YIG films and powders, as well as XRD and DTA analyses. Also, I need to thank him for the helpful suggestions and fruitful discussions during the whole project.

I would like to express my special thanks to Dr. Oleksandr Kovalenko and Dr. Mircea Vomir for fruitful discussions and support in the implementation of experiments I had to carry out. Many thanks to Dr. Alex Boeglin for helping me with my writing of the dissertation and for fruitful discussions.

In addition, I would like to thank IPCMS members: Mr. Cedric Leuvrey, who kindly helped me with SEM measurements and analyses of my experimental samples; Mr. Nicolas Beyer, who produced the iron core for the magnetic field generator and other parts of the experimental setup for magnetic field measurements.

Finally, I would like to acknowledge financial support from the French National Research Agency via the project FOGAMO [grant number: ANR-16-CE08-0014-01] and the project Equipex UNION [grant number: ANR-10-EQPX-52].

Content

General Introduction 17

Chapter 1 19

1.1. Magnetic sensing technology 19

1.1.1. Compass 19

1.1.2. Induction magnetometers 20

1.1.3. Hall Effect Sensors 21

1.1.4. Proton magnetometer 22

1.1.5. Optically pumped magnetometer 22

1.1.6. Magnetoresistive sensors 23

1.1.7. Superconducting Quantum Interference Device (SQUID) sensors 25

1.2. Magneto optical (MO) sensors 26

1.2.1. Magnetostrictive sensors 26

1.2.2. Terfenol-D 27

1.2.3. Magnetic Fluid 27

1.2.4. Magneto-optic sensors 28

1.2.5. Bulk-optic sensor 29

1.2.6. All-fiber sensor 31

1.3. Summary 35

Chapter 2 36

2.1. Phenomenological description of the magneto-optic effect 36

2.2. Light propagation in magneto-optical materials 38

2.3. Bulk Magneto Optical materials 41

2.3.1. (LaSr)MnO_3 43

2.3.2. Cobalt ferrites $CoFe_2O_4$ 44

2.3.3. Barium ferrite 44

2.3.4. Semiconductor $CdCr_2S_4$ 45

2.3.5. Ferric borate and ferric fluoride 45

2.3.6. Chromium trihalides: CrCl3, CrBr3, Cr I3 46

2.3.7. Europium chalcogenides films 46

2.3.8. Terbium gallium garnet (TGG) 47

2.4 Evolution of MO materials 48

2.4.1. Europium chalcogenides nanoclusters 49

2.4.2. Cobalt ferrites nanoparticles 49

2.4.3. Magneto plasmonic crystals 50

2.4.4. Organic materials 51
2.5. Yttrium iron garnet (YIG) 52
2.5.1 Bi: YIG film preparation processes 56
Chapter 3 58
3.1. Film preparation and Magneto–Optical characterization 58
3.1.1. Bi: YIG film preparation by metal-organic decomposition method 58
3.1.2. Experimental setup 60
3.1.3. Calculation of the MO response of the material 61
3.1.4. Result and discussion of MO measurements 63
3.1.5. FR dependence on annealing temperature and duration 65
3.1.6. Multilayer films 68
3.2. Crystallization process of the Bi: YIG 69
3.2.1. The XRD analyses of Bi: YIG films 69
3.2.2. SEM and AFM measurements of Bi: YIG films 71
3.2.3. XRD and SEM measurements of Bi: YIG powders 73
3.2.4. DTA measurements for Bi: YIG powders 75
3.2.5. Activation energy of Bi: YIG film crystallization 77
Chapter 4 81
4.1. Functionalization of an optical fiber with a garnet 81
4.1.1. The synthesis of Bi: YIG film at fiber end. 82
4.1.2. The synthesis of Bi: YIG pattern on the fiber core. 83
4.2 Magneto-optic sensor based on the Faraday effect 86
4.2.1. Magnetic field sensor device 86
4.2.2. Description the experimental setup through the Jones matrix formalism 88
4.2.3. Result of Faraday rotation and Faraday ellipticity measurements 91
4.2.4. Calculation of the dephasing $\boldsymbol{\varphi}$ 92
4.3 Magneto-optic sensor based on MCD 95
4.3.1. Magnetic field sensor device with one detector 95
4.3.2. Result of Faraday ellipticity only measurements 97
4.3.3. Effect of fiber orientation on the dephasing in the fiber 100
4.3.4.Conclusion 101
General Conclusion 102
RÉSUMÉ DE LA THÈSE DE DOCTORAT 105
Bibliography 117
Facsimile of the paper: *"Limits of the magneto-optical properties of Bi: YIG films prepared on silica by metal-organic decomposition"* 129

List of Figures

Chapter 1

Figure 1.1: Scheme of Earth inductor invented by C. E. J. Delzennes in 1844. ..... *20*
Figure 1.2: Demonstration of the fluxgate sensor operation. *21*
Figure 1.3: Schematic to illustrate the operating principle of magnetic sensors based on the Hall effect. *22*
Figure 1.4: Prototype design of optically pumped sensors. *23*
Figure 1.5: The giant magnetoresistance curves at 4.2 K of (Fe/Cr) multilayer. *24*
Figure 1.6: Fiber-optic sensor using magnetostrictive material. *26*
Figure 1.7: Schematic diagram of the Terfenol-D based fiber sensor proposed by Mora et al. [24]. . . *27*
Figure 1.8: Illustration the principle of work of the magnetic field sensor HC PCF FP proposed by Zhao et al. [30] *28*
Figure 1.9: MO sensor head with rectangle shape glass. *29*
Figure 1.10: Miniature Faraday current sensor based on multiple critical angle reflections in a bulk-optic ring taken from [32]. *29*
Figure 1.11: The principle of MO sensing based on FR measurement. *30*
Figure 1.12: Images of the sensor head using YIG material synthesized on GGG substrate taken from [35]. *30*
Figure 1.13: Schematics of an all-fiber optical gyroscope taken from [37]. *31*
Figure 1.14: Faraday/Sagnac loop interferometer current sensor taken from [38]. *31*
Figure 1.15: In line Sagnac interferometer current sensor taken from [38]. *32*
Figure 1.16: Faraday rotation mirror. *33*
Figure 1.17: Schematic diagram of the in-line Sagnac interferometer magnetic sensor based on MO polymer. In-line Sagnac interferometer sensor design taken from [49]. *34*

Chapter 2

Figure 2.1: Polarization changes by FR (left picture) and MCD (right picture) in a MO material. *37*
Figure 2.2: Scheme of reciprocal and non-reciprocal propagation through the active media. *38*
Figure 2.3: The spectral dependence of the FR for $La_{0.82}Sr_{0.18}MnO_3$ *[52], measured and calculated for* $CoFe_2O_4$ *[53],* $BaFe_{12}O_{19}$ *and* $BaFe_{10.42}Co_{0.78}Ti_{0.8}O_{12}$ *[54],* $FeBO_3$ *[55], and for* FeF_3 *[56],* $CdCr_2S_4$ *at 4.2 K [57]; .*$CrC1_3$*,* $CrBr_3$ *and* CrI_3 *at 1.5 K in saturating magnetic filed [58], EuS films at 10 K and H = 4 T [59],* Tm^{3+}*: TGG and pure TGG [60].* *42*
Figure 2.4: Lanthanum manganese oxides can be prepared via different methods: ceramic process [61], sol-gel [62], [63], radio frequency (RF) sputtering [52], pulsed laser deposition (PLD) [64]. . . *43*
Figure 2.5: Crystal structure of Spinel Ferrite with general formula AB_2O_4*, where A = divalent metallic cations (eg.* Mn^{2+}*,* Ni^{2+}*), B = trivalent cations (eg.* Fe^{3+}*,* Al^{3+}*).* *44*
Figure 2.6: The unit cell for $Ba_{1-x}La_xFe_{12}O_{19}$ *(where purple, red, and gold spheres correspond to Ba/La, O and Fe atoms respectively) taken from [66].* *44*
Figure 2.7: The unit cell for $CdCr_2S_4$*, where Cr atoms (blue balls) occupy the octahedral sites, and Cd atoms (pink balls) occupy the tetrahedral sites, S atoms (yellow balls) taken from [73].* *45*
Figure 2.8: Crystal structure of $FeBO_3$*, where red balls represent Fe atoms, white balls represent B atoms, and blue balls represent O atoms taken from [76].* M_1 *and* M_2 *are the magnetic moments of the* Fe^{3+} *ions.* *45*

Figure 2.9: Atomic structure of monolayer CrX_3 (X = Cl,Br,I), where blue balls represent Cr atoms, and pink balls represent Cl, Br, I atoms taken from [81]. (a) Top view and (b) side view of a single layer. 46
Figure 2.10: Crystal structure of EuO, where white balls represent Eu atoms, red balls represent O atoms. 46
Figure 2.11: The spectral dependence of the FR for $CoFe_2O_4$ NP's 1% fluids and $CoFe_2O_4$ NP's 2:2 monolayer [91], poly(3-octyloxy thiophene POT [92], Au-BIG with period 450 nm and 490 nm [93], Au-EuS with period 460 nm and 505 nm [94], EuSe NP's [95]. 48
Figure 2.12:(a) Schematic drawing of the structure of Au-EuS. (b) Colorized scanning electron micrograph of the sample cross section taken from [94]. 50
Figure 2.13: Structure of P3HT 51
Figure 2.14: Crystal structure of YIG. 52
Figure 2.15: The optical absorption spectrum of YIG taken from [121]. 53
Figure 2.16: (a) The FR and FE spetrum for different concentrations of bismuth in Bi: YIG films in the 450 – 550 nm range taken from [127] 54
Figure 2.17: (a) The concentration dependences of the FR for films: $Y_3Fe_{5-x}Ga_xO_{12}$, $Y_{3-x}Bi_xFe_5O_{12}$, $Y_{3-x}Pr_xFe_5O_{12}$, $Gd_{3-x}Bi_xFe_5O_{12}$, $Y_{3-2x}Pb^{2+}{}_xM^{4+}{}_xFe_5O_{12}$ (b) The concentration dependences of figure of merit $2\theta_F/\alpha$ $Y_{3-x}Bi_xFe_5O_{12}$ (solid and dash line) and $Gd_{3-x}Bi_xFe_5O_{12}$ (dot line) at 546 and 633 nm taken from [128], [129], [130] 55

Chapter 3

Figure 3.1: Schematic diagram of thin films preparation by MOD process. 60
Figure 3.2: Experimental setup for the FR measurements. 61
Figure 3.3: (a) FR (Inset: MO hysteresis measurement at 532 nm for x_{ini} = 1.3), (b) FE spectrum at saturation for Bi: YIG films on silica substrate with different initial amounts of bismuth, annealed at 700 °C for 1 hour. (c) The optical absorption for the same films. Inset: optical absorption at 532 nm (The line is a guide for the eyes). 63
Figure 3.4: Hysteresis loops measured from the FR at 532 nm for $Bi_xY_{3-x}Fe_5O_{12}$ as a function of the amount of bismuth, x_{ini}, in the initial solution. 64
Figure 3.5: FR dependency on temperature for 0.8 < x_{ini} < 2.2 samples (thicknesses 40 nm), annealed during 1 hour at different temperatures. 65
Figure 3.6: Evolution of the FR angle with the annealing time for different initial amounts of bismuth at (a) 660 °C and (b) 740 °C. Black square: x_{ini} = 0.8, Blue disk: x_{ini} = 1.0, Red up triangle: x_{ini} = 1.3, Green down triangle: x_{ini} = 1.6, Black diamond: x_{ini} = 1.9. 67
Figure 3.7: (a) FR, (b) normalization of FR, for x_{ini} = 1.0 and x_{ini} = 1.3 with different film thicknesses 50 and 250 nm. 68
Figure 3.8: XRD patterns of the Bi: YIG films annealed at 660 °C during 400 min for different initial amounts of bismuth: x_{ini} = 1.0, 1.3, 1.6, 1.9, 2.2. At the bottom, the histograms give the tabulated positions and relative intensities of the diffraction peaks for Bi: YIG, $YFeO_3$ and Fe_2O_3. 70
Figure 3.9: Evolution of the lattice parameter of the $Bi_xY_{3-x}Fe_5O_{12}$ with the amount of the initial part of Bi, compared with lattice parameters measured by Matsumoto et al. (109), Geller et al. (128), Strocka et al. (129) and Popova et al. (113). 71
Figure 3.10: SEM images of the Bi: YIG film with x_{ini} = 1.3 multilayer samples annealed at T = 660 °C. 71
Figure 3.11: SEM images for Bi: YIG multilayer film in profile with x_{ini} = 1.3 multilayer samples annealed at T = 660 °C. 72
Figure 3.12: AFM measurements for x_{ini} = 1 and x_{ini} = 2.2 of $Bi_xY_{3-x}Fe_5O_{12}$. 72

Figure 3.13: XRD patterns of the Bi: YIG powders annealed at 660 °C during 400 min for different initial amounts of bismuth: x_{ini} = 0.8, 1.0, 1.3, 1.6. At the bottom, the histograms give the tabulated positions and relative intensities of the diffraction peaks for Bi: YIG (x_{ini} = 1.5), $YFeO_3$, Y_2O_3, and Fe_2O_3. At the top, the tabulated positions and relative intensities of the diffraction peaks for $BiFeO_2$ and $Bi_2Fe_4O_9$. 74
Figure 3.14: SEM images at different scales for Bi: YIG powder prepared from a x_{ini} = 1.0 solution. 75
Figure 3.15: DTA for Bi: YIG powders prepared from solutions with x_{ini} = 0.8 – 2.2. 76
Figure 3.16: (a) Time dependent FR angle induced by the material for an initial compostions x_{ini} = 0.8, x_{ini} = 1.0, x_{ini} = 1.3, x_{ini} = 1.6, x_{ini} = 1.9 of $Bi_xY_{3-x}Fe_5O_{12}$ at different annealing temperatures. Lines are the adjustments by the solution in equation (3.18). 78
Figure 3.17: Variation with the temperature of the creation rates of MO phase for the different x_{ini}, the initial amounts of Bi. Lines are adjustments using an Arrhenius law. Inset: Activation energies of the creation of the MO phase for different initial amount of bismuth (The dashed line is a guide for the eyes). 79
Figure 3.18: Variation with the temperature of the destruction rates of the MO phase for different initial amounts of Bi x_{ini}. Lines are adjustments by Arrhenius law. 80

Chapter 4

Figure 4.1: Scheme of the production the Bi: YIG film at the end the optical fiber. 82
Figure 4.2: (a) SEM images of the synthesized Bi: YIG microcrystal on the cladding surface of the optical fiber with the initial composition x_{ini} = 1.3. The deposition procedure was repeated 2 times before the annealing at 660 °C for 5 hours. 83
Figure 4.3: Scheme of the production of Bi: YIG on the core of the optical fiber accompanied by microscopic-interferometry measurements of the surface topography. 84
Figure 4.4: (a) SEM image (b) Interferometric microscopy image of the Bi: YIG microcrystal on the core of optical fiber with the initial composition x_{ini} = 1.3. The deposition procedure was repeated 5 times before the annealing at 660°C for 5 – 7 hours. 85
Figure 4.5: SEM images (a) of Bi: YIG film at the edge of optical fiber coated with gold, (b) Bi: YIG microcrystal on the core of optical fiber coated with cold. 85
Figure 4.6: The scheme of the magnetic field sensor device. 86
Figure 4.7: The scheme of the magnetic field sensor device with indications of the Jones matrices for each optical element in the setup. Here φ_M is the amplitude of the dephasing generated by the PEM, ω is the frequency of the modulation of the light, θ_F is the angle of the FR, ηF is the angle of the FE and φ is the dephasing coming from the optical fiber and other optical elements and related to their birefringence. 88
Figure 4.8: The plot of Bessel function $J_n(\varphi_M)$, where n = 1, 2, 3, 4, 5. 90
Figure 4.9: (a) Fourier spectrum of the FR response, (b) FR and FE dependency on the amplitude of the magnetic field. 91
Figure 4.10: (a) MO response (red curve) as function of time while varying the magnetic field in the range -200 to 200 mT (black curve), (b) Hysteresis loop of Bi: YIG synthesized at the end of optical fiber. 92
Figure 4.11: (a) The difference between the intensities of the vertical and horizontal polarizations measured at ω and 2ω (b) The calculated value of φ as a function of φ_M 93
Figure 4.12: (a) Corrected values of differences between the intensities of the vertical and horizontal polarizations measured at ω and 2ω with the Bessel function fit (b) The plot of Bessel functions$J_n(\varphi_M)$, where n = 0, 1, 2. 93

Figure 4.13: $\Delta I(0)$, the difference between the intensities of the vertical and horizontal components measured at $\omega = 0$ as a function of the phase φ_M of PEM with the Bessel function fit. 94
Figure 4.14: The scheme of the magnetic field sensor device based on the FE measurements indicating the Jones matrices for each optical element in the setup. 95
Figure 4.15: (a) Fourier spectrum of the FE response, (b) FE dependency on the amplitude of the magnetic field. 97
Figure 4.16: Measured FE as a function of the amplitudes of the magnetic field. 97
Figure 4.17: FE as a function of time with different variation functions for the generated magnetic field. 98
Figure 4.18: FE as a function of the frequency of the generated square magnetic field. 99
Figure 4.19: Polarization maintaining (PM) "Panda" type fiber, with slow and fast axes indicated. 100
Figure 4.20: (a) Dependence of the intensities of the first and second harmonic components on the orientation angle of the fiber. The line correspond to the curve adjustment to the calculated response of the setup. (b) dephasing φ as a function of the orientation angle of the fiber ξ. 101

List of Tables

Table 1: Comparison of the sensing parameters of the magnetic field sensor technology. 35
Table 2: Value of the FR, the Kerr rotations for MO materials presented in this section and the way of their preparation. 43
Table 3: Composition of the initial solutions. 59
Table 4:Lattice parameter for Bi: YIG with x_{ini} from 1.0 to 2.2. 70

List of Abbreviations

AFM *Atomic Force Microscope*

AMR *Anisotropic Magnetoresistance*

BS *Beam Splitter*

Bi: YIG *Bismuth substituted Yttrium Iron Garnet*

CSD *Chemical Solution Deposition*

DTA *Differential Thermal Analysis*

FBG *Fiber Bragg-Gratings*

FE *Faraday Ellipticity*

FFT *Fast Fourier Transform*

FOM *Figure-Of-Merit*

FP *Fabry-Perot*

FR *Faraday Rotation*

GGG *Gadolinium Gallium Garnet*

GMR *Giant Magnetoresistance*

HC-PCF-FP *Hollow-Core Photonic Crystal Fiber Fabry-Perot*

HWP *Half-Wave Plate*

InSb *Indium Antimonide*

LCP *Left Circular Polarized*

LPE *Liquid Phase Epitaxy*

MCD *Magnetic Circular Dichroism*

MEMS *Microelectromechanical systems*

MO *Magneto-Optical*

MOD *Metal-Organic Decomposition*

Nd: YAG *Neodymium-Doped Yttrium Aluminium Garnet*

PEM *Photo Elastic Modulator*

PLD *Pulsed Laser Deposition*

PMF *Polarization Maintaining Fiber*

QWP *Quarter-Wave Plate*

RCP *Right Circular Polarized*

RF *Radio Frequency*

RMCD *Reflectance Magnetic Circular Dichroism*

SEM *Scanning Electron Microscope*

SMF *Single Mode Fiber*

SQUID *Superconducting Quantum Interference Device*

XRD *X-ray diffraction*

YIG *Yttrium Iron Garnet*

List of Symbols

B, H magnetic field

D electric displacement

E electric field

Ea activation energy

I light intensity

L length of MO material

M magnetization

N_+ *refraction index for right circular polarized waves*

N_- *refractive index for left circular polarized waves*

T temperature

V Verdet constant

k wave vector

k_C *rates of chemical reaction of Bi: YIG crystallization*

k_D *rates of chemical reaction of Bi: YIG degradation*

ε *dielectric permittivity*

ε_0 *vacuum permittivity*

η_F *Faraday ellipticity angle*

θ_F *Faraday rotation angle*

λ *wavelength*

μ_0 *vacuum permeability*

σ *optical conductivity*

φ *phase shift*

χ *dielectric susceptibility*

ω *angular frequency*

General Introduction

This dissertation is the framework of the ANR contract FOGAMO, which has started in January 2017 and going to end in January 2020. The main aim of this project is the functionalization of an optical fiber with a bismuth-substituted yttrium/iron garnet (Bi: YIG) for magneto-optical sensing applications, based on the Faraday effects The development of magnetic sensor has been done at *Institut de Physique et Chimie des Matériaux de Strasbourg* (IPCMS), UMR 7504 CNRS – Université de Strasbourg, in the *Département d'Optique ultrarapide et de Nanophotonique* (DON).

Most of the magneto-optical fibered sensors described in the literature find their application for high-voltage and current sensing using the Faraday effect of a fiber coiled around a conductor. A local measurement of magnetic field, at the millimeter scale or below, requires much higher Faraday rotation values than those accessible in silica fiber. To access a high spatial resolution of the magnetic field measurement, a solution is to functionalize the end of the optical fiber with the magneto-optical material to constitute the sensing part. The optical fiber is used to guide the light back and forth between the illumination/analysis systems and the remote magneto-optical material. One of the best-known materials for such an application is the Bi: YIG that exhibits a Faraday rotation at saturation of about 1000 $deg \cdot cm^{-1}$. Such functionalization of an optical fiber has been already demonstrated by H. Sohlström and K. Svantesson [1] using an epitaxially grown Bi YIG crystal on GGG substrates. Here, the crystal is cut and polished and then carefully aligned and attached at the end of the optical fiber. A holder ensures the mechanical strength of the sensing head. The size of such a sensor can be as small as a few millimeters. We propose here to considerably decrease the size of the magneto-optical sensitive part and to greatly simplify the assembly procedure by synthesizing a Bi: YIG microcrystal grown directly at the core area on the edge of an optical fiber.

We have developed an original method for the preparation of Bi: YIG starting from liquid organometallic precursors. These liquids can be prepared at a room temperature, in normal atmosphere and they present very low toxicity. The optimization of an initial formulation and of the synthesis process allowed the production of Bi: YIG thin films on silica showing around 1600 $deg \cdot cm^{-1}$ rotation at magnetic saturation [2, 3]. As the initial solution is light sensitive, the growth of the garnet phase from the solution can be limited to the exiting light mode area at the end of the fiber. It is possible to obtain a crystal with a size of a few micrometers, self-centered on the fiber core without any delicate shaping and alignment.

This dissertation contents 4 chapters. The first chapter is dedicated to different kinds of magnetic field sensors. They can be separated mainly on the effect they are based on. For instance: compasses based on mechanical effect, Hall effect sensors based on Lorentz forces, fluxgate sensors based on induction effect, SQUID sensors based on quantum effect, and optical sensors based on Faraday effect and on Zeeman effect. They are discussed in terms of the operation principle by pointing the ranges of operation, and their direct applications.

In the second chapter, we present different magneto-optical materials. We briefly discuss their optical and magneto-optical properties, point out their main advantages and disadvantages and compare to the material we selected: Bi: YIG. In addition, different methods of preparation of the Bi: YIG films are presented.

The third chapter is dedicated to the characterization of the magneto-optical and structural properties of the Bi: YIG films prepared by metal-organic decomposition method. We show that the magneto-

optical properties Bi: YIG films depend on the annealing temperature, on the duration of the annealing and on the composition of the initial solution. The systematic study of the magneto-optical properties of Bi: YIGs prepared using different sets of parameters allowed us to find the optimal conditions to achieve the largest Faraday rotation. In addition, these studies gave us the possibility to determine the temperature dependent rates of crystallization of Bi: YIG films allowing the calculation of the activation energy.

Finally, the fourth chapter is dedicated to the development and to the optimization of the synthesis process of Bi: YIG at the end of optical fiber without any specific mechanical holder or alignment device, which will make its production simple and low cost. We present an original method of preparation of the garnet microcrystals with 2 – 3 μm size self-centered on the core of the optical fiber. The prepared Bi: YIG at the fiber end is characterized for the measurement of magnetic fields ranging from 100 mT down to a few μT. Moreover, the setup allows us to make the magnetic field measurements based not only on Faraday rotation but Faraday ellipticity, which gives us the opportunity to significantly simplify the detection system and open new perspectives for the magnetic field measurements.

Chapter 1

1.1. Magnetic sensing technology

1.1.1. Introduction

1.1.2. Induction magnetometers

1.1.3. Hall Effect Sensors

1.1.4. Proton magnetometer

1.1.5. Optically pumped magnetometer

1.1.6. Magnetoresistive sensors

a) Anisotropic magnetoresistance AMR sensors

b) Giant magnetoresistance GMR sensors

1.1.7. Superconducting Quantum Interference Device (SQUID) sensors

1.1. Magnetic sensing technology

1.1.1. Compass

The first mention of the magnetic field sensing in the history appears in China, where back as far as the fourth century BC, the floating of steel needle on the water surface was used as much for feng shui as for navigation on land. In 1190 in Europe Alexander Neckam described a magnet device, which used for navigation and helped travelers in the determination of the orientation of the Earth’s magnetic field, later it will be known as a compass. It is still not clear for history if this knowledge come to Europe from China, or was invented separately. Anyway, this device allowed ships to confidently cross the seas and oceans without fear of getting lost and it pushed humans to many discovers.

The studying of the Earth magnetic field has started from 1269 when French scientist Petrus Peregrinus de Maricourt mapped out the magnetic field of the Earth, and he also named the resulted crossed field lines as "poles" in analogy to Earth's poles. Later, he articulated the principle that magnets always have both north and a south poles. Only after more than 300 years, William Gilbert was the first, who called Earth as "a big magnet", using the Petrus Peregrinus's work.

Back in the lab, the compass was effectively the first magnetometer used in the early electromagnetic studies. In 1820, Oersted observed that an electrical current tends to orient perpendicularly to the conducting wire. This was the first evidence of the relation between magnetism and electricity. But the first absolute magnetometer is attributed to K. F. Gauss. Measuring the oscillation period of a permanent magnet suspended by gold wire and the deviation angle of this magnet induced by another similar one, he was able to give the absolute value of the magnetic fields [4]. The devices using the deviation of a magnet in a magnetic field are known as magnetic scales or variometers. The most

famous are the Thalen-Tiber magnetometer [5] and Schmidt's scale. They have been widely used until the mid-XXth century for geophysical and mining applications [6, 7].

1.1.2. Induction magnetometers

The development of electromagnetism by A. M. Ampère and M. Faraday led to the development of inductive sensors where the external magnetic field induces voltage changes in the internal circuit of the device proportional to the rate of flux change in induction coil. The Earth inductor built by C. E. J. Delzenne in 1844, uses rotating coils to induce an electrical current from the Earth's magnetic field (see Figure 1.1). The orientation of the coil allows distinguishing between the horizontal and vertical component of the field [8].

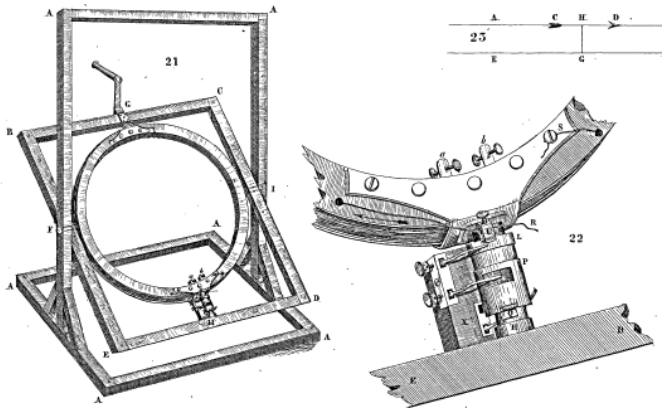

Figure 1.1: Scheme of Earth inductor invented by C. E. J. Delzennes in 1844.

It is to note that the Cambridge Earth inductor, developed in the 1930s, was still in use until 1986 at the French magnetic laboratory as a reference device.

This family of the inductive sensors using passive coils is still in use in automotive speed sensors for example. Their sensitivity depends directly on the number of turns in the coil, and therefore, their size. Most often, the coil wire winds up around a high magnetic permeability material (ferrite ceramic rod) to amplify the flux density. Passive devices which depend on the mobility of magnetic objects are rather insensitive at low speeds and have no output at zero speed at all. However, at present, they are irreplaceable in the industry for automotive anti-skid braking systems [9].

Sensors of this type can detect fields as weak as 20 fT [10], with no upper limit to their sensitivity range. Their useful frequency typically ranges from 1 Hz to 1 MHz. In addition to this passive use, one can also operate a search coil in an active mode to construct a proximity sensor for metal detection. In 1874, Gustave Trouvé invented the first device prototype for locating and extracting the bullets or metals objects from human bodies. Later in 1881, A. G. Bell developed a similar device and used it for the same application [11]. For metal detection, the device requires another coil, which carrying a high frequency alternating electric current. It constantly changes the magnetic field to induces eddy currents in conducting object. The closer the target, the greater the induced eddy currents and the more effective their induced magnetic fields, which are therefore easier to detect by the search coil.

Fluxgate sensors can also be classified as an induction sensor. They are widely used for low-level magnetic fields in geomagnetic surveying, compassing, ferromagnetic metal detection, and even submarine hunting. Invented by V. Vacquier in 1939, the fluxgate sensors are based on effect ferromagnetic saturation at high magnetic fields and consist of a ferromagnetic material wound with

two coils, a driving one, and a sensing one. The operating principle of the fluxgate sensor is illustrated in Figure 1.2 (a).

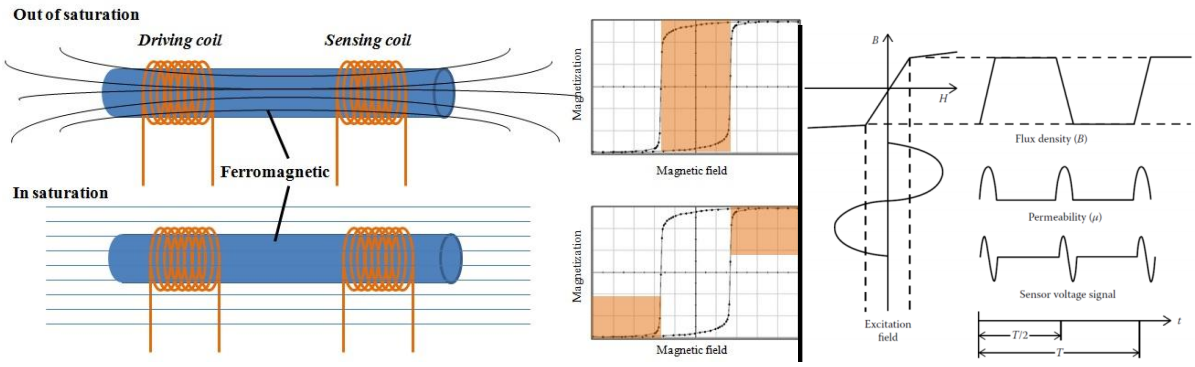

a. b.

Figure 1.2: Demonstration of the fluxgate sensor operation.

When a sinusoidal current of sufficient amplitude to push the ferromagnetic core into saturation is applied to the driving coil, the sensing coil responds to the fast change in magnetic flux happening during the polar inversion jumps. The induced voltage is proportional to the number of turns (n), the rate of change of the magnetic field in the core, and the cross-sectional area of the core (S):

$$V(t) = nS\frac{dB}{dt}. \tag{1.1}$$

In the core material with a square hysteresis loop, these changes will occur periodically and the induced voltage will be presented as an alternating series of short, symmetrical pulses, equally spaced in time (see Figure 1.2 (b)). In this case, these pulses will only have odd harmonics due to the odd symmetry of the pulses. With a signal filtering at twice the drive frequency, it becomes possible to extract the second harmonic signal and to obtain a signal proportional to the external field. The sensitivity of the fluxgate type sensors depends on the shape of the hysteresis curve used in the core ferromagnetic material. To maximize the sensitivity, it is better to use core materials with a square curve of magnetic induction. The sensitivity ranges from 10^{-2} to 10^{-7} T [12]. The frequency response of the sensor is limited by the excitation field and the response time of the ferromagnetic material. The upper limit on the frequency is about 10 kHz. The size of the fluxgate sensing head allows the measurement of the magnetic field at a small scale and so it is for the Hall sensors.

1.1.3. Hall Effect Sensors

In 1879, E. Hall discovered the effect of a magnetic field on motion of charge carriers. Here, the Lorentz force accelerates moving charge carriers in a direction perpendicular to both their direction of motion and to the magnetic field. For a current in a plate of semiconductor material, the Hall effect leads to the appearance of the Hall voltage across the plate proportional to the magnetic field on plate and perpendicular to the current and to the magnetic field. Figure 1.3 shows the geometry of a Hall sensor. These devices are very attractive due to the low cost of their components. In practice, gallium arsenide (GaAs), indium arsenide (InAs), indium phosphide (InP), indium antimonide (InSb) are especially suitable for Hall effect sensors. They have been gaining popularity due to their high electron-carrier mobilities which result in greater sensitivity and in frequency response capabilities above the 10 – 20 kHz typical of Si Hall sensors. (Si Hall sensors 1 – 100 mT, InSb extend the lower limit to 100 nT)

The Hall voltage based device provides much better measurement accuracy compared to fluxgate magnetometers or magnetoresistance-based sensors. The temperature dependence of the Hall voltage and the input resistance of Hall sensors are governed by the temperature dependence of the carrier mobility and of the Hall coefficient. The trade-offs between sensitivity and temperature dependence determine the choice of the materials and of the doping levels.

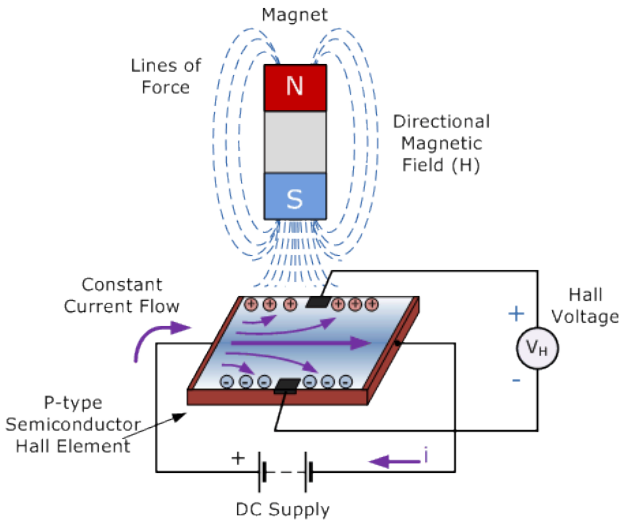

Figure 1.3: Schematic to illustrate the operating principle of magnetic sensors based on the Hall effect.

Because of the low signal level, the Hall effect sensors were effectively developed after World War II, taking advantage of the huge progress of the performances of electronic devices. At this time, the small size of electronic amplifiers and their low cost have allowed their production at a large scale.

1.1.4. Proton magnetometer

High performances electronic devices and the rapid progress of quantum physics boosted the development of magnetic sensor in the second part of the XXth century. The discovery of the nuclear magnetic resonance by I. Rabi in 1938 [13], developed in 1946 by F. Bloch and E. Purcell found their application to magnetic field measurements in 1948 with the work of R. H. Varian [14]. Here, a hydrogen-rich material is polarized by a strong magnetic field. Once the polarization field is interrupted, the magnetic moment precesses under the influence of the ambient magnetic field at a frequency proportional to its strength. An electronic circuit amplifies and measures the frequency of the signal of the weak rotating magnetic field induced in an inductor to give the value of the magnetic field.

1.1.5. Optically pumped magnetometer

Another non-trivial type of sensor devices uses the Zeeman effect inducing a division of the spectral lines depending on the applied magnetic field strength. This effect has been discovered by P. Zeeman in 1896, but its application to magnetic measurements started in the late 1950s with the invention of optical pumping [15]. Here, the population of the hyperfine levels is probed by a polarized light beam. Adjusting the frequency of a microwave beam to the hyperfine transition depending on the magnetic field leads to a variation the population. The tuning of the frequency is revealed by the light beam transmission and gives the corresponding magnetic field value. Optically pumped magnetometers is still an active research field today, experimenting with new detection methods and leading to miniature sensors with 1 cm square footprint.

The spectral lines of certain atoms, specifically alkali elements such as cesium, helium or rubidium are used in optically pumped magnetometers. The atom of cesium may be described as a three-level system. The energy difference between the two-level states corresponds to a microwave frequency. They differ by their orientation of the spin axis, parallel and antiparallel. The higher state has the same angular momentum as one of the lower states and the transition between one of the lower and the higher energy state is in the optical frequencies range.

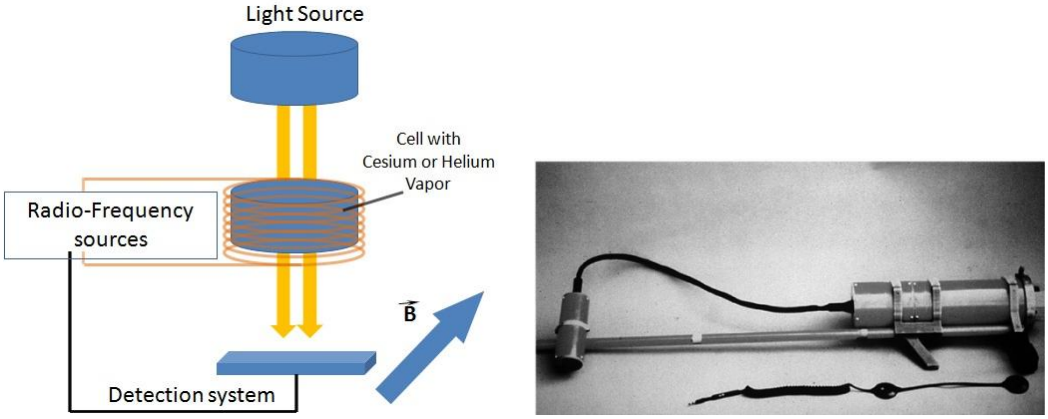

Figure 1.4: Prototype design of optically pumped sensors.

The cell with cesium vapor is pumped by circularly polarized light (see Figure 1.4). Because of the optical selection rules, only transitions from one of the lower states to the excited state may happen. The resulting absorption can be measured by the detection system. The electrons in the higher state drop back down to the lower states and in some cases, they may fall into the state that cannot absorb. After some time, almost all electrons will have accumulated in the dark state and the system will become completely transparent to the light. When radio-frequency is now applied to the vapor system at the correct frequency, it changes the spin angular momentum of the electrons i.e. induces a transition between the lower two states, which in turn, re-enable the light absorption mechanism. The combination of the radio frequency and optical pumping produce a specifically sharp resonance and this resonance effect can be used to measure the magnetic field, which splits the lower two states.

The sensitivity of this type of sensors is determined by the accuracy of the signal analysis system and is used in the range from 1 nT or 1 T. There are many disadvantages to using them: the production is expensive and difficult and the size of the device is limited by the vapor cell. Its size cannot be too small as collisions with cell wall limits the spin lifetime.

1.1.6. Magnetoresistive sensors

The sensors based on magnetoresistance use the change in electrical resistance caused by the external-applied magnetic field. There are many sensor technologies based on the magnetoresistance effect which may occur in a large variety of materials: bulk non-magnetic materials and semiconductors (geometrical magnetoresistance), magnetic metals and ferromagnets (anisotropic magnetoresistance), and finally multilayer systems using magnetic tunnel junctions (tunnel magnetoresistance, giant magnetoresistance, extraordinary magnetoresistance).

a) Anisotropic magnetoresistance AMR sensors

The first observation of the magnetoresistance effect was made in 1856 by William Thomson, and the observed change in electrical resistance was not more than 5 %. Nowadays, the most common magnetoresistive material is produced from nickel-iron alloys (permalloys). This material looks very

attractive in industrial applications because of the large change in electrical resistance (> 1 order of magnitude) and for its low cost. The change in resistivity is anisotropic and its experimental shape can be expressed as:

$$R(\alpha) = R_0 + \Delta R cos^2(\alpha), \tag{1.2}$$

where α is the angle between the magnetization vector(direction of the detected field) and the current, and R_0 is the resistivity for $\alpha = \pi/2$. Its anisotropic properties can be set during the fabrication process. It allows to get thin permalloy strips with highly uniaxial anisotropic characteristics (when using magnetizing field during film deposition). Such sensors are called anisotropic magnetoresistance (AMR) sensors. The AMR sensors are used in combination with an electrical circuit (Wheatstone bridge) in order to enhance the output signal and reduce the effect of external perturbations like temperature drift for instance. The AMR sensors have a sensitivity range of 1 µT to 1 mT and can operate at temperatures between -55 °C and 200 °C.

b) Giant magnetoresistance sensors

Giant magnetoresistance (GMR) sensors are based on the quantum mechanical magnetoresistance effect observed in planar multilayers structures composed of alternating ferromagnetic and non-magnetic conductive layers. In 2007 Albert Fert and Peter Grünberg were awarded the Nobel Prize in Physics for the discovery of GMR. This effect was observes for the first time in 1988 independently in the groups of Albert Fert (University of Paris-Sud) and of Peter Grünberg (Forschungszentrum Jülich, Germany).

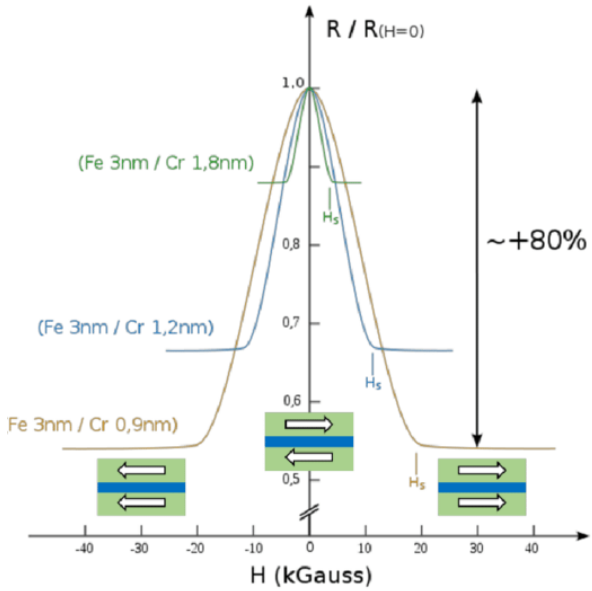

Figure 1.5: The giant magnetoresistance curves at 4.2 K of (Fe/Cr) multilayer.

In its simplest form, the GMR can be presented as a four-layer structure that consists of two thin layers of ferromagnets separated by a conductor. The fourth layer is an antiferromagnet that is used to pin (inhibit the rotation) the magnetization of one of the ferromagnetic layers. In the ferromagnetic layers, the orientation of the magnetization strongly influences the resistance of the system. Electrons can flow more readily when the orientation of the magnetization of two ferromagnetic layers are parallel to each other, which corresponds to low resistance and more difficulty when the orientation is antiparallel which corresponds to high resistance. The difference in resistivity between these two cases can be as

large as 12.8 % at room temperature and 80 % at 4.2 K (see Figure 1.5) [16]. This allows one to a measure magnetic field as small as 10 nT at 1 Hz. Today, to optimize the effect the layers produced are only a nanometer thick. The main application of GMR is magnetic field sensors, which are used to read data in hard-disk drives, biosensors, microelectromechanical systems (MEMS).

1.1.7. Superconducting Quantum Interference Device (SQUID) sensors

The SQUID is extremely high sensitive magnetometer, which have been developed specifically to detect exceedingly weak magnetic fields as low as 5 aT ($5 \cdot 10^{-18}$ T, with several averaged measurements) [17]. The technique is based on superconducting loops containing Josephson junctions. The production of this type of device is very expensive as it traditionally consists of pure niobium or a lead alloy with 10 % gold or indium, and only be used in combination with cryogenic refrigeration as the device needs to operate at a few degrees above absolute zero. They find their applications in material science but also in medical and biological applications, such as to measure the activity inside of the human brain (magnetoencephalography).

1.2. Magneto optical (MO) sensors

1.2.1. Magnetostrictive sensors

1.2.2. Terfenol-D

1.2.3. Magnetic Fluid

1.2.4. Magneto-optic sensors

1.2.5. Bulk-optic sensor

1.2.6. All-fiber sensor

1.2. Magneto optical (MO) sensors

One common feature of the systems described above is that they require some electric connections of the sensor to perform the measurement of the magnetic field. In a perturbed electromagnetic environment, the electric wires collect also some noise and require shielding. The use of light propagating in an optical fiber as information carrier, offers a good alternative as it is intrinsically protected from these electromagnetic noise sources. This property motivated the development of all-optical sensors mainly for the electric power industry.

One can distinguish between two main families of optical magnetic sensors. The first uses light to measure the perturbations of the sensing device due to a magnetic field, like optical transmission or strain. The second works on the magneto-optic effect that couples the light polarization and the magnetic field in a material.

1.2.1. Magnetostrictive sensors

The magnetostrictive interferometer is related to the first group of optical magnetic sensors. Here two optical fibers are arranged to form a Mach-Zender interferometer [18]. The light from a laser source is injected into both fibers. One of the fibers is wrapped around magnetostrictive material (nickel [19 - 21], Vitrovac 40 – 60, ceramic thin films (Fe_2O_4, $Ni_xCo_{1-x}Fe_2O_3$) [22, 23]). Through the influence of the external magnetic field, the length of magnetostrictive material extends and produces some stress in the fiber, which in turn produces additional birefringence. The light in the other fiber branch travels along the same length of fiber unaffected by the field. These two fibers are coupled optically just before each of them arrives at its detector. The interference signal of the beams depending on the phase shift between the two paths gives the value of the magnetic field (see Figure 1.6).

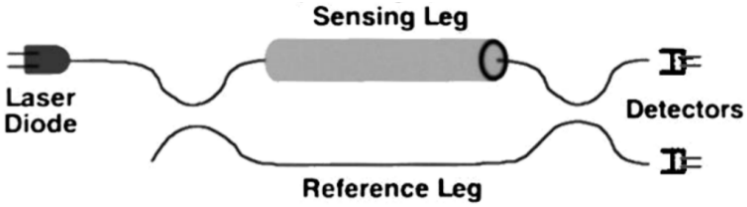

Figure 1.6: Fiber-optic sensor using magnetostrictive material.

This device is uniquely sensitive to the orientation of field lines and could be applicable for its curvature measurements, as well as the strength of the magnetic field. Also, it is widely used in current sensing, with the fiber wrapped around the conductor. In combination with different magnetostrictive materials, the sensor demonstrated sensitivity in the range 10^{-2} nT to 1 mT.

1.2.2. Terfenol-D

The first demonstration of Terfenol-D based sensors combined with optical sensors to measure static magnetic fields and temperature was made by Mora [24]. This type of magnetostrictive sensor is composed from two different alloys, the Terfenol-D and Monel 400, with an equivalent thermal expansion coefficient for the compensation of the temperature variation. The mechanical extension of these two materials is coming either from temperature or magnetic field variations. This extension is detected by the two fiber Bragg-gratings (FBG) attached. See Figure 1.7

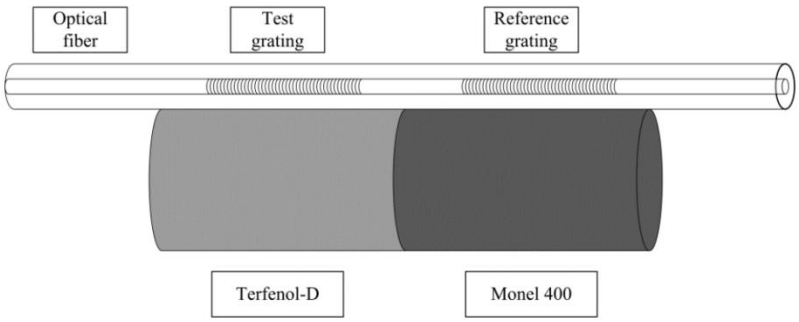

Figure 1.7: Schematic diagram of the Terfenol-D based fiber sensor proposed by Mora et al. [24].

The spectral difference between the two Bragg wavelengths is proportional to the expansion of the magnetostrictive elements which is proportional to the magnetic field. The wavelength shift produced by the FBG attached to the non-magnetic alloy (Monel 400) is proportional to the temperature variation [25]. The simultaneous measurements of the magnetic field as small as 70 mT and temperature variations in the range 18 °C to 90 °C were demonstrated by Reilly et al. [26] in 2006.

In 2009, Yang et al. [27] produced a small magnetic field sensor by coating the optical fiber with a Terfenol-D thin film. Not only did the size become as small as 85 μm but the sensitivity also improves. In production, the Terfenol-D thin film is deposited on prepared FBGs by the sputtering deposition process. The sensitivity can be enhanced by increasing the thickness of the deposited material.

1.2.3. Magnetic Fluid

The magnetic fluid is usually a type of oil, whose properties such as viscosity, refractive index, transparency depend on orientation and strength of a magnetic field. The study of optical transmission properties of the magnetic fluid under magnetic field has been carried out by Yang et al. [28]. In his experiments, it was demonstrated that magnetic particles agglomerate forming magnetic columns in the presence of the magnetic field. The fluid itself is transparent, whereas the appearance of columns opacifies the fluid. With the increase of the external magnetic field more columns are formed, which leads to a decreasing of the optical transmission.

The same group also investigated the refractive index dependence on the applied magnetic field, which led to the designing of a fiber optic current sensor by Hu et al. [29]. The magnetic fluid is inserted in a

resonant cavity, as the optical medium in a Fabry-Perot (FP). The refractive index of the medium is changing under the influence of the external magnetic field and modifies the output spectrum of the FP fiber sensor. In 2012, Zhao et al. [30] presented the magnetic field sensor based on a magnetic fluid contained in a Fabry-Perot hollow core photonic crystal fiber (HC-PCF-FP) as shown in Figure 1.8.

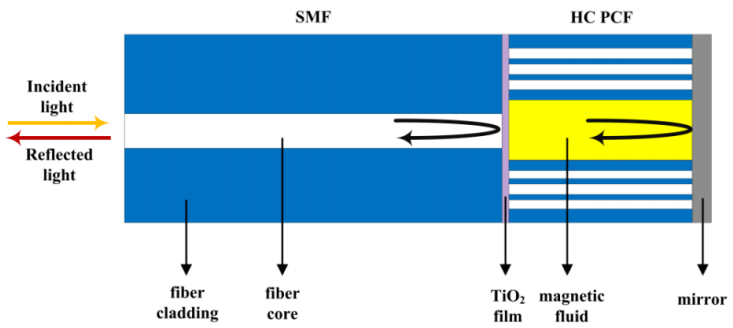

Figure 1.8: Illustration the principle of work of the magnetic field sensor HC PCF FP proposed by Zhao et al. [30].

The HC-PCF-FP implemented into a Sagnac interferometer and contained a polarization-maintaining fiber. The magnetic field measurement resolution could reach 37.7 μT.

1.2.4. Magneto-optic sensors

In 1845, M. Faraday discovered that the linear polarization of a light beam passing through a piece of glass was rotated by a magnetic field applied along the light propagation direction. This was the first demonstration of coupling between magnetism and light. The magnetic field can also introduce some discrepancy between the absorption of left or right circular polarized light. This magnetic circular dichroism (MCD) was evidenced later thanks to the discovery of Zeeman effect in 1896. These effects will be detailed in Sections 2.1 and 2.2.

The rotation of the polarization is proportional to the strength of the magnetic field B, to the interaction length L and to the properties of the material characterized by the Verdet's constant V. The rotation is then simply express by equation (1.3):

$$\theta_F = V \cdot B \cdot L. \tag{1.3}$$

θ_F is the Faraday rotation (FR) angle. A specific feature of the MO effect is its non-reciprocity due to the chirality induced by the magnetic field. As a consequence, a light beam reflected back after passing through a MO material will see its polarization rotation angle doubled at the exit of the crystal in comparison with a single pass (see Section 2.1 for more details). The same experiment with a birefringent plate leads to a compensation of the depolarization after such a double pass. The non-reciprocity is of great interest as it allows to amplify the response via a double pass but also allows to distinguish between the depolarization due to the birefringence and to the Faraday effect.

In a polarimetry arrangement, the measurement of the rotation of a linear polarized light beam leads directly to the amplitude of the magnetic field. Such devices are mainly described for the measurement of electrical current for electric power plant. Here, the light beam circulates around the conductor, confined in a magneto-optic material.

1.2.5. Bulk-optic sensor

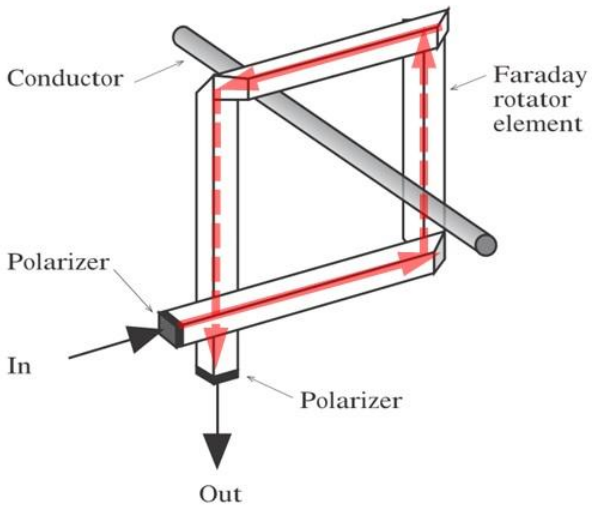

Figure 1.9: MO sensor head with rectangle shape glass.

The first bulk-optic sensors was shown by Sato et al. [31], made of standard glass with a rectangular shape (see Figure 1.9). Also, the glass can be easily substituted by another material with a higher Verdet constant, and due to their low photo-elastic coefficients, the linear birefringence affecting the polarization of light is negligible. Such a setup is shown to be robust regarding external perturbations such as temperature variations, vibration or electromagnetic noise. Nevertheless, the system can be affected by other external factors such as humidity! As the light reflects in the crystal several times, depends on its design, this may introduce an additional optical phase difference between the two circular polarization states, which is not related for magnetic effect. The solution of the problem will be concluded in isolation of the system, but it will lead the increase of the cost.

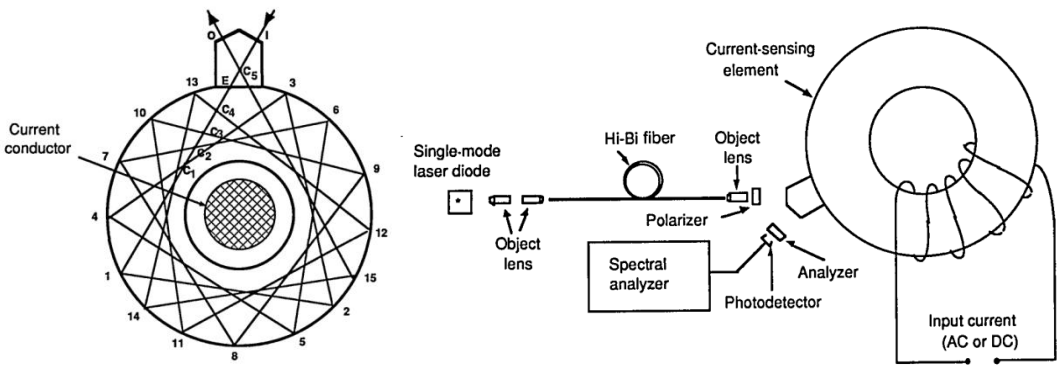

Figure 1.10: Miniature Faraday current sensor based on multiple critical angle reflections in a bulk-optic ring taken from [32].

The variety shape of the sensing element allows increasing the MO response of these devices. One of a good example is a circular sensor head with the prism light injection system under specific angles. The scheme provides the extension of the optical path inside the crystal where the light reflects from its sides several times before it exits from the sensing element [32, 33] (see Figure 1.10).

The main disadvantages of these sensors are related to difficulty in production special shape of the sensing elements, and the further implementation of attaching to optical fiber, and the fragility of the system coming from relevant the big size of the sensing element.

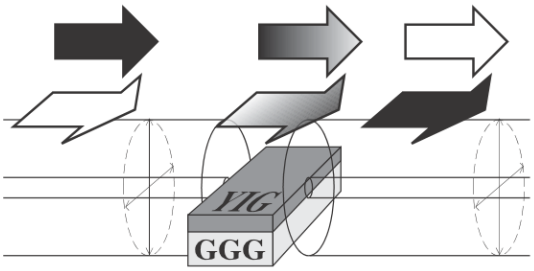

Figure 1.11: The principle of MO sensing based on FR measurement.

In the early 90s, an optical fiber sensor based on yttrium iron garnet (YIG) was presented by Hans Sohlström [1, 34, 35]. The device used a YIG crystal [1] epitaxially grown on Gadolinium Gallium Garnet (GGG) single crystal substrate. The thicknesses of the YIG crystals were around 5 – 10 μm, which allowed to use them effectively as single-mode waveguides. A single mode fiber is coupled on the edge of YIG/GGG sample (the core diameter of the optical fiber is around 2 μm). The basic sensing principle is shown in Figure 1.11. The FR angle of such sensor is 1000 deg·cm^{-1} ($1.7 \cdot 10^3$ rad·m^{-1}) at 1.15 μm wavelength.

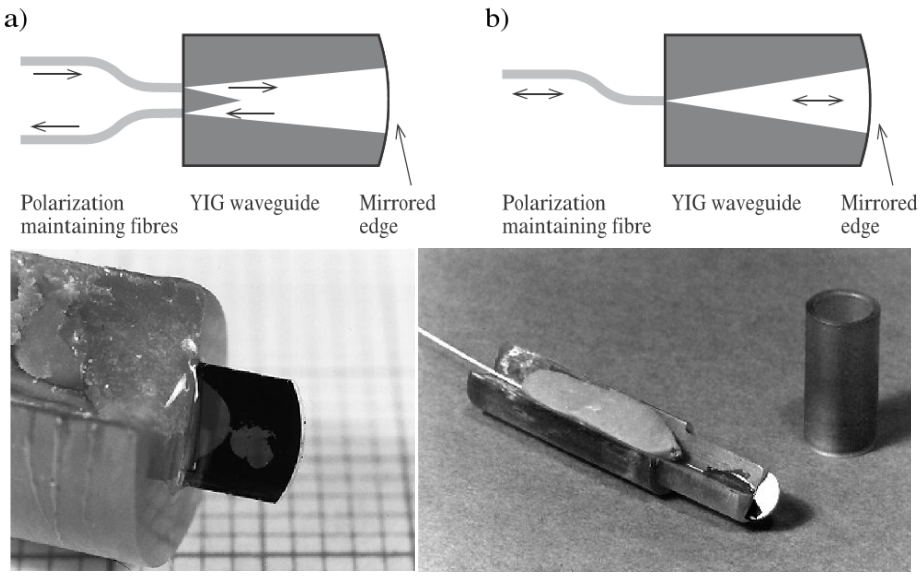

Figure 1.12: Images of the sensor head using YIG material synthesized on GGG substrate taken from [35].

As already mentioned, going back and forth in the crystal doubles the FR and then enhanced the sensitivity. Here, the same YIG/GGG sensing element was used. In one side the polished end of the polarization maintaining optical fiber is very carefully aligned when attached to the front of the sensing element, the back of which is polished into the arc of a circle and coated with a thin gold film to increase the back reflection (see Figure 1.12) [35]. Here the detection of the magnetic field is made by polarimetry. The prototype test showed a good signal quality with noise level about 8 nT infor a 1 Hz bandwidth. A size of such sensors as small as 5 – 10 mm.

1.2.6. All-fiber sensor

Compared to the devices described above, all-fiber sensors use the optical fiber not only to carry light, but as the magneto-optic medium itself [36]. At the beginning of these developments, the detection was based on polarimetric analysis of the FR. In the mid-1970's, the development of the optical fiber gyroscopes triggered the apparition of interferometric detection. Indeed, in an optical gyroscope based on a Sagnac interferometer [37], the rotation of a fiber coil around its axis induces a non reciprocical dephasing on the two counterpropagating waves in the fiber. The Faraday effect also induces such a non reciprocal phase shift and the measurement techniques are very similar. Figure 1.13 shows the fundamental scheme of a fiber gyroscope.

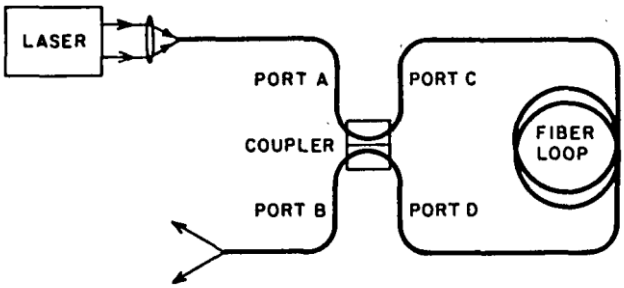

Figure 1.13: Schematics of an all-fiber optical gyroscope taken from [37].

The similarity of this arrangement with the Faraday/Sagnac fiber loop interferometer current sensor presented in Figure 1.14 is more than obvious.

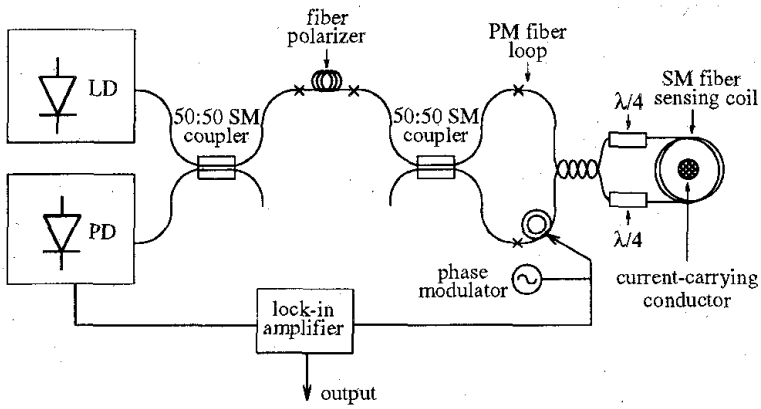

Figure 1.14: Faraday/Sagnac loop interferometer current sensor taken from [38].

Here, the light travels in an optical fiber coiled around the conductor just as in the bulk optic sensors presented in the previous paragraph. As the Faraday effect introduces non-reciprocal dephasing on circularly polarized light, the quarter wave-plates (QWP) transforms the linearly polarized light traveling in the polarization-maintaining fiber into circularly polarized light. Coming back from the loop, the light experiments the reverse transformation. Doing so, the dephasing between the two returning beams is due to the Faraday effect only. All the contributions from the birefringence of the fibers and optical elements are compensated and canceled. A phase modulator is generally used in order to obtain a better signal to noise ratio. The interference signal is measured via a photodetector connected with a lock-in amplifier.

This arrangement has progressively evolved and has been simplified over time. Figure 1.15 shows an inline Sagnac interferometer where only one beam is injected in the coil and reflected back by a mirror at the end of the fiber. The two orthogonal modes, corresponding to the major axis of a polarization-maintaining fiber, are transformed into two orthogonal circularly polarized beams by the QWP. They undergo dephasing related to the Faraday effect. The mirror reflects back the two modes reconverted to linear polarized beams as they pass through the QWP again. Doing so, the linear polarizations in the backward beam are swapped in comparison with the forward beam (forward horizontal polarization comes back vertically polarized and forward vertical returns as horizontally polarized). This allows the compensation of the birefringence. The two retro-propagating polarization modes are mixed via a polarizer and their interferences modulate the output intensity collected by a photodetector.

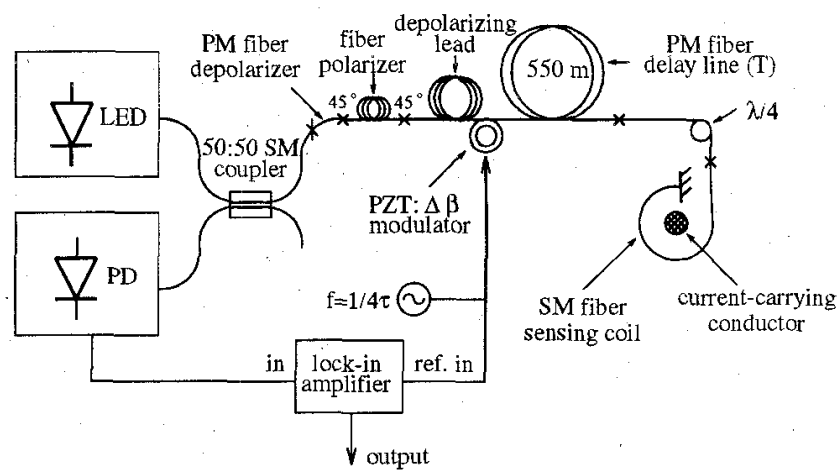

Figure 1.15: In line Sagnac interferometer current sensor taken from [38].

In all fiber sensors, the sensitivity depends on the Verdet constant of the optical fiber and on the number of turns in the coil.

The sensitivity of the all-fiber sensors is defined by the length and the Verdet constant of the optical fibers. The Verdet constant of standard silica fibers is low. A lot of investigations dedicated to the production have been done in order to increase the value of the Verdet constant.

Usually, the available materials which exhibit a FR angle large enough for magnetic field sensors are classified into three groups. The first group contents the optical glasses used for the fabrication of standard optical fiber with the low Verdet constant. In the second group are diamagnetic doped glasses, where the high concentrations of ions rises the refractive index and increases the Verdet constant. In the last group are rare-earth glasses or, in other words, the paramagnetic ion-doped glasses which have a large Verdet constants.

A flint glass [39, 40] showed a Verdet constant six times higher than a standard silica fiber and much lower photo-elastic coefficient (780 times). Later on, this material was used for current sensing application with a reduced temperature dependency and better accuracy [41] compared to a twisted single-mode fiber [42].

In 2009, a new glass material with high refractive indexes was presented by Poland research group of the Silesian University of Technology [43]. The Verdet constant value for the glass with refractive index 2.2 is 35.70 rad·(T·m)$^{-1}$ at 635 nm and 8.57 rad·(T·m)$^{-1}$ at 1550 nm.

Another way to increase the value of the Verdet constant is to dope the phosphate fiber core with terbium (Tb) [44, 45]. The idea comes from the development of magnetic terbium gallium garnet (TGG) crystals, usually used in bulk-optic materials. This material presents the highest value of the Verdet constant for such crystal with 40 rad·(T·m)$^{-1}$ at 1064 nm and -134 rad·(T·m)$^{-1}$ at 634 nm at liquid helium temperature [46]. The highest reached value of the Verdet constant for the terbium-doped fiber is -32 rad·(T·m)$^{-1}$ for operation at room temperature when for the standard fiber this value is around 1 rad·(T·m)$^{-1}$ at 1053 nm [45].

As already mentioned, the effect of linear birefringence, which is induced by mechanical stress, thermal fluctuation, manufacture imperfections, and other effects reduces the sensitivity of the sensor based on FR because of polarization degradation. The longer fiber is used the more linear birefringence is induced. However, there are a several methods to reduce or compensate this effect. The birefringence effect can be greatly reduced in single-mode fiber during production process-annealing procedure [47]. The process involves 3 – 4 days of the annealing temperature cycles around 850 °C.

Another way to fight with birefringence effect is to compensate it by using reflected light elements, such as Faraday rotating mirrors [48] or other polarization rotators, as described before, which in turn also double the sensitivity for the same fiber length. This element leads to the rotation of the polarization at 90°. In this case, which is propagates in one axis is re-couple to the other axis, and reverse. While the linear birefringence is a reciprocal effect, the phase difference introduced in an optical fiber by temperature fluctuation or external stresses, which in turn produce the linear birefringence, is compensated. In Figure 1.17 the example of usage of the Faraday rotation mirror in the scheme of the current sensing device.

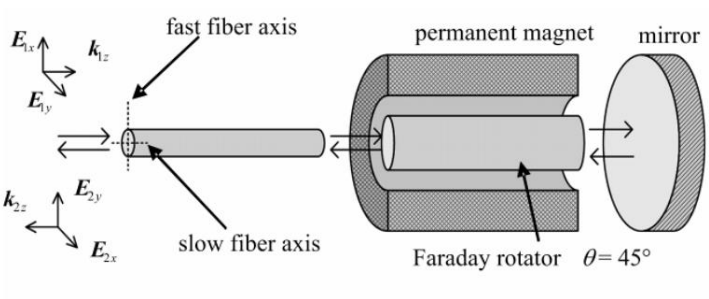

Figure 1.16: Faraday rotation mirror.

The MO fiber-based sensors for current measurements are commercially available. The patent belongs to the ABB Company, which uses the Faraday mirror shown in Figure 1.17. The range of the operation can go up to 500 kA with 0.1 % of accuracy.

All-fiber sensors relate to intrinsic type sensors which are very easy to implement by a simple coiling of the optical fiber around the conductor. Nevertheless, they suffer from high linear birefringence effect as several meters of fiber are used as they have a relatively low Verdet constant. In this context, the bulk optic sensors look very attractive, as they allow a small the size of the sensing element and avoid some adverse effects for light propagation. This last type of sensors is actually the most implemented in industry.

The inline arrangement presented in Figure 1.16 can be modified to perform local measurement of magnetic field strength. To do this, the coil is replaced by some optical material exhibiting very high Verdet constant. The most recent example of such a miniaturized magnetic field sensors are based on Dy^{+3}-doped magnetite and ferrite nano-particles dispersed in a polymer matrix [49]. The production process is much complicated, but on the output, one gets a large MO response from the material. The sensor is based on an inline Sagnac interferometer design and operating on 1310 nm wavelength, at room temperature. For the thicknesses of the material around 500 µm, the measured noise floor is 20 fT without using synchronous detection. This has been possible because of the tremendous Verdet constant of the material equal to $32.2 \cdot 10^{7}$ deg·(T·m)$^{-1}$.

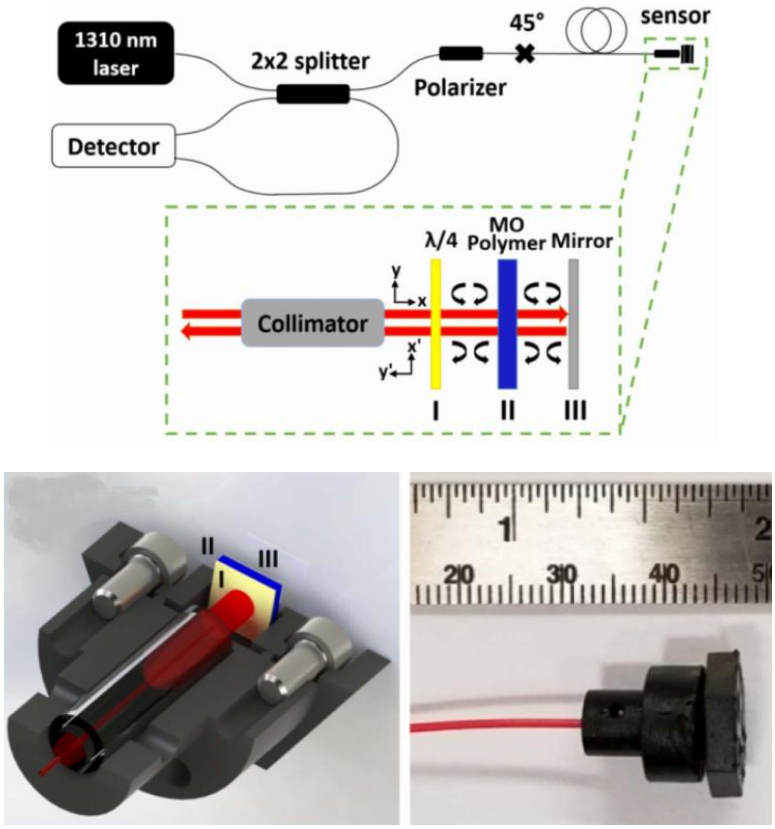

Figure 1.17: Schematic diagram of the in-line Sagnac interferometer magnetic sensor based on MO polymer. In-line Sagnac interferometer sensor design taken from [49].

The sensing part of the device contains almost the same optical elements combination of QWP and mirror to compensate the birefringence in the optical fiber (see Figure 1.16 and find the explanation in the previous subsection). The holder for the sensing part is manufactured on a 3D printer, which makes the production cheaper and easier. The 1.3 µm wavelength also is very attractive, as most of the fiber devices used for telecommunications work at this wavelength, and therefore the optical components are low cost and easily available.

1.3. Summary

A summary of the sensing parameters of the presented magnetic field detection technologies is provided in Table 1. The given values are indicative and they do not demonstrate all functional capabilities of the sensor devices, but they can be very helpful for comparison the next parameters as the sensitivity range, the noise, the footprint of sensing element.

Sensor technology	Sensitivity range	Noise [/√Hz]	Frq	Footprint	Comment
Inductive Sensors	20 fT – no upper limit	20 fT	DC - 1MHz		simple construction
Hall Effect Sensors	0.1 µT – 0.1 T	100 nT	DC – 1MHz	Limited by size of the semiconductor substrate 2.4 µm x 2.4 µm	suitable for large magnetic filed (> 1 T) Low cost;
Optically pumped sensors	1 nT – 1 T	10 fT		Limited by vapor cell, around 100 mm^3	128 °C work temperature
Fluxgate Sensors	0.01 nT – 10 mT	9 pT	DC – 10kHz	few mm	can be operated at temperatures between -180 °C and 200 °C with error ± 3 nT
Anisotropic magnetoresistance AMR sensors	10 nT – 5 mT	200 pT	DC – 1GHz	few mm	
Giant magnetoresistance GMR sensors	10 nT – 0.1 T	10 nT	DC – 1GHz	few mm	more sensitive at 4.2 K
SQUID Sensors	5 aT – 1 nT	3 fT	DC – 1GHz	0.5 mm – 1 cm	high power consumption; more sensitive at < 1 K; expensive;
Magneto-optical sensors	20 fT – no upper limit	20 fT	DC – 10kHz	Limited by the size of using material 2 µm	No need for isolation from electromagnetic sources

Table 1: Comparison of the sensing parameters of the magnetic field sensor technology.

It is very important to note that the real parameters of individual commercial sensors can vary strongly from the value given from one to another document since they depend on the implementation of the sensing technology, the nature of the used materials and the accuracy of the detections system. However, the information in Table 1 is more than enough to clearly demonstrate the excellent competitiveness of the MO sensing technology. The variety of sensing materials, which define the sensitivity range of the device, and the controllable size of the sensing element make these types sensors very attractive for use in applications going from the measurement of the Earth's magnetic field (mT) to magnetocardiography (nT).

Chapter 2

This chapter is deals with the origin of the MO effects such as the FR and the MCD taking place in MO materials under an applied magnetic field. We will describe the interaction of light with MO materials and give the relevant equations for the light propagation in Section 2.2. In Section 2.3 and Section 2.4, we will give the description of some instances of MO materials, which have being considered for applications and of their successful syntheses with a few examples.

2.1 Phenomenological description of the magneto-optic effect

2.2. Light propagation in magneto-optical materials

2.1. Phenomenological description of the magneto-optic effect

In Section 1.2.4. we presented equation (1.3), which shows the relation between the rotation angle of the polarization plane, the magnitude of the magnetic field B, the path length L of the light through the magnetized material (thickness of the material), and the Verdet constant V. The Verdet constant is specific to the material. It depends on its magnetic properties, on the operating conditions (temperature, stress…) and on the wavelength. One can illustrate the Faraday effect by considering linear polarized light, which propagates through the MO material placed under the influence of a magnetic field applied along the direction of propagation of the light. The linearly polarized wave can be decomposed as a superposition of two equal-amplitude circularly polarized waves, one circular left and one circular right (see Figure 2.1). The Faraday effect induces a circular birefringence and therefore different phase shifts along the propagation for the two circular polarizations. At the exit of the MO material, the recomposition of the two circular polarized waves results in a linearly polarized wave whose polarization direction is rotated around the direction of propagation by an angle θ_F with respect to the initial polarization. The MCD may also introduce polarization change. Here, the absorption for left and the right circularly polarized waves are different inside the material and their amplitudes at the exit are different and the resulting polarization is no longer linear, but elliptical (see Figure 2.1)

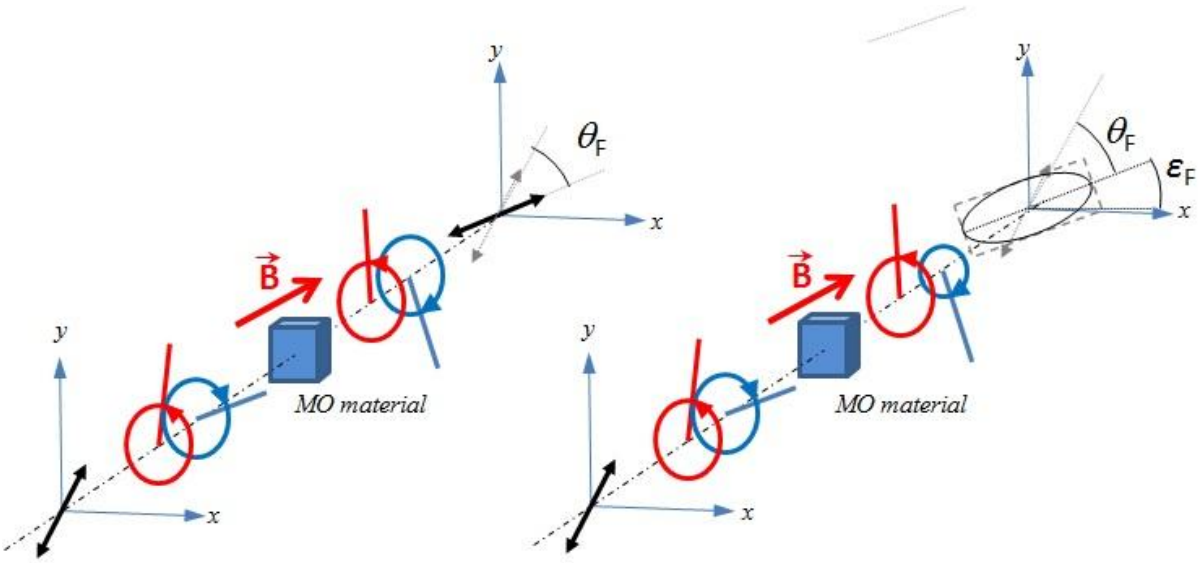

Figure 2.1: Polarization changes by FR (left picture) and MCD (right picture) in a MO material.

Because the FR depends on the orientation of the magnetic field, parallel or anti-parallel to the direction of the propagation of the light, its effect is a non-reciprocal on optical polarization. Figure 2.2 illustrates this property. The polarization of the light propagating in a direction parallel to the magnetic field experiences an anticlockwise rotation. Reflected back, the propagation direction is antiparallel to the magnetic field and the rotation is clockwise. As the two propagation directions are opposite, the two rotations add up. In the case of a birefringent medium (e.g. a half-wave plate) the two rotations compensate and the orientation of the polarization of the back-propagating light is the same as the incident one.

An example of application of the Faraday effect is the optical isolator which is used to prevent damage in optical systems due to the unwanted back-reflected light. To build the optical isolator the MO material has to induce a 45 degrees rotation in a single pass. Then, the back-reflected light experiences an additional 45 degrees rotation during the second pass and will be polarized at 90 degrees, perpendicular, to the incident polarization, thus the reflected light can be fully blocked by means of a polarizer.

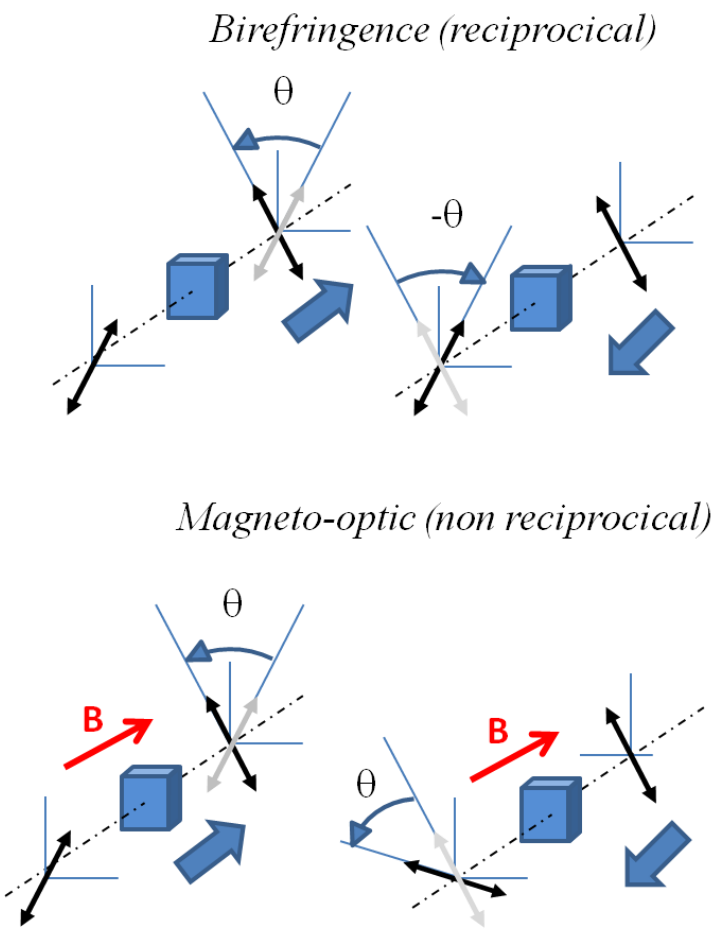

Figure 2.2: Scheme of reciprocal and non-reciprocal propagation through the active media.

2.2. Light propagation in magneto-optical materials

In Section 1.2.4., we introduced the MO effects as FR and MCD, resulting from the coupling between the light and the material under the influence of an external magnetic field. The aim of this section is to detail the electromagnetic description of the MO effect.

We consider a material with a magnetization $\boldsymbol{M}$ [50]. The properties optical of the materials are described by the constitutive equation:

$$\boldsymbol{D} = \varepsilon_0 \, \varepsilon \, \boldsymbol{E} \ , \tag{2.1}$$

where $\boldsymbol{D}$ is the electric displacement vector, $\boldsymbol{E}$ is the electric field, ε_0 is the vacuum dielectric permittivity and ε is the relative dielectric permittivity rank 2 tensor that depends on the magnetization and on the frequency of the fields. In general, the influence of the magnetic permeability of the material on optical waves is negligible and therefore considered to be equal to the vacuum magnetic permeability. Therefore we assume that the properties of the material are fully described in terms of its dielectric permittivity tensor expressed as:

$$\varepsilon = \begin{bmatrix} \varepsilon_{xx} & \varepsilon_{xy} & \varepsilon_{xz} \\ \varepsilon_{yx} & \varepsilon_{yy} & \varepsilon_{yz} \\ \varepsilon_{zx} & \varepsilon_{zy} & \varepsilon_{zz} \end{bmatrix}, \tag{2.2}$$

where x, y, z indexes represent the three cartesian coordinate axes. All the components of this tensor are complex, i.e. $\varepsilon_{mn} = \varepsilon'_{mn} + i\,\varepsilon''_{mn}$, and depend on the magnetization $\boldsymbol{M}$ and on the frequency.

The electric and magnetic fields $\boldsymbol{E}$ and $\boldsymbol{H}$ associated to the monochromatic light wave are given by:

$$\boldsymbol{E} = \boldsymbol{E_0} \exp[i(\boldsymbol{k}\cdot\boldsymbol{r} - \omega t)]\,, \tag{2.3 a}$$

$$\boldsymbol{H} = \boldsymbol{H_0} \exp[i(\boldsymbol{k}\cdot\boldsymbol{r} - \omega t)]\,, \tag{2.3 b}$$

where $\boldsymbol{E_0}$ and $\boldsymbol{H_0}$ are the vector amplitudes of the electric and magnetic components, $\boldsymbol{k}$ is the wave vector taken parallel to the z axis ($\boldsymbol{k} = k\boldsymbol{z}$), ω is the circular frequency of the wave. The interaction of the wave with the medium derived from the Maxwell equations (2.4 a) and (2.4 b):

$$\nabla \times \boldsymbol{E} = -\mu_0 \frac{\partial \boldsymbol{H}}{\partial t}, \tag{2.4 a}$$

$$\nabla \times \boldsymbol{H} = \varepsilon_0\, \varepsilon \frac{\partial \boldsymbol{E}}{\partial t}\,. \tag{2.4 b}$$

We consider a cubic material with internal magnetization $\boldsymbol{M}$ oriented in z-direction, i.e. $\boldsymbol{M}$ = M $\boldsymbol{z}$, the permittivity tensor element along OX and OY are equivalent. $\boldsymbol{M}$ induces an optical anisotropy. Therefore the permittivity tensor is invariant under an arbitrary rotation around axis z. This is expressed by equation (2.5):

$$\varepsilon = \begin{bmatrix} cos\varphi & sin\varphi & 0 \\ sin\varphi & cos\varphi & 0 \\ 0 & 0 & \pm 1 \end{bmatrix} \begin{bmatrix} \varepsilon_{xx} & \varepsilon_{xy} & \varepsilon_{xz} \\ \varepsilon_{yx} & \varepsilon_{yy} & \varepsilon_{yz} \\ \varepsilon_{zx} & \varepsilon_{zy} & \varepsilon_{zz} \end{bmatrix} \begin{bmatrix} cos\varphi & -sin\varphi & 0 \\ sin\varphi & cos\varphi & 0 \\ 0 & 0 & \pm 1 \end{bmatrix}, \tag{2.5}$$

where φ is the arbitrary angle of the rotation about the $\boldsymbol{z}$ axis and the ± signs indicates the proper (+) and improper (-) rotations, respectively. The general form of the permittivity tensor resulting from the latter equation is:

$$\varepsilon = \begin{bmatrix} \varepsilon_{xx} & \varepsilon_{xy} & 0 \\ -\varepsilon_{xy} & \varepsilon_{xx} & 0 \\ 0 & 0 & \varepsilon_{zz} \end{bmatrix}. \tag{2.6}$$

Substituting in to equation (2.4 a) and (2.4 b) the expressions of $\boldsymbol{E}$, $\boldsymbol{H}$ given by equations (2.3 a) and (2.3 b) one obtains:

$$\boldsymbol{k} \times \boldsymbol{E} = \omega\, \mu_0 \cdot \boldsymbol{H}\,, \tag{2.7 a}$$

$$\boldsymbol{k} \times \boldsymbol{H} = -\,\omega\, \varepsilon_0\, \varepsilon \cdot \boldsymbol{E}\,. \tag{2.7 b}$$

Using the relation $\boldsymbol{k} \times (\boldsymbol{k} \times \boldsymbol{E}) = \boldsymbol{k}(\boldsymbol{k}\cdot\boldsymbol{E}) - \boldsymbol{k^2 E}$, equations (2.7) become:

$$\boldsymbol{k}(\boldsymbol{k}\cdot\boldsymbol{E}) - \boldsymbol{k^2 E} + \mu_0 \varepsilon_0\, \omega^2 \varepsilon \cdot \boldsymbol{E} = 0\,. \tag{2.8}$$

We consider $\boldsymbol{N}$ parallel to $\boldsymbol{M}$, that is, the light propagates along the z-direction, i.e. $\boldsymbol{N}=\boldsymbol{k}/k_0=(0, 0, N)$. With $k_0^2 = \mu_0 \varepsilon_0\, \omega^2$, equation (2.8) becomes:

$$\begin{vmatrix} N^2 - \varepsilon_{xx} & -\varepsilon_{xy} & 0 \\ \varepsilon_{xy} & N^2 - \varepsilon_{xx} & 0 \\ 0 & 0 & N^2 - \varepsilon_{zz} \end{vmatrix} \begin{vmatrix} E_x \\ E_y \\ E_z \end{vmatrix} = 0\,. \tag{2.9}$$

Then, $D_z = \varepsilon_0 \varepsilon_{zz} E_z = 0$, that is, $E_z = 0$, and by solving (2.9) we get:

$$(N^2 - \varepsilon_{xx})E_z - \varepsilon_{xy}E_y = 0\,, \tag{2.10 a}$$

$$\varepsilon_{xy}E_x + (N^2 - \varepsilon_{xx})E_y = 0\,. \tag{2.10 b}$$

From the condition for non trivial solutions of E_x and E_y one obtains:

$$N_{\pm}^2 = \varepsilon_{xx} \pm i\,\varepsilon_{xy}\,, \tag{2.11}$$

$$\pm i\,E_x = E_y\,. \tag{2.12}$$

The normal modes of propagation are then:

$$D_+ = \varepsilon_0 N_+^2\left(E_x + iE_y\right), \tag{2.13}$$

$$D_- = \varepsilon_0 N_-^2\left(E_x - iE_y\right). \tag{2.14}$$

They correspond to circularly polarized waves in the plane XY. It follows that the right (with refraction index N_+) - and left (with refraction index N_-) -circular polarized waves have different refractive indices and thus different phase velocities in the medium. Reconsidering the decomposition of a linearly polarized wave into right and left circularly polarized waves described in Paragraph 2.1, the rotation of the linear polarization can be simply expressed by the phase shift between right and left circular components after the propagation through the magnetized medium. It corresponds to the FR angle θ_{F} and is given by equation (2.15):

$$\theta_{\mathrm{F}} = \frac{\omega \cdot l}{2c} \cdot Re(N_+ - N_-), \tag{2.15}$$

where l is the interaction length and c the celerity of light. This corresponds to FR when the electromagnetic wave propagates in the direction of the magnetization vector (**k** ↑↑ ***M***). If the direction of the propagation of light is reversed (**k** ↑↓ ***M***), when **k** = (0,0, -k), then the sign of θ_{F} changes.

The imaginary part of the refractive index is related to the absorption. Again, considering the description in paragarph 2.1, the difference of absorption for right and left circular polarization components of the linear polarization introduces some ellipticity. The ellipticity is the ratio of the lengths of the major and minor axis of the ellipsoid. It is given by equation (2.16):

$$\eta_{\mathrm{F}} = \frac{\omega \cdot l}{2c} \cdot Im(N_+ - N_-). \tag{2.16}$$

The FR angle and Faraday ellipticity (FE) can be written as a function of two elements of the permeability tensor after several variable replacements:

$$\theta_{\mathrm{F}}(\omega) = -\frac{\omega \cdot}{2c} \cdot \frac{\varepsilon_{xy}''}{n}, \qquad \eta_{\mathrm{F}}(\omega) = -\frac{\omega \cdot}{2c} \cdot \frac{\varepsilon_{xy}'}{n}\,. \tag{2.17}$$

These elements can be calculated from the microscopic modeling of the charge carrier behaviour in the material. In the next section, we give some examples of MO materials and comment their properties.

2.3. Bulk Magneto Optical materials

2.3.1. (LaSr)MnO_3

2.3.2. Cobalt ferrites $CoFe_2O_4$

2.3.3. Barium ferrite $BaFe_{12}O_{19}$

2.3.4. Semiconductor $CdCr_2S_4$

2.3.5. Ferric borate and ferric fluoride

2.3.6. Chromium trihalides: CrCl3, CrBr3, Cr I3

2.3.7. Europium chalcogenides films

2.3.8. Terbium gallium garnet (TGG)

2.4. Evolution of MO materials

2.4.1. Europium chalcogenides nanoclusters

2.4.2. Cobalt ferrites nanoparticles

2.4.3 Magneto plasmonic crystals

2.4.4. Organic materials

2.5. Yttrium iron garnet (YIG)

2.3. Bulk Magneto Optical materials

The present section focuses on the description of some of MO materials that were being considered for MO applications. We give some elements of comparison in order to show the situation of the Bi: YIG among the large variety of the MO material considering the physical properties and the methods of preparation.

First, we present the FR spectrum (Figure 2.3) of different MO materials mainly extracted from the book of A. K. Zvezdin and V. A. Kotov [51] in 1997. The review collected many of the research works in the investigation of MO properties of various bulk materials which are relevant for our project. We present briefly their structures, preparation methods, and MO properties. In Table 3 below, we present the value of the FR, the Kerr rotations for MO materials presented in this section and their preparation methods.

In the second part, to complete this first review and to illustrate the evolution of MO materials, we present more recent magnetic materials and structures which exhibit huge values of FR.

The last section is dedicated to the Bi: YIG only. Here, we present in more detail its structure and its properties focusing on the influence of the bismuth substitution on the MO effect. Finally, we conclude on the different preparation methods of the garnet.

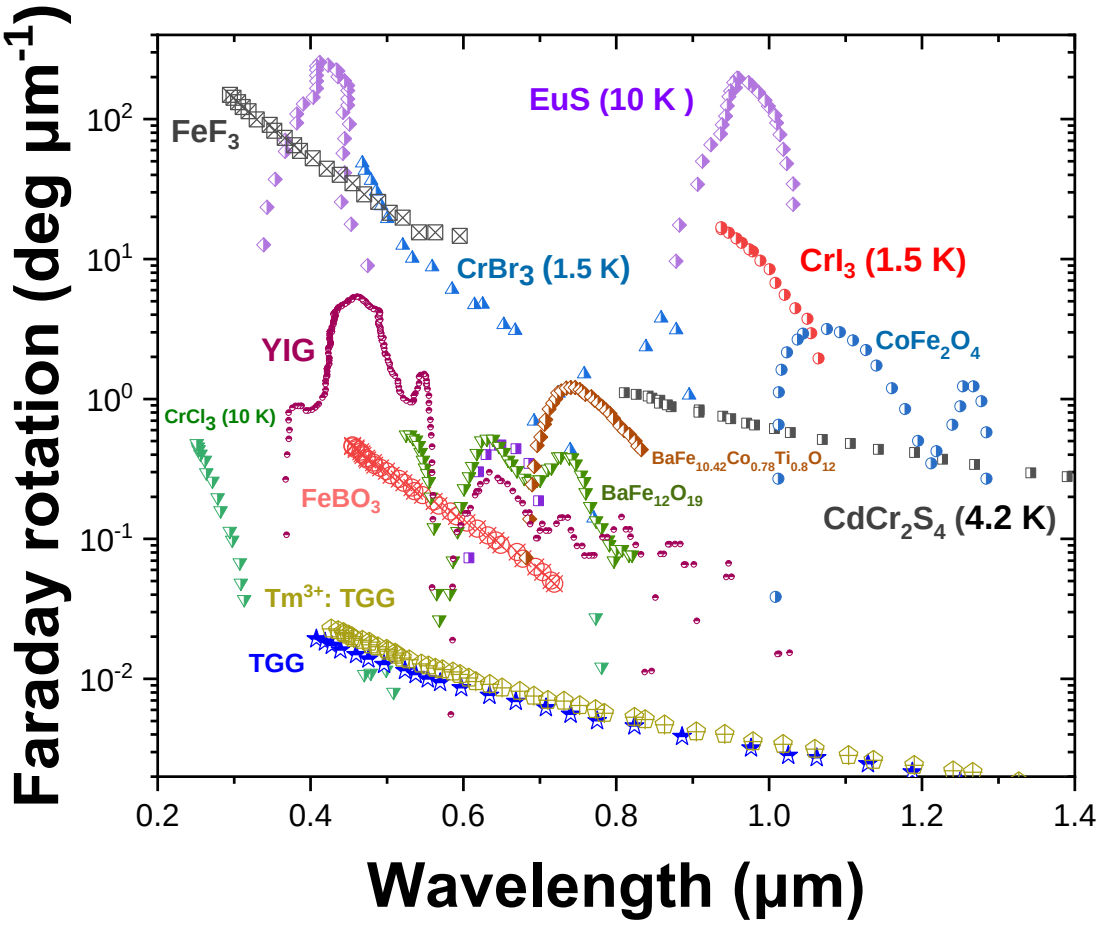

Figure 2.3: The spectral dependence of the FR for $La_{0.82}Sr_{0.18}MnO_3$ [52], measured and calculated for $CoFe_2O_4$ [53], $BaFe_{12}O_{19}$ and $BaFe_{10.42}Co_{0.78}Ti_{0.8}O_{12}$ [54], $FeBO_3$ [55], and for FeF_3 [56], $CdCr_2S_4$ at 4.2 K [57]; .$CrC1_3$, $CrBr_3$ and CrI_3 at 1.5 K in saturating magnetic filed [58], EuS films at 10 K and H = 4 T [59], Tm^{3+}: TGG and pure TGG [60].

Figure 2.3 shows the value of FR for the MO materials presented in this section. For ease of comparison, we indicate FR values for each material in the same graph mentioning the temperature for which the highest FR was achieved. The monochalcogenides (EuS), Chromium trihalides (CrI_3, $CrBr_3$), ferric fluoride (FeF_3) show a higher FR value compared with the other MO materials, but an operating temperature below 10 K is required. Some of these materials are difficult to prepare and/or require expensive preparation setups, which makes them unattractive for fast and cheap material production. In the case of ferric borate and of ferric fluoride, the material preparation process takes 3 weeks with annealing temperature at 800 °C, which is also not motivating. The stability at high temperature and pressure is a very important parameter, which only a few of the presented materials possess. In Table 3 below, we present the value of the FR, the Kerr rotations for MO materials presented in this section and the way of their preparation.

MO material	FR (deg μm^{-1})	Kerr rotation (deg)	Method of preparation	Disadvantages
Manganites ($La_{1-x}Sr_xMnO_3$)	-5 at 400 nm	2.3 at 300 nm (78 K)	Ceramic process RF sputtering Sol-Gel PLD	The annealing process needs to occur under the O_2
Co-containing ferrimagnetic spinels ($CoFe_2O_4$)	0.37 at 632 nm	0.23 at 632 nm	Sol-Gel technique RF sputtering	Tetrahedral and octahedral sites may exist at the same time
Hexagonal ferrites ($BaFe_{12}O_{19}$)	0.51 at 630 nm	0.14 at 670 nm	CSD Rf sputtering PLD	Strong optical absorption in visible region
Chalcogenide spinels ($CdCr_2S_4$)	1.1 at 810 nm (80 K)	-3.5 at ~840 nm (for $CoCr_2S_4$ at 80 K)	Cold pressing Solid-State reaction technique	Special technique as hot pressing (up to 50 kpsi) is required
Ferric borate ($FeBO_3$)	0.46 at 454 nm	-	Powder technique Flux-grow technique Gas phase growth	There is no FR in the plane (111)
Chromium trihalides ($CrBr_3$)	$4.8\cdot10^1$ at 468 nm (1.5 K)	-	Grown by chemical vapor transport method	Operability only at T < 1.5 K
Europium oxides and monochalcogenides (EuS)	$2.5\cdot10^2$ at 412 nm (10 K) $1.96\cdot10^2$ at 0.958 nm (10 K)	8 at 688 nm	Solid phase Liquid phase CVD	Operability only at T < 10 K

Table 2: Value of the FR, the Kerr rotations for MO materials presented in this section and the way of their preparation.

2.3.1. (LaSr)MnO$_3$

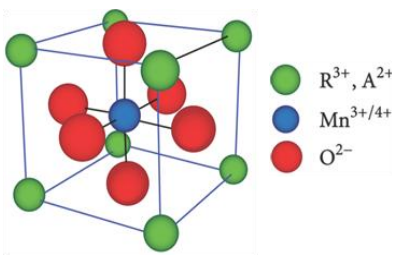

Figure 2.4: Lanthanum manganese oxides can be prepared via different methods: ceramic process [61], sol-gel [62], [63], radio frequency (RF) sputtering [52], pulsed laser deposition (PLD) [64].

Manganites present a perovskites-type structure with general formula $R_{1-x}A_xMnO_3$ where R = La and A = Ca, Sr, Ba, Pb (see Figure 2.4). They are composed of oxygen octahedra with Mn atoms in the center and crystallize in the orthorhombic system. The material is considered for MO recording because of its strong Kerr rotation and ferromagnetic properties.

Popma and al. [61] have studied the MO properties as the Kerr effect of $Bi_xLa_{0.7-x}Sr_{0.3}MnO_3$ prepared via the ceramic process in the range 250 – 700 nm at 78 K and at 300 K. The highest value they have obtained was 2.3 deg, measured at a temperature of 78 K and at 290 nm, for the composition with x = 0.25. At room temperature (300 K) and at the same wavelength this value was found to be smaller by a factor 10.

The FR and FE of (LaSr)MnO_3 polycrystalline films prepared by RF sputtering, were studied in [52] in the range 400 – 750 nm spectral range. The crystalline films of lanthanum manganese oxide were easily grown by sputtering at low temperatures 170 °C on silica and $Gd_3Ga_5O_{12}$ (GGG) substrates. The best performances of FR and FE ($\Theta_F = -2.6\cdot10^4$ deg·cm^{-1} at 428 nm and $\eta_F = -5\cdot10^4$ deg·cm^{-1} at 400 nm) were obtained for the film with x = 0.18 deposited at 500 °C on the substrate under pure O_2, and annealed in an O_2 atmosphere at 900 °C.

Lanthanum manganese oxides demonstrate a good performance of MO properties only at the low temperature of 78 K, which requires a cooling system for use. For the material preparation, a difficult technique is also required as RF sputtering or PLD. Therefore, this material is not the most convenient for our purposes.

2.3.2. Cobalt ferrites $CoFe_2O_4$

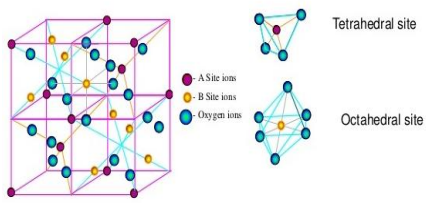

Figure 2.5: Crystal structure of Spinel Ferrite with general formula AB_2O_4, where A = divalent metallic cations (eg. Mn^{2+}, Ni^{2+}), B = trivalent cations (eg. Fe^{3+}, Al^{3+}).

Spinel ferrites have a general formula is AB_2O_4, $\mathbf{Me}^{2+}\ Fe^{3+}{}_2\ O_4$ for iron spinels, where **Me** can be one of the following metallic cations: Co^{2+}, Zn^{2+}, Ni^{2+}, Mn^{2+}, etc... (see Figure 2.5). One of the most representative classes of these materials exhibiting high value of FR is the cobalt-ferrites. Usually, the films cobalt-containing ferrimagnetic spinels are prepared by the sol-gel process, where it is deposited on silica or relevant substrate for the annealing process in the range of temperatures 700 - 1000 °C.

The Faraday and Kerr rotations for $CoFe_2O_4$ have been studied in [53]. In this work, two major peaks for FR at 632.5 nm and 799.8 nm were observed and measured to be $3.7{\cdot}10^3$ and $3.3{\cdot}10^4$ deg cm^{-1}, respectively. The dependence of FR on annealing temperature ranging from 400 to 600 °C for 2 hours under normal atmosphere was studied in the wavelength range from 600 to 800 nm for films of $CoFe_2O_4$ prepared by RF sputtering on quartz substrates [65]. The positive evolution of FR with increasing annealing temperature was observed, and the highest value of $4{\cdot}10^4$ deg·cm^{-1} was obtained at the annealing temperature 600 °C at 740 nm.

There are various methods for the preparation of Co-containing ferrimagnetic spinels, but each of them requires complex types of equipment and processes. This material is also difficult to implement for the type of sensor device we have in mind.

2.3.3. Barium ferrite

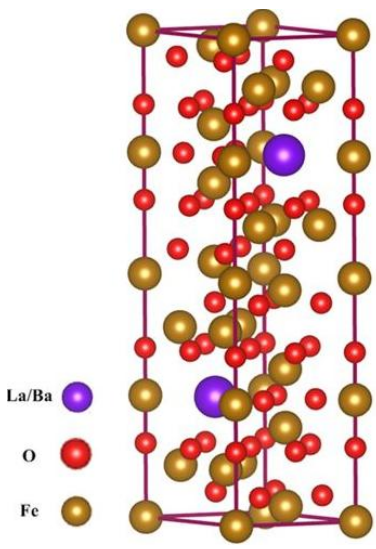

Figure 2.6: The unit cell for $Ba_{1-x}La_xFe_{12}O_{19}$ (where purple, red, and gold spheres correspond to Ba/La, O and Fe atoms respectively) taken from [66].

The study and development of hexagonal ferrite ceramics started in the 1950s with the synthesis of the naturally magnetic mineral magnetoplumbite containing lead and iron oxides. The general formula is $AFe_{12}O_{19}$ were A = Ba, Sr, Ca, Pb. Very often, the cations of hexagonal ferrites are replaced by barium or strontium (see Figure 2.6). This material became popular due to its strong anisotropy with an axis perpendicular to the surface [67, 68].

The strong absorption in the visible range limits the observation of MO to the 1 – 8 μm range [69]. However, with $PbFe_{12}O_{19}$ [70], the substitution of iron ions by Al^{+3} can improve the optical transparency in the visible region, but it also decreases the FR.

Hexagonal ferrites can be prepared by flux method [71], sol-gel [72], or by PLD process [54]. Prepared by PLD, the components are deposited on a hot substrate (850 °C) under oxygen working gas at 0.2 mbar and result in single-phase crystals [54]. Nakamura et al. [54] demonstrated that the FR of $BaFe_{12}0_{19}$ in the near infra-red region between 1770 nm and 1240 nm and at 730 nm can be enhanced by cobalt substitution. The FR of $BaFe_{12}O_{19}$ and $BaFe_{10.4}C_{0.8}Ti_{0.8}O_{12}$ in the spectral range 520 – 830 nm are shown in Figure 2.3.

The strong optical absorption of Hexagonal ferrite ceramics in the visible range will reduce the efficiency of our MO sensor operating at 532 nm. Therefore, we abandoned the idea of using it, however, it could be promising to consider this material when working in the infrared region.

2.3.4. Semiconductor $CdCr_2S_4$

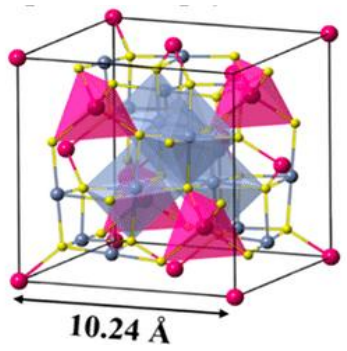

Figure 2.7: The unit cell for $CdCr_2S_4$, where Cr atoms (blue balls) occupy the octahedral sites, and Cd atoms (pink balls) occupy the tetrahedral sites, S atoms (yellow balls) taken from [73].

The ferromagnetic semiconductor $CdCr_2S_4$ has a face-centered-cubic spinel structure and is related to chalcogenide spinels with the general formula ACr_2S_4. The space group of $CdCr_2S_4$ is *Fd3m* with octahedral Cr^{3+} and tetrahedral Cd^{2+} surrounded by sulfur ions (see Figure 2.7). $CdCr_2S_4$ is well known because of its colossal magnetoresistance, magnetic field induced structural transformations, and giant redshift of the absorption edge. It is transparent in the spectral range 0.9 – 14 μm.

In the 70's, the chalcogenide spinels samples were prepared by cold pressing [74]. Nowadays, the solid-state reaction and chemical transport reaction method are preferred [75].

The FR spectrum of hot-pressed films of $CdCr_2S_4$ at 4.2 K performed by [57] is given in Figure 2.3 in the spectral range 0.8 – 1.4 μm.

The operating temperature for $CdCr_2S_4$ and $CoCr_2S_4$ is $T = 80$ K or below which makes them unattractive and difficult to use.

2.3.5. Ferric borate and ferric fluoride

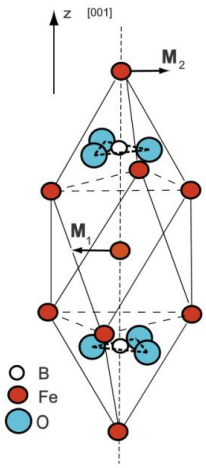

Figure 2.8: Crystal structure of $FeBO_3$, where red balls represent Fe atoms, white balls represent B atoms, and blue balls represent O atoms taken from [76]. M_1 and M_2 are the magnetic moments of the Fe^{3+} ions.

$FeBO_3$ and FeF_3 represent materials which are related to ferromagnetic crystals. $FeBO_3$ has the rhombohedral calcite structure and the general formula $Fe_{1-x}M_xBO_3$ where M is the metal ion of Cr^{3+}, Ga_{3+}, or Ti^{3+} (see Figure 2.8). In both materials, all of the iron spins are parallel to the (111) plane. The crystal has a specific green color and good transparency in the visible region at room temperature [77].

Ferric borate can be grown from Fe_2O_3 – B_2O_3 – PbO/PbF_2 using the flux-grow technique [78], or from powder using Joubert's method [79], or from the gas-phase. In [80], $Fe_{1x}M_xBO_3$ powders obtained after slow heat procedure going from 200 to 500 °C, and maintaining 500 °C for 12 hours. In the final process, it is annealed in air at around 800 °C for 3 weeks. It has also been demonstrated, that the thermal stability of $Fe_{1-x}M_xBO_3$ increases with x. [80].

The Faraday rotation, birefringence, and optical absorption spectra for $FeBO_3$ [55] and FeF_3 [56] were studied, and the FR spectra for these materials are shown in Figure 2.3.

The preparation of $FeBO_3$ and FeF_3 requires several weeks of heat treatment at 800 °C. This is needed to avoid the appearance of other phases in the material. The long procedure of preparation makes the material unattractive for use.

2.3.6. Chromium trihalides: CrCl3, CrBr3, Cr I3

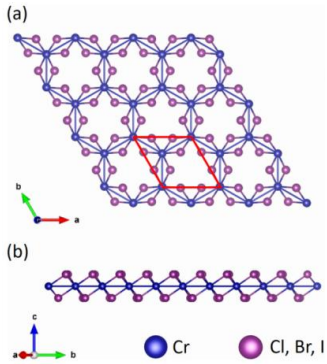

Figure 2.9: Atomic structure of monolayer CrX_3 (X = Cl,Br,I), where blue balls represent Cr atoms, and pink balls represent Cl, Br, I atoms taken from [81]. (a) Top view and (b) side view of a single layer.

In 1966, Dillon et al. [58] gave an exhaustive description of ferromagnetic chromium trihalides, including structural, optical, and MO properties. This type of material is relatively transparent in a wide spectral range and has a huge FR, which may be observed at low temperatures below 1.5 K. $CrC1_3$ and $CrBr_3$ have a similar covalently bonded layered crystal structure at low temperatures. The hexagonal network of Cr^{3+} ions is placed in between two close-packed layers of halogen ions (see Figure 2.9). The bonds inside each layer are mainly covalent, while Van der Waals interactions bind the layers. It is assumed that CrI_3 can have the same structure.

Single crystals of CrX_3 where X = Cl, or I are obtained by chemical vapor deposition, where polycrystals of CrX_3 are placed in vacuum at approximately 850 K for 150 hours. Next, these materials are used to assemble a layered structure of graphite/CrX_3/graphite exfoliated using polydimethylsiloxane (PDMS)-based gel [82].

The FR spectra of chromium trihalide materials were measured at 1.5 K at saturation (> 0.25 T) and is presented in Figure 2.3.

While CrX_3 has the highest FR properties among all the presented MO materials, they degrade quickly in an air environment, which will severely limit the MO sensor lifetime.

2.3.7. Europium chalcogenides films

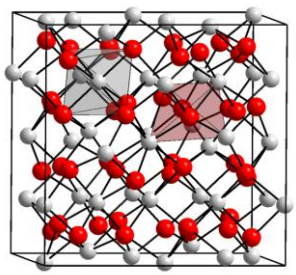

Figure 2.10: Crystal structure of EuO, where white balls represent Eu atoms, red balls represent O atoms.

The EuS has a simple crystal structure similar to the structure of common salt (see Figure 2.10)

The studies of MO properties of europium chalcogenides films (EuX, where X = O, S, Te, and Se) have been started in the early ’70s. The crystal is structure shown in Figure 2.10. Reference [83] presents the FR and the MCD spectra for 100 – 200 nm thin evaporated films of EuS at magnetic saturation at H = 10 T and at 2.5 K. The value of the first maximum of FR was observed at 282 nm where it reaches $2.5{\cdot}10^6$ deg·cm^{-1} and the second maximum at 577 nm where it reaches $2{\cdot}10^6$ deg·cm^{-1} (see Figure 2.3). The Kerr rotation spectrum and ellipticity for europium oxide single crystals at T = 10 K and H = 4 T were studied by Wang et al. [59]. A maximum Kerr rotation of 7.1 deg was observed at 885 nm and at 10 K.

The fist synthesis of bulk EuX (X = O, S) has been demonstrated by Shafer M. in 1965 [84]. In his work, the solid-phase reactions of Eu_2O_3 and chalcogens (oxygen or sulfur sources) at high temperature above 1000 °C were used. During the preparation, chemical and physical instabilities in materials were reported.

The difficult preparation of materials and low temperature (10 K) operation requirements make europium oxides and europium monochalcogenides unattractive for use in our MO sensor device.

2.3.8. Terbium gallium garnet (TGG)

In addition, we present terbium gallium garnet (TGG) and doped materials, which have not been mentioned in [51].

TGG is related to synthetic minerals, with the general formula $Tb_2Ga_5O_{12}$. This material is still under study for MO applications and especially for high power faraday isolators [85 - 87], since it shows great transparency and high FR. Also, due to its MO properties it can be used in magnetic field sensing as well as in optical circulators of fiber optic systems.

The TGG films can be prepared via the Czochralski method in Ir crucibles with (RF) induction heating [60, 88].

The Verdet constant for TGG materials have a strong dependency on the wavelength [89] and operation temperature [90]. A value for the Verdet constant of -74 $deg\cdot(T\cdot cm)^{-1}$ and of 21 $deg\cdot(T\cdot cm)^{-1}$ was measured at 362 nm and at 1064 nm respectively at room temperature. Its temperature dependence has been studied in the range from 300 K down to 4.2 K. At low temperature (4.2 K) a Verdet constant of $18\cdot10^4$ $deg\cdot(T\cdot cm)^{-1}$ has been measured at 1053 nm, which is 87 times higher than at room temperature.

The doping by various ions may enhance the MO properties: Ce^{3+}, Pr^{3+}, Nd^{3+}, Tm^{3+}, Dy^{3+}. Thulium (Tm^{3+}) doped TGG shows a FR of 165 $deg\cdot cm^{-1}$ at 532 nm, at 1.2 T, and at room temperature, which is 25% higher than for pure TGG [60] (see Figure 2.3). Dysprosium (Dy^{3+}) doped TGG exhibits a FR of 180 $deg\cdot cm^{-1}$ at 532 nm at 1.2 T, and room temperature, which is 50% higher than for pure TGG [88].

Since the preparation process requires a high temperature of more than 1200 °C, we discarded this option for our purposes. However its high damage threshold qualifies TGG for high fluence operations.

2.4 Evolution of MO materials

The MO materials described in the review [51] has now been synthesized in a new manner, where the particle size falls into the nanoscale, and in this case new optical and magneto-optical properties for these nanoparticles have be founded. In the first subsection, we present the examples of nanoparticles (Europium chalcogenides nanoclusters and Cobalt ferrites nanoparticles). One of the promising ways to use these nanoparticles in the enhancement of MO properties is to develop magnetoplasmonic structures, where the magnetic nanoparticles are covered with noble metals (for example gold). Notice that MO materials in the form of films can be combined with noble metal nanoparticules to achieve the same goal. This type of structure allows enhancing the interaction between the material and light by surface plasmon resonances. The building of this type of complex structure becomes possible only because of access to nanofabrication techniques (lithography, physical vapor deposition, nanoimprint and etc.). In the last subsection, we will present the organic polymer materials, whose huge MO properties have been discovered recently while the origin of its FR is still remains unknown.

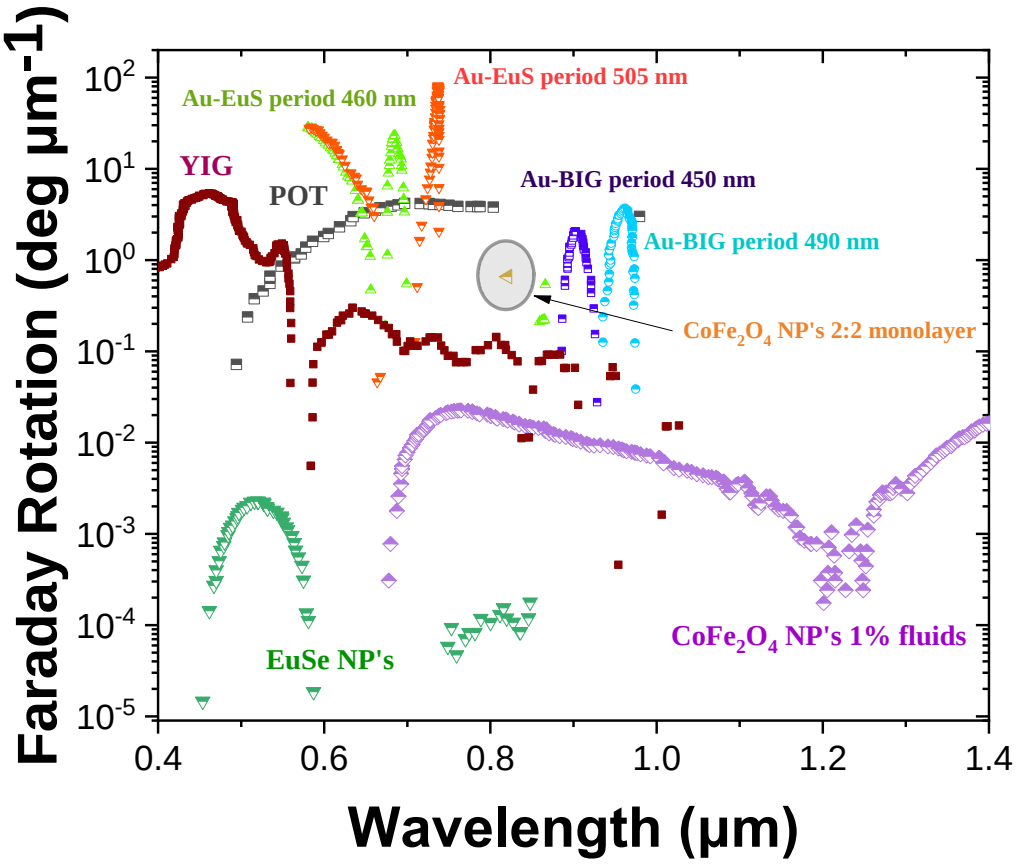

Figure 2.11: The spectral dependence of the FR for $CoFe_2O_4$ NP's 1% fluids and $CoFe_2O_4$ NP's 2:2 monolayer [91], poly(3-octyloxy thiophene POT [92], Au-BIG with period 450 nm and 490 nm [93], Au-EuS with period 460 nm and 505 nm [94], EuSe NP's [95].

Figure 2.11 shows FR amplitude spectrum in the range 0.4 – 1.4 µm for the set of MO materials presented in this section. For ease of comparison, we included the FR spectrum for YIG as we did in Figure 2.3 measured at 20 K.

2.4.1. Europium chalcogenides nanoclusters

Nowadays, the optical and MO properties of EuX have been very well studied and new perspectives in synthesizing EuS nanoparticles and their use in different applications are described in [95, 96]. In 2003, the first synthesis of EuX nanocrystals based on liquid-phase reactions of europium metal in liquid ammonia was reported [97, 98]. Presently, Eu films are fabricated by chemical vapor deposition (CVD), which avoids the use of high temperatures and toxic substances.

Optical and MO properties such as FR and MCD of EuX nanocrystals in poly(methyl methacrylate) (PMMA) films have been studied in [97, 98]. A Verdet constant of 1500 deg $(T\cdot m)^{-1}$ for the major peak at 580 nm was measured for a concentration of 5.3wt% in EuS clusters.

The effect of increasing the particle size on the amplitude of the FR around 620 nm was discovered in [98, 99].The doping process of EuS with Au improved the MO properties and also produced an effective photoswitchable Faraday effect [100]. The MCD spectra for the EuS-Au nanosystem at 670 nm changes reversible under light irradiation, which can be used for a new type of fiber optic communication devices.

2.4.2. Cobalt ferrites nanoparticles

Cobalt ferrite nanoparticles are quite promising in the formation of nanowires for potential magneto-optical data storage. Its FR has been studied in the range 500 - 1000 nm at room temperature in [101]. A maximum in absolute value for the Verdet constant of 160 $deg\cdot(T\cdot cm)^{-1}$ has been measured at 725 nm. The saturation of the magnetization is reached at 1.5 T. The FR measurements of size sorted cobalt ferrite fluids as a function of cobalt iron concentration in the 550 - 1550 nm range was studied in [102]. The highest FR amplitude measured was 25 deg cm^{-1} for 12.5 nm particles at 850 nm. This result were compared with the FR of γ-Fe_2O_3 particles [102]. In [103] the FePt nanoparticles were also studied as a function of core diameters from 1.9 to 9.3 nm in block copolymer (BCP). The highest value of the Verdet constant obtained for a 9.3 nm composite at 845 nm was $5.34\cdot10^4$ $deg\cdot(T\cdot m)^{-1}$.

The dependency of FR on operation temperature in the 40 - 201 K range has been studied for $CoFe_2O_4$ composite films between two BK7 glass substrates [104]. A Verdet constant of 1369 $deg\cdot(T\cdot cm)^{-1}$ at 532 nm has been obtained by cooling the temperature from 201 K down to 40 K. In this case, the Verdet constant increased by a factor of 4 compared with the value measured at 201 K.

The $CoFe_2O_4$ nanocomposite (nearly monodisperse cobalt ferrite nanoparticle-based polymer composites) were used in developing the optical magnetometer with a sensitivity of 50 nT / $\sqrt{Hz}$. The Faraday rotation is about 11 deg cm^{-1} at 980 nm and the Verdet constant is equal to $1.2\cdot10^4$ $deg\cdot(T\cdot m)^{-1}$ [105].

$CoFe_2O_4$ magnetic nanoparticles are also used in the building of magnetophotonic crystals (MPC's), where there are embedded in a SiO_2/ZrO_2 matrix. MPC elements are based on the non-reciprocity of the FR. The FR as a function of volume fractions for $CoFe_2O_4$ magnetic composites in the 1540 - 1560 nm range were studied in [106]. A maximum value of about 50 degrees for FR was obtained at 39% volume fraction (concentration of magnetic nanoparticles of $CoFe_2O_4$).

The MPC's can be prepared by embedding cobalt ferrite nanoparticles in the silica matrix via the sol-gel process (vertical deposition method was used to fabricate the direct opals) [91]. The FR of samples prepared with a 1% volume fraction of cobalt ferrite measured in the 620 – 1520 nm range. Two major peaks in the FR spectrum were observed at 750 nm and at 1550 nm. Their amplitudes were found to be 225 deg cm^{-1} and 310 deg cm^{-1} respectively (see Figure 2.11).

Europium chalcogenides nanoclusters and Cobalt ferrites nanoparticles could be promising to consider this material for our application, but YIG shows the higher FR compare to these nanocomposites.

2.4.3. Magneto plasmonic crystals

The investigations of FR in plasmonic materials have been started from the synthesis of γ-Fe_2O_3-Au core-shell nanostructures [107]. The FR spectrum for the γ-Fe_2O_3 nanoparticels, the mixture of γ-$Fe2O_3$, and Au nanoparticles, and Au coated γ-Fe_2O_3 nanopartiecles have been studied in the 480-690 nm range. An enhancement of FR around 530 nm was observed. The enhancement effect of the MO properties in this type of materials is lies in the overlap of the MO effects and the propagating surface plasmons.

Magneto-plasmonic crystals are materials where a metallic grating made of noble metal (gold) is lithographed on a thin layer of magneto-optical material such as ferromagnetic dielectric BIG, itself synthesized on glass substrate. This type of layered materials use the transverse magneto optical Kerr effect (TMOKE) [93] for back reflection or FR. The study of TMOKE as a function of the angle of the incident light was studied in [93].

The FR spectrum strongly depends on the periodicity of the grating of the top gold layer. The sample with a periodicity of 495 nm (120 nm wide and 65 nm thick nanowires) shows 0.80 deg of rotation at the 963 nm peak, which is higher by almost a factor 9 compared to BIG film without the metal grating layer [108].

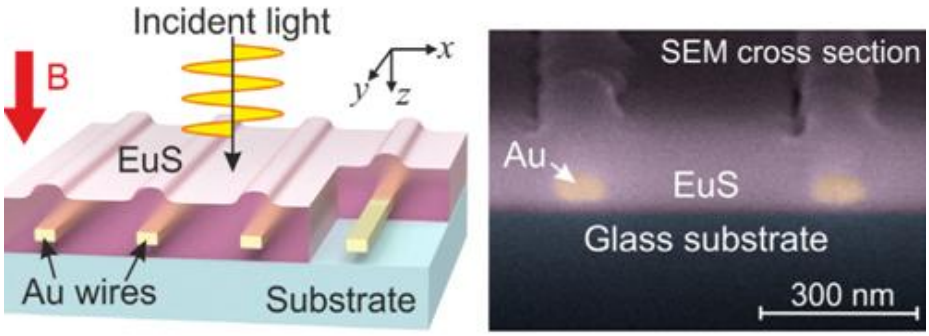

a. b.

Figure 2.12:(a) Schematic drawing of the structure of Au-EuS. (b) Colorized scanning electron micrograph of the sample cross section taken from [94].

Glass substrate coated by periodic Au-EuS thin films have been embedded with gold naonowires (EuS film with a 139 nm thick and gold nanowires 33 nm x 85 nm). The highest value FR has been obtained for the sample with a 505 nm periodand attained 14 deg at 5 T, 737 nm, and 20 K temperature (see Figure 2.11). At 250 mT the FR is about 4.9 deg [94].

Magneto plasmonic crystals show a huge value of FR, but the material preparation requires a difficult technique such as lithography, which increases their cost. Therefore, this material is not the most convenient for our purposes.

2.4.4. Organic materials

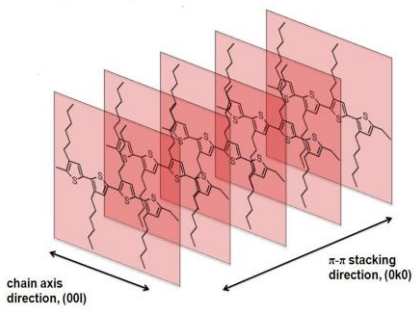

Figure 2.13: Structure of P3HT

The optical properties of conjugated polymers are defined by the charge transfer in the molecular chain and by intermolecular interactions. In [109] the organization of the molecule as π-conjugated and/or π-stacked structures leads to enhancement of MO properties. The Verdet constants measured for poly(arylene ethynylene) (PAE), for regioregular poly(3-hexylthiophene) (RRP3HT) and regioregular poly(3-dodecylthiophene) (RRP3DT) at 632 nm, are $2.50\cdot10^5$ deg $(T\cdot m)^{-1}$, $2.03\cdot10^5$ deg $(T\cdot m)^{-1}$, and $1.14\cdot10^5$ deg $(T\cdot m)^{-1}$ respectively.

The conjugated polymers poly(3-octyloxy thiophene) (POT) show great solubility in organic solvents, which makes them good candidates for simple spin coating on various substrates. The optical studies show a strong absorption in the 400 – 800 nm range and fully transparency in the infrared region [92]. The Verdet constant was studied from 800 nm to 1549 nm. It decreases linearly from $25\cdot10^5$ deg$\cdot(T\cdot m)^{-1}$ at 800 nm to $10\cdot10^5$ deg$\cdot$ $(T\cdot m)^{-1}$ at 1549 nm.

Organic materials such as an acrylate polymer/magnetite nanoparticle composites show huge values of for their Verdet constants around 10^6 deg $(T\cdot m)^{-1}$ in poled films [110]. This type of material was used in fiber MO sensor devices, and have demonstrated sensitive measurements of weak magnetic fields around 100pT at frequency 20 - 1000Hz. In [111] the optical properties in the 300 - 1200 nm range and the MO properties as a function of magnetic flux density in the 30 - $120\cdot10^{-4}$ T range have been studied for RRP3HT and RRP3DT. The optical absorption study showed a major peak at 550 nm for both RRP3HT and RRP3DT. Linear evolutions of the FR with increasing magnetic field were observed. The Verdet constants at 532 nm for RRP3HT and RRP3DT are $6.25\cdot10^4$ deg $(T\cdot m)^{-1}$ and $2.06\cdot10^4$ deg $(T\cdot m)^{-1}$ respectively.

Up to now, the origins of FR in conjugated polymers are still unclear. Some considerations involving the spin-orbit coupling related to the sulfur atom have been proposed, but the influence of the chiralilty of the molecular organization has also considered [112].

The studies of MO properties of organic materials, and especially of conjugated polymers, are still at their beginning. The degradation under light emission can severely limit their lifetime, but the huge MO properties, their ease of preparation and of implementation made them very promising for sensing applications.

The next section is dedicated to the yttrium iron garnet materials that have been used in the present work. They fulfill the conditions required for our application, demonstrating high FR under normal conditions and offering ease of preparation.

2.5. Yttrium iron garnet (YIG)

The yttrium iron garnet material ($Y_3Fe_5O_{12}$, YIG) is an extensively studied ferrimagnetic compound, widely used for microwave devices (filters, resonators) or as model materials for magnonic [113]. The YIG is also largely used for its MO properties, related to the Faraday effect, for the fabrication of optical devices: optical isolator [114 - 117], birefringent compensators, magnetic field sensing [118], [119] and magneto-optical visualization setups [120].

One of the main advantages qualifying the Bi: YIG for these applications is its Curie temperature (T_c = 550 K for YIG) which allows a good operability at high temperatures.

Structure of YIG

YIG has a cubic unit cell with space group O_h^{16} (Ia3d) with eight formula units of $\{Y_3\}[Fe_2](Fe_3)O_{12}$. The unit includes cell 24 Fe^{3+} ions in the (d) (tetrahedral) sites, 16 Fe^{3+} in the [a] (octahedral) sites, and 24 rare-earth ions Y^{3+} in the {c} (dodecahedral) site (see Figure 2.14). The yttrium and iron ions are surrounded by close-packed O^{2-} ions. In the position of the dodecahedral site, the Y^{+3} ion is bonded and surrounded with eight O^{2-} ions, in the octahedral and tetrahedral sites the iron ions are bonded and surrounded with six and four O^{2-} ions respectively.

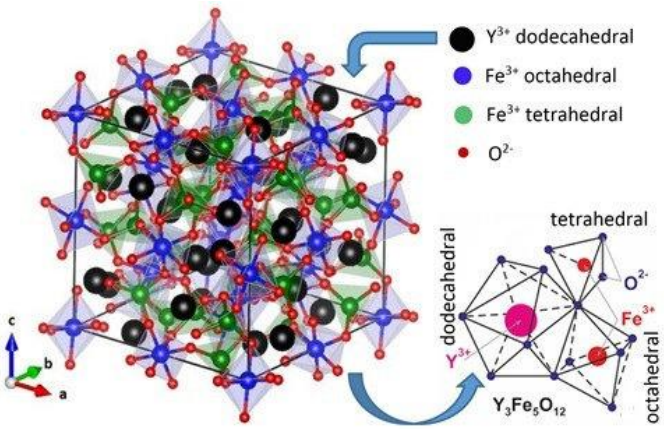

Figure 2.14: Crystal structure of YIG.

The presence of iron ions in both octahedral and tetrahedral positions creates complex superexchange interactions which have a strong effect on the optical absorption and on the MO spectra. Interactions between the rare-earth in the dodecahedral site and iron ions in the octahedral or the tetrahedral sites are much smaller, compared with the interaction between iron ions from different sites.

Optical and MO properties of YIG

The study of the YIG materials starts from the 50s, where the first optical and MO optical have been presented by Dilon [121]. The optical absorption spectrum for YIG contains the optical transparency window in the near-infrared region from 1.0 to 1.3 μm (see Figure 2.15). In the region below 5 μm a strong optical absorption is observed due to the contributions of lattice vibration phonons. In the region above 1 μm absorption due to electron transition in the octahedral site with the center of the absorption band at approximately 900 nm is observed.

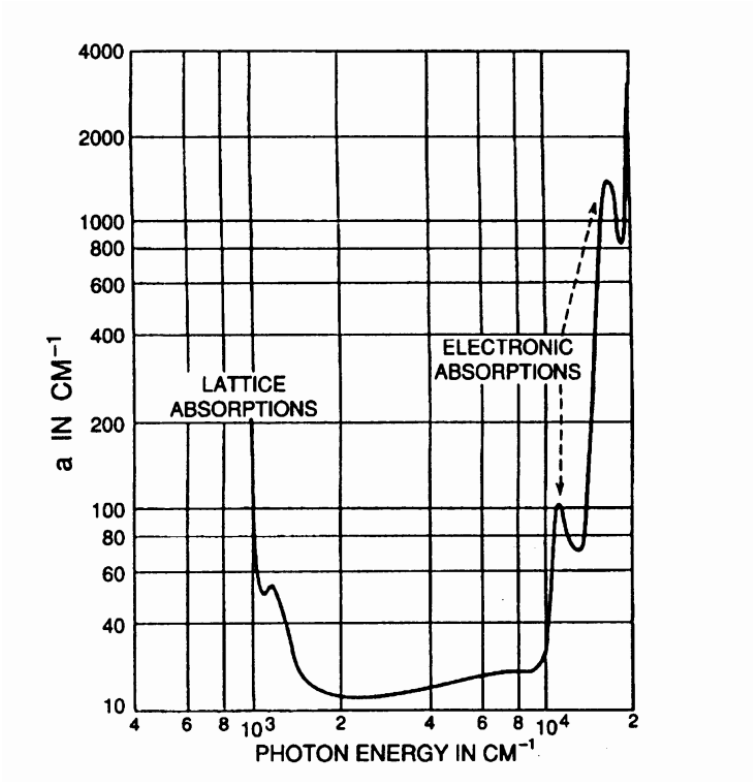

Figure 2.15: The optical absorption spectrum of YIG taken from [121].

The highest value of FR is observed in the visible region at 435 nm, and equal to $2.8 \cdot 10^4$ deg·cm^{-1}. In the ultra-violet region, the FR changes sign and reach 10^5 deg·cm^{-1} at 300 nm [122].

Doping the YIG with Bi^{3+} and Ce^{3+} ions

Due to the three different oxygen environments for the cations in the garnet structure, they easily may be substituted by specific ions with fitting radii. This feature allows a good control and manipulation of magneto-optical properties (Faraday rotation and MCD) of the materials. The cations can occupy three different sites (tetrahedral, octahedral, dodecahedral) in the garnets, which in turn extends much more the variety in materials. They exhibit different optical and magneto-optical properties, through substitutions, as the electronic states of the whole structure change and affect the resulting FR in the magnetic garnet.

According the literature [50], the iron garnet can be doped for the enhancement of FR, for instance, by bi-valent ions of Co^{2+} or tri-valent ions of Co^{3+}, which occupy tetrahedral sites, or by tetra-valent ions of Ru^{4+}, Rh^{4+}, Ir^{4+} [123] which occupy octahedral sites. The FR can also be improved by the substitution of Ce^{3+} [124], Pr^{3+}, Nd^{3+} [125], Bi^{3+}, and Pb^{2+} ions on dodecahedral sites. The Ce^{3+} and Bi^{3+} ions are the most promising for enhancing of FR in YIG.

The cerium ions in Ce doped iron garnet (Ce: YIG) exist in tri- and tetra-valent states. The optical and MO properties for both valent states are different. Gomi et al. [124] studied the optical and MO properties for $Ce_xY_{3-x}Fe_5O_{12}$ with x in the range 0 – 1.9, which were synthesized by RF sputtering on GGG substrates. The FR as a function of the concentrations of substituted Ce, Bi, Pr in YIG, measured at 663 and 1150 nm. The Ce and Bi substituted iron garnets show identical positive evolution for FR with the increasing amount of ion substitutions.

The FR studied as a function of operating temperature for Ce: YIG synthesized by PLD on the GGG substrate was studied in [126]. The temperature varied from -195 up to +25 °C at 1550 nm and at saturation of FR. Also, the FR spectrum in the range 0.25 - 2 μm at two steady-state temperatures -195 °C and 25 °C was studied. The highest value of FR of $8{\cdot}10^3$ deg·cm^{-1} obtained at -200 °C and of $3{\cdot}10^3$ deg·cm^{-1} at 25 °C at 1550 nm. In the FR spectral range, the heist value obtained at 290 nm and it is equal $6{\cdot}10^4$ deg·cm^{-1}, which is almost the same for -200 °C and 25 °C.

The main and unique difference between Ce: YIG, and Bi: YIG is how easy it is to prepare the materials with the right valency cation in the dodecahedral site. In the case of Ce: YIG the tri-valent Ce^{3+}, since the tetra-valence Ce^{4+} also may exist in the material. The right valency can be achieved by special conditions during the annealing process, for instance, annealing under pure argon atmosphere or other inert gasses, while for Bi: YIG, annealing under normal conditions is more than enough. This makes Bi: YIG very attractive for use in our project.

The great performance of MO properties as FR and FE for Bi: YIG as a function of amount of substituted bismuth ions shown in [127] in the visible range 330-550 nm (see Figure 2.16). The samples were prepared by LPE method. With small variation of bismuth from x = 0 up to x = 0.5 the value of FR increased by factor 20 at peak 375 nm. The almost the same behavior observed in FE. The FR of $20{\cdot}10^4$ deg·cm^{-1} at 375 nm with x = 0.5 for $Bi_xY_{3-x}Fe_5O_{12}$ have been measured.

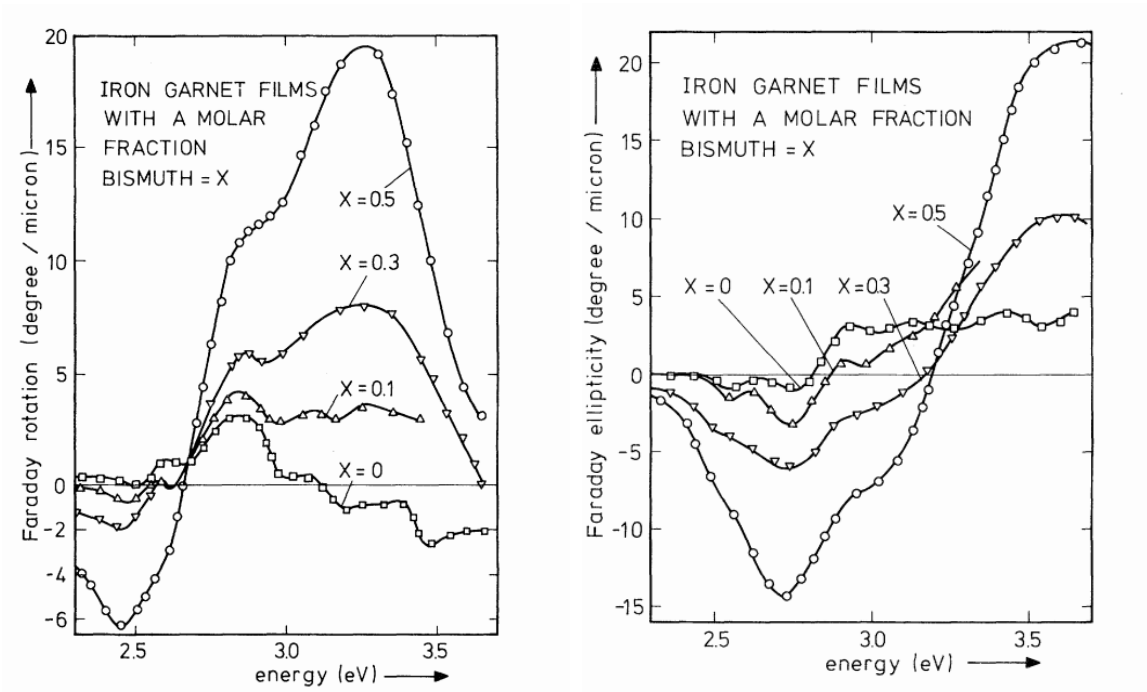

Figure 2.16: (a) The FR and FE spetrum for different concentrations of bismuth in Bi: YIG films in the 450 – 550 nm range taken from [127].

The dependence of FR on the concentration of doped Bi in different iron garnets are shown in Figure 2.17 (a). The substitution of Bi in $Bi_xY_{3-x}Fe_5O_{12}$ and in $Gd_{3-x}Bi_xFe_5O_{12}$ shows almost the same effect on FR, with increasing amounts of substituted Bi ions. The highest value of FR was achieved for the composition $Bi_{2.,3}(Y)_{0.7}Fe_5O_{12}$ with a value of $4.8{\cdot}10^4$ deg·cm^{-1} at 633 nm and at 295 K.

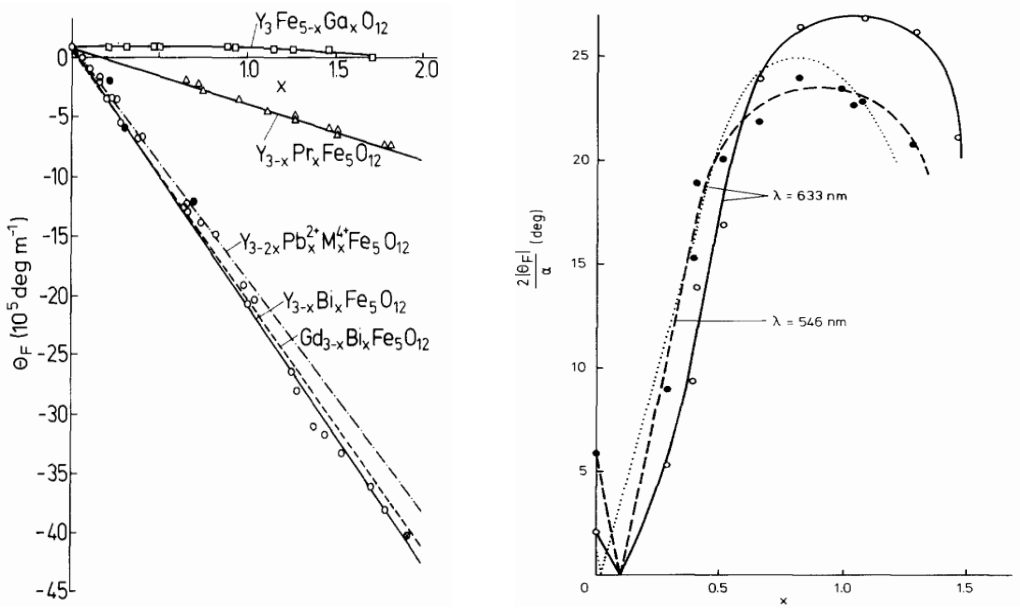

a. b.

Figure 2.17: (a) The concentration dependences of the FR for films: $Y_3Fe_{5-x}Ga_xO_{12}$, $Y_{3-x}Bi_xFe_5O_{12}$, $Y_{3-x}Pr_xFe_5O_{12}$, $Gd_{3-x}Bi_xFe_5O_{12}$, $Y_{3-2x}Pb^{2+}{}_x M^{4+}{}_xFe_5O_{12}$ (b) The concentration dependences of figure of merit $\frac{2|\theta_F|}{\alpha}$ $Y_{3-x}Bi_xFe_5O_{12}$ (solid and dash line) and $Gd_{3-x}Bi_xFe_5O_{12}$ (dot line) at 546 and 633 nm taken from [128 - 130].

The figure of merit $\frac{2|\theta_F|}{\alpha}$ for $Bi_xY_{3-x}Fe_5O_{12}$(solid and dash line) and $Gd_{3-x}Bi_xFe_5O_{12}$ (dot line) measured at 546 and 633 nm and are shown in Figure 2.17 (b). Beyond the value $x \approx 1$, a saturation of FR with increasing amounts of bismuth inside the garnet was observed. The authors connect this phenomenon with increases in optical absorption by ion substitution. Matsumoto et al. [131] have been explained this phenomenon by the role of side reactions in garnet synthesis. In this case, the value of saturation can vary depending on many parameters, starting from the initial reagents being used, going to the annealing temperature and ending with the preparation method.

Bismuth has been chosen as the specific ion to substitute the yttrium in the dodecahedral site for our project. The optical absorption of Bi^{3+} substituted garnets looks very similar to pure YIG, while FR in the visible range is enhanced. Therefore, Bi: YIG material seems very attractive for optical applications and especially the one we are interested in, where a high amplitude of FR and a small optical absorption coefficient are required.

After finding that Bi^{3+} substituted garnets are among the most effective magnetic materials with a number of positive magneto-optical properties, it remains to be defined which method of preparation is the most optimal and suitable for us. For the last 40 years, many promising techniques for garnet synthesis have been developed. In the next section, the preferred methods of Bi: YIG preparation will be presented and compared and we will highlight some specific examples.

2.5.1 Bi: YIG film preparation processes

Different processes are available for the preparation of Bi: YIG. In this section we will briefly described those frequently appearing in the literature, focusing on the preparation of thin films which is our main interest in the present work. The different processes we consider are: LPE (Liquid Phase Epitaxy [132, 133], PLD (Pulsed Laser Deposition) [134, 135], RF sputtering [136 - 138], sol-gel [2, 131], MOD (Metal-organic decomposition [139 - 141], and combinations of these methods.

Liquid phase epitaxy

Liquid Phase Epitaxy (LPE) process is one of the oldest, used since the early 1960s, and certainly the most common method in the preparation of epitaxial garnet films [142]. However, with this method it is impossible to obtain a high substitution of Bi in YIG. Also, the LPE method requires the incorporation of lead and platinum, which leads to an increase in optical absorption of the material [143]. The method of LPE growth from a liquid phase (a solution or melt) of the Bi-substituted iron garnet starts with the preparation of the mixture of the garnet constituent oxides, which are heated and melted and then homogenized at 1200 °C usually over 8 hours constant. After the mixture melt is prepared, the substrate is dipped into it for a few minutes at the typical growth temperatures of 880 ~ 900 °C. After the desired thickness of growth is reached, the sample is raised from melt. Finally, the prepared film is withdrawn from the furnace and is cleaned. This method allows to epitaxial growth at lower temperatures [133].

Pulsed Laser Deposition

Pulsed laser deposition (PLD) is one of the most multi-faceted methods for preparation of thin films of different geometries and thicknesses. This method is used since 1965 and became more popular in 1987 after Dijkkamp et al. [144] used it to synthesize Y-Ba-Cu-O superconducting films. The main drawbacks of the PLD method are high costs of the equipment and the needed control of the laser ablation process (laser power, stability of focusing, target displacement…). The PLD method refers to a group of physical vapor deposition (PVD) methods. Production of films and coatings occurs by condensation on the substrate surface of products vaporized by pulsed laser radiation focused on a target material (laser ablation). The interaction of the high-energy laser pulse with the target material leads to the formation of various products: ions, neutral particles, microparticles of originating from the target material, which deposit on the substrate to form a thin film. The quality of the film depends on the trajectory of these particles and their distribution in energy depends not only on the intensity, duration, and frequency of laser pulses but also on the pressure in the working chamber.

For example, in reference [135], YIG films with thicknesses between 10 and 400 nm were prepared using a 6 ns pulse Nd: YAG laser with a 10 Hz repetition rate and maximum energy of 180 mJ/pulse at 355 nm focused on a polycrystalline YIG target. The position of the focus point on the target surface was controlled by a computer. The substrate was a quartz plate heated between 500 to 750 °C. The laser fluence was set between 3 and 9 $J \cdot cm^{-2}$ and the pressure inside the chamber was adjusted between 5 and 200 mTorr.

RF sputtering

For the RF sputtering method, energetic ions (argon and oxygen), generated by an intense electric field, bombard the target (cathode). The atoms of the target are ejected and impinge on the substrate to form a thin film. The substrate can be heated during sputtering to improve the quality of the coating. The quality of deposition depends also on the ratio of Ar/O_2 and on the pressure inside the chamber. After the deposition of the film, the sample is annealed in the oven (700 °C – 900 °C) for a few hours.

The process can be repeated many times until the required thickness is achieved [137]. For the preparation of Bi: YIG, RF sputtering allows the use of different substrates, quartz, GGG or others.

Chemical solution deposition

The chemical solution deposition (CSD) method, including the sol-gel method [2, 131] and the metal-organic decomposition (MOD) method [139 - 141] are among the most convenient processes for the synthesis of garnets. Indeed, they only require coating and heating devices and can be operated in open air. Both these methods start from a solution of specific precursors that react to form the final material. The difference between these processes is roughly that for the sol-gel process, the precursors undergo a primary hydrolysis followed by a condensation while for the MOD, the precursors do not undergo significant condensation during the preparation of the solution or the formation of the material. We focus on the optimization of the MOD process which has been used for the preparation of the materials used in present work.

The basic process consists in simply dissolving the metal-organic compounds in an adapted solvent and to combine the solutions to obtain the desired stoichiometry. The solution is then deposited on the substrate (spin-coating, spray-coating, dip-coating…). The film is then dried and undergoes a first pyrolysis that decomposes and volatilizes the organic moieties. The next step is the annealing leading to the crystallized material. The synthesis of a well-defined material requires the adjustment of the following parameters: initial formulation, pyrolysis and annealing conditions. Nevertheless, these parameters are easy to control and give the desirable flexibility.

The next chapter is dedicated to the MO characterization of Bi: YIG films prepared by the MOD method. The dependence for FR on the annealing temperature, the duration of the annealing, and the amount of substituted bismuth ions will be analyzed and discussed. Additionally, an original technique for the calculating the rate of the chemical reaction and the activation energy of the crystallization of Bi: YIG from the MO measurements will be described. Also, in the next chapter the structural characterization through XRD and SEM analyses for Bi: YIG films and powders will be given..

Chapter 3

In this chapter, we will present the preparation of Bi: YIG thin films on silica substrates using the MOD process. As this material is dedicated to MO measurements, we have optimized the preparation considering the maximum FR achievable. For this purpose, we have monitored the evolution of the FR during the annealing process using a dedicated MO measurement setup. Section 3.1 will present this part of the work and the results obtained. In Section 3.2, we will present the structural characteristics of Bi: YIG thin films and powders made by scanning electron microscopy (SEM) and X-ray diffraction (XRD) techniques.

The parameters, on which the value of FR depends have been studied: the annealing duration time, the temperature of annealing, and the concentration of Bi in the composition of Bi: YIG. For the first time, we have calculated the rate of chemical crystallization of Bi: YIG and its activation energy from the thin film FR measurements.

3.1. Film preparation and Magneto – Optical characterization

3.1.1. Bi: YIG film preparation by metal-organic decomposition method

3.1.2. Experimental setup

3.1.3. Calculation of the MO response of the material

3.1.4. Result and discussion of MO measurements.

3.1.5. FR dependence on annealing temperature and duration

3.1.6. Multilayer films

3.1. Film preparation and Magneto–Optical characterization

3.1.1. Bi: YIG film preparation by metal-organic decomposition method

Our aim was to synthesize Bi: YIG sensing materials directly on the core of an optical fiber made of silica, without using additional epitaxial materials. For this purpose, MOD appears as the simplest process allowing the direct coating of the fiber with the initial solution of precursors and the in situ annealing.

Before considering the fiber functionalization, a preliminary task is the optimization of the MOD process to achieve the best FR performances. Despite the fact that the synthesis of Bi: YIG garnet and its MO properties are well described in the literature, this task is required for the understanding of the chemical reactions involved during crystal synthesis from the original precursors (metal propionates) and to insure that the maximum efficiency will be reached. Figure 3.1 shows schematically the different steps of the MOD process used to obtain the Bi: YIG thin films on silica substrates. All operations are performed in open air.

1st step: The process starts with the preparation of solution mixing the different metal propionate precursors dissolved in propionic acid: iron(III) propionate ($Fe(C_3H_5O_2)_3$) - υ[Fe] = 1 mol/L, yttrium(III) propionate ($Y(C_3H_5O_2)_3$) - υ[Y] = 0.279 mol/L, and bismuth(III) propionate ($Bi(C_3H_5O_2)_3$) - υ[Bi] = 0.84 mol/L. The initial products are produced by acid-base reaction [145]. They are dissolved in propionic acid according to the desired stoichiometries. As the bismuth substitution is the key parameter for the MO properties, different solutions are prepared with varying initial amounts of bismuth, x_{ini}, and of yttrium, 3-x_{ini}, but with a constant amount of iron. The metal chelates can be concentrated in the liquid solution by evaporating the solvent. Here the control of the final concentration is very important as crystallization is starts for υ[metal] > 1 mol/L. Six solutions of $Bi_xY_{x-3}Fe_5O_{12}$ were prepared with values of x_{ini} varying between 0.8 to 2.2; their formulations are detailed in Table 3.1. The concentration of the metal chelates was set to υ [Metal] = 0.9 mol/L, to avoid crystallisation and to insure a constant thickness for different formulations deposited under the same conditions.

$Bi_xY_{3-x}Fe_5O_{12}$	Mass Y (g)	Mass Y (g)	υ (mol/L)	υ after drying (mol/L)
x_{ini} = 0.8	4.73	0.656	0.572	0.89
x_{ini} = 1.0	4.3	0.82	0.59	0.9
x_{ini} = 1.3	2.905	1.067	0.688	0.91
x_{ini} = 1.6	2.393	1.313	0.716	0.9
x_{ini} = 1.9	2.366	1.6	0.689	0.9
x_{ini} = 2.2	1.72	1.805	0.735	0.92

Table 3: Composition of the initial solutions.

2nd step: The next step is a spin coating of the solution on a cleaned 1 cm × 1 cm silica substrate. The typical parameters for the spin coating are 3000 rpm for 1 minute to obtain wet films with a thickness around 500 nm.

3rd step: The films are dried and then heated up to 300 °C for 40 minutes to complete the evaporation of the solvent and to start the pyrolysis in order to eliminate the organic part. After these operations, the thickness of the material decreased to around 50 nm.

The 2nd and 3rd steps can be repeated to increase the final thickness of the films.

4th step: The final annealing, leading to the crystallisation of Bi: YIG is performed at a temperature between 640 – 750 °C and for duration varying between 4 h and 20 h.

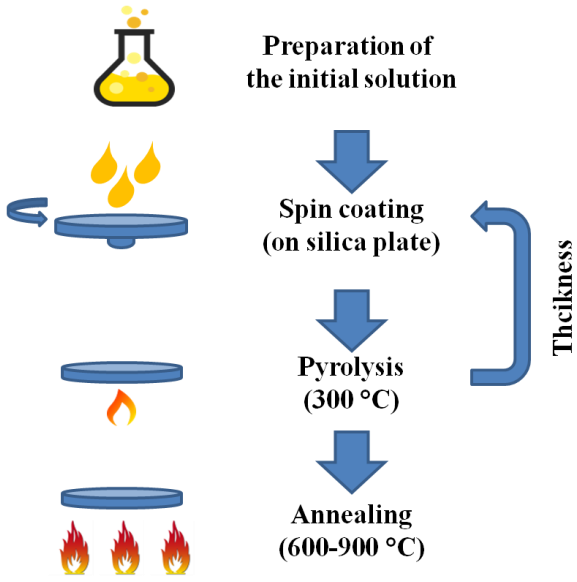

Figure 3.1: Schematic diagram of thin films preparation by MOD process.

As the optimization of the process aims to maximize the MO properties, we need to measure the evolution of FR as a function of the different parameters: formulation, annealing temperature and annealing time. For this purpose, we have performed the annealing in a small oven directly inserted in a MO measurement setup that will be fully described in the next part. This procedure enables the monitoring of the evolution of the MO properties during the annealing step without moving the sample. This avoids errors due to successive repositioning of the sample.

3.1.2. Experimental setup

To investigate MO properties of the films, the FR and FE angles were measured by ellipsometry on an experimental setup (see Figure 3.2) developed at the Institut de Physique and Chimie des Matériaux de Strasbourg. This setup allows the measurement of MO response in the 300 to 800 nm spectral range using a 150 W Xe arc lamp as the light source. The light is collimated and polarized by a Rochon prism. The polarization is adjusted at 45° of the major axes of the following photo-elastic modulator (PEM). The PEM (Hinds PEM- 100) modulates the polarization of the light at a frequency of 50 kHz. The light beam passes through the sample holder in a hot stage (LINKAM Scientific TS1500) with transparent windows. The temperature can be accurately controlled from the room temperature to 1500 °C with a heating rate ranging from 1 to 200 °C/min. The small size of the hot plate allows its positioning in the air gap of the electromagnet (GMW Associates 5403) providing static magnetic fields from -1.2 T to 1.2 T. The polarization of the light is then analyzed by a second Rochon prism aligned along the direction of the PEM major axis. The light is then focused on the entrance slit of a monochromator and detected as it exits by a photomultiplier. The signal is analyzed by two lock-in amplifiers (Stanford SR810), synchronized with the PEM, to retrieve the first and second harmonics of the modulated intensity. The amplifiers are interfaced with a computer ensuring the control of the different components and the calculation of FR and FE in real time via a program developed in the IGOR PRO environment.

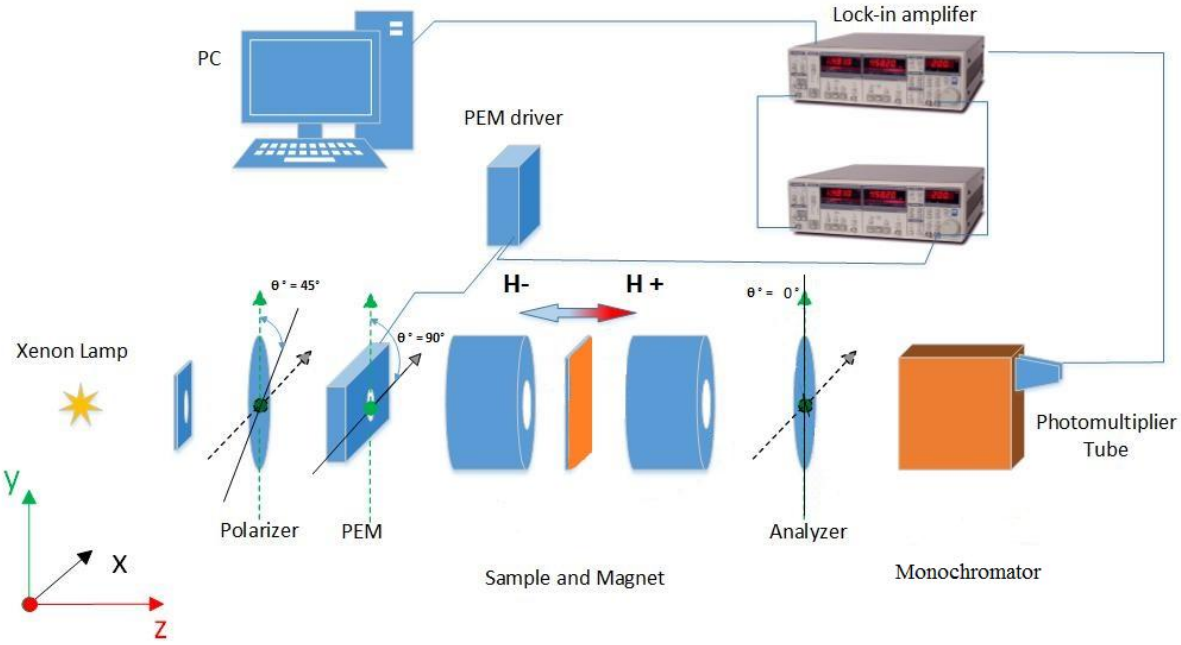

Figure 3.2: Experimental setup for the FR measurements.

The data analysis is detailed in the next part where the experimental setup is described in the Jones formalism. The same formalism will also be used later for the calculation of the MO fibered magnetic field sensor.

3.1.3. Calculation of the MO response of the material

To calculate the MO response of the sample, we need to define the polarization state of the light after all the optical elements before being measured by the detection system [146]. For this purpose, we use the Jones formalism, where the polarization of the light is represented by a vector, and linear optical elements are represented by matrices. Thus, the electric field can be written as a normalized column vector:

$$E = \begin{bmatrix} E_x(t) \\ E_y(t) \end{bmatrix} , \tag{3.1}$$

where $E_x(t)$ and $E_y(t)$ are scalar components of the electric field vector E projections on the main axis. The beam polarization state at the entrance of the photomultiplier tube (PMT) is given by the product of the matrices, corresponding to each optical element, acting on the entrance polarization state:

$$E_{PMT} = A \cdot S \cdot circ \cdot M \cdot P \cdot E = \begin{bmatrix} E_{PMT,\ x}(t) \\ E_{PMT,\ y}(t) \end{bmatrix} , \tag{3.2}$$

where P represents the initial polarizer, M the Jones matrix of the photo-elastic modulator, *circ* the transformation matrix from the linear polarization basis to the circular polarization basis, S the matrix of the sample under investigation, and A the matrix for the analyzer which is aligned along the direction of a major axis of the PEM.

The PEM matrix is M:

$$M = \begin{bmatrix} exp\left(\frac{i\varphi}{2}\right) & 0 \\ 0 & exp\left(-\frac{i\varphi}{2}\right) \end{bmatrix}, \tag{3.3}$$

where φ is phase retardation of the modulation. The *circ* matrix represents the transformation the coordinate system from rectangular to circular:

$$circ = \frac{1}{\sqrt{2}} \begin{bmatrix} 1 & i \\ 1 & -i \end{bmatrix}. \tag{3.4}$$

Passing through the Bi: YIG garnet, the right-circularly and left-circularly polarized light experience different phase shifts originating from the different refraction indexes. The matrix S represents the sample under investigation, namely the circular dichroism and the circular birefringence of the material:

$$S = \begin{bmatrix} exp\,(-i\theta_F + \eta_F) & 0 \\ 0 & exp\,(i\theta_F - \eta_F) \end{bmatrix}, \tag{3.5}$$

where $\theta_F(\omega)$ and $\eta_F\,(\omega)$ are the FR and FE angles respectively. The last optical element in the system is the analyzer, whose matrix is shown below:

$$A = \frac{1}{2} \begin{bmatrix} 1 & exp\,(-i2\delta) \\ exp\,(i2\delta) & 1 \end{bmatrix}. \tag{3.6}$$

This matrix corresponds to a linear polarizer expressed in the basis of circular polarizations. The orientation of the analyzer corresponds to $\delta=0$. The intensity of the detected beam with the PMT determined by the following equation:

$$I = E^*_{PMT,\ x} \cdot E_{PMT,\ x} + E^*_{PMT,\ y} \cdot E_{PMT,\ y}\,, \tag{3.7}$$

where the exponent * indicates complex conjugation.

Substituting these elements in to equation (3.2) leads to the expression of the Intensity at the output of the setup:

$$I = \frac{1}{2}[\cosh 2\eta_F + \sinh 2\eta_F \sin\varphi + \sin 2\theta_F \cos\varphi]\,. \tag{3.8}$$

Considering that the modulation of the dephasing introduced by the PEM is harmonic:

$$\varphi = \varphi_m \sin\omega\, t\,, \tag{3.9}$$

where φ_m is the amplitude of the dephasing, ω the circular frequency of the modulation, and t the time, one can develop the equation (3.9) in Fourier series and express the intensity of the light as the sum of a discontinuous contribution (I_{dc}), a first (I_ω) and a second harmonic ($I_{2\omega}$) contributions. These different contributions are expressed as:

$$I_{dc} = \frac{1}{2}[\cosh 2\eta_F + J_0(\varphi_m) \sin 2\theta_F\,]\,. \tag{3.10}$$

$$I_\omega = J_1(\varphi_m) \sinh 2\eta_F\,, \tag{3.11}$$

$$I_{2\omega} = J_2(\varphi_m) \sin 2\theta_F\,. \tag{3.12}$$

Here, $J_n(\varphi_m)$ are the Bessel functions, where n = 0, 1, 2. Choosing the value of φ_m to make $J_0(\varphi_m) = 0$ and considering that η_F is always small, the FE and FR angles can be expressed as:

$$\eta_F = \frac{1}{2}\operatorname{atanh}\frac{I_\omega}{2J_1(\varphi_m)I_{dc}}, \tag{3.13}$$

$$\theta_F = \frac{1}{2}\operatorname{asin}\frac{I_{2\omega}}{2J_2(\varphi_m)I_{dc}}. \tag{3.14}$$

These expressions are used by the computer program to calculate the FR and FE from the lock-in amplifier data.

3.1.4. Result and discussion of MO measurements

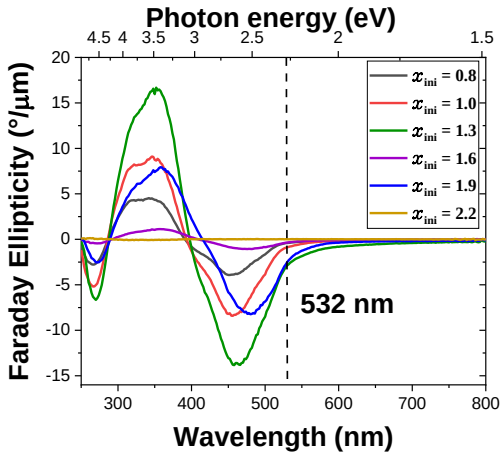

a.

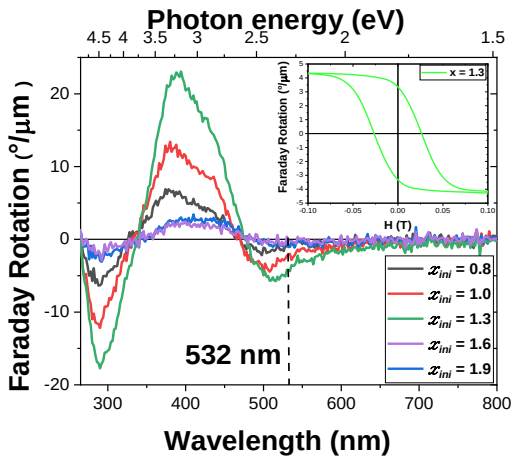

b.

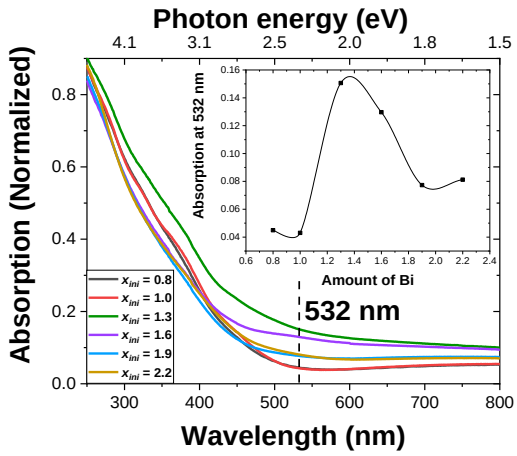

c.

Figure 3.3: (a) FE, (b) FR spectra at saturation for Bi: YIG films on silica substrate with different initial amounts of bismuth, annealed at 700 °C for 1 hour (Inset: MO hysteresis measurement at 532 nm for x_{ini} = 1.3). (c) The optical absorption for the same films. Inset: optical absorption at 532 nm (The line is a guide for the eyes).

The Faraday rotation angles θ_F for the Bi: YIG samples are measured at room temperature. In the first set of measurements, made to have a first idea about the behavior of the materials, each solution is spin-coated on a quartz substrate and annealed at a temperature T = 700 °C for 1 hour.

Figure 3.3 (a, b) presents the resulting FE and FR spectra for the range of wavelengths 250 – 800 nm. It shows a clear dependence of the FR and FE angles on the quantity of the bismuth x_{ini} in the initial solution. At saturation, these MO spectra are very similar to those observed for Bi: YIG prepared by the sintering reaction [147] and/or by MOD [148] which use different precursors. The magnitudes of the 390 nm and 516 nm peaks, ascribed to the bismuth-substituted garnet, first increase with the initial amount of bismuth and then decrease after a maximum observed for x_{ini} = 1.3. The highest values of FR at the magnetic saturation point correspond to the sample with x_{ini} = 1.3 and it is valued of 4.2 °/µm at the wavelength λ = 532 nm. This specific wavelength has been chosen as it corresponds to the second harmonic of Nd: YAG laser. Easily available, these lasers are pertinent for the development of applications and will be used for the demonstration of the MO fibered sensor. The optical absorption at 532 nm, also varying with the bismuth substitution rate, [149] shows a similar variation (see Figure 3.3 (c)).

The hysteresis cycles for the different samples are also measured at 532 nm in the range -0.5 – 0.5 T and are given in Figure 3.4. In this graph, we observe a rising of the FR angle with increasing amounts of bismuth in the initial formulation from x_{ini} = 0.8 to x_{ini} = 1.3. This can be interpreted as an increase of the effective substitution of the bismuth enhancing the coupling between the ferric ions which leads to a change in the magnetic moment and amplifies the MO response. For the value above x_{ini} = 1.3, we observe a decrease of FR. This suggests that the effective substitution of the bismuth in the final products saturates, but the apparition of by-products has also been observed.

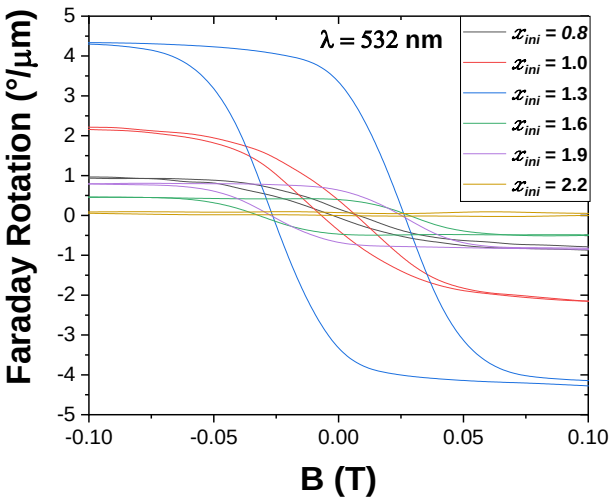

Figure 3.4: Hysteresis loops measured from the FR at 532 nm for $Bi_xY_{3-x}Fe_5O_{12}$ as a function of the amount of bismuth, x_{ini}, in the initial solution.

Many of the investigations of the Bi: YIG dependence on the annealing temperature and on the duration of the annealing have already been described in [128 - 130], and the behavior of Bi-substituted iron garnet thin films in magnetic fields is well documented. However, the preparation methods, the initial precursors, the nature of the solvents… lead to the noticeable changes in the garnet properties. Figure 3.5 shows a visual map of the FR values for the samples at a given temperature T = 620 – 720 °C. The thickness of the magnetic material is around 40 nm after a 1 hour annealing procedure. This experiment is required to choose the right range of temperatures to determine the composition with the highest value of FR. In the graph, the samples with x_{ini} = 1.3 and x_{ini} = 1 show the highest value of FR in the range of temperature 650 – 700 °C.

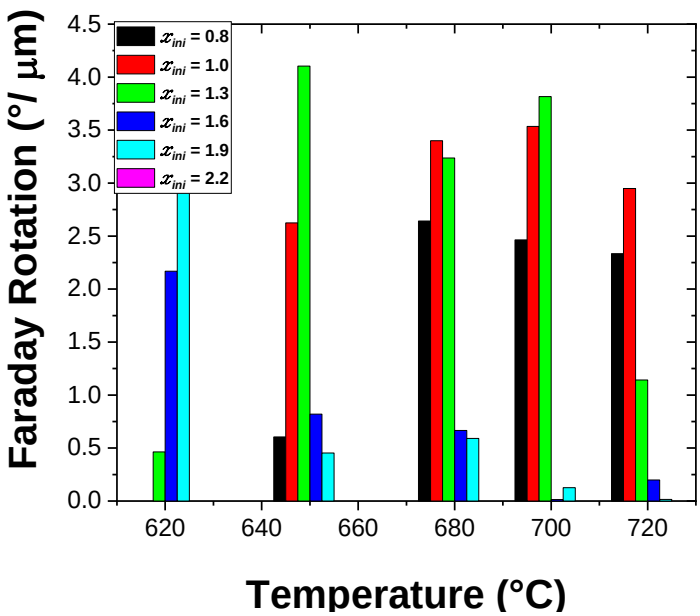

Figure 3.5: FR dependency on temperature for $0.8 < x_{ini} < 2.2$ samples (thicknesses 40 nm), annealed during 1 hour at different temperatures.

Nevertheless, it is still not possible to assert that the maximum FR is reached for any of our initial compositions, measurements considering the annealing duration is still required at this point.

3.1.5. FR dependence on annealing temperature and duration

In this part, the influence of annealing temperatures and heating durations on MO will be presented and discussed for the different initial compositions. This study definitively sets the parameters leading to the optimum FR angle and therefore defines the process that will be used for the preparation of the material used for the development of the MO fibered sensor.

Using the previous results, we prepare more samples of Bi: YIG thin films on silica substrates varying the initial concentration of bismuth in the precursor solution , x_{ini} = 0.8, 1 ,1.3, 1.6, 1.9, 2.2 (see Table 5). Here, the MO response is monitored during the annealing process thanks to the oven inserted in the experimental setup. The FR for the different films is measured at the saturation of the magnetization as a function of annealing temperature and duration for different bismuth composition x_{ini}, varying from x_{ini} = 0.8 to x_{ini} = 2.2.

Each sample is heated to the desired temperature, set between 620 and 740 °C. As these temperatures are well above the Curie point ($T_C \approx 320$ °C), the sample is brougth back to room temperature before the MO measurements. The fast cooling and heating rate (≥ 200 °C/minute) of the oven limits this measurement time to 2 – 3 minutes. We have checked that this operation has no influence on the final MO properties as the samples present the same MO response whether they underwent successive heating/cooling cycles or not. The evolution of garnet crystallization with the temperature and the duration of the annealing can be therefore accurately measured. The annealing times vary from 700 min. to 1700 min. depending on the sample composition. The FR values are taken every 10 – 20 minutes at the beginning of the annealing, for a better resolution, and every 1 – 2 hours close to saturation. These measurements are performed at 532 nm at the saturation of the magnetization (B = 0.5 T).

Before annealing, a first MO measurement clearly shows that the samples have no MO activity. As seen in Figure 3.6 the samples exhibit very different behaviors during the annealing process depending on the initial compositions and the temperatures.

The appearing of MO activity is always observed for the whole set of parameters, but the behavior differs for different temperatures and compositions. For example, for x_{ini} = 1.6 at 640 °C, it takes 800 min. to reach the saturation, but at 720 °C this value is 40 min. only. For composition x_{ini} = 1. 3, the FR saturation is reached only after more than 1600 min., but at 700 °C, the saturation appears after just 80 min.. Furthermore, at temperatures higher than 720 °C, we observe a decreasing of the FR value. The starting time of this decrease in FR is also dependent on the temperature and composition of the solution. It is clearly observed for T = 740 °C and x_{ini} = 1.0, where after 80 min of annealing time, the FR starts a decrease. For x_{ini} = 1.3 at the same temperature, this value decreases under 25 min. Finally, we observe that the maximum of FR decreases with increasing annealing temperatures.

The optimum set of parameters leading to the highest FR appears to be an initial amount of bismuth set between 1.0 and 1.3 and an 6 to 8 hours annealing at a temperature set between 640 °C and 680 °C.

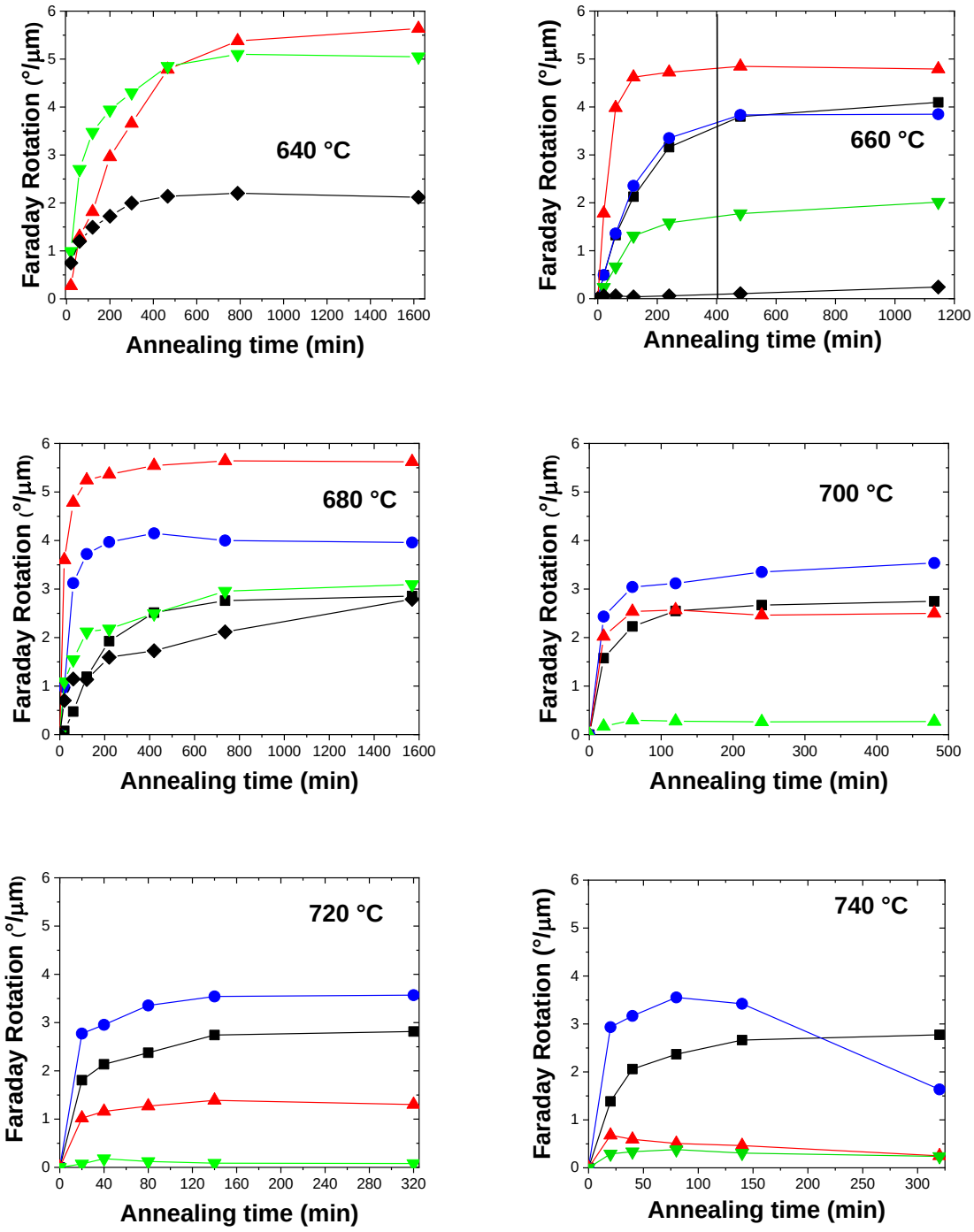

Figure 3.6: Evolution of the FR angle with the annealing time for different initial amounts of bismuth at (a) 660 °C and (b) 740 °C. Black square: x_{ini} = 0.8, Blue disk: x_{ini} = 1.0, Red up triangle: x_{ini} = 1.3, Green down triangle: x_{ini} = 1.6, Black diamond: x_{ini} = 1.9.

3.1.6. Multilayer films

In paragraph 3.1.1 we have announced that the pyrolysis deposition step can be repeated in order to increase the thickness of the sample. We present here the results obtained repeating the cycle five times. Relying on data obtained from previous measurements, where solutions with x_{ini} = 1.0 and x_{ini} = 1.3 showed the best results for MO properties, we prepare multilayer samples from the same solutions. The objective is to increase the value of FR by increasing the thicknesses of the garnet. For this purpose, we used the common scheme of film preparation (see Figure 3.1), namely, spin-coating each solution on the substrate followed by a pyrolysis at 450 °C for 30 min., and repeated it five times. Note that we were able to increase the temperature of pyrolysis as no crystallizations have been observed up to this value. The final thicknesses of the samples are close to 250 nm. They were measured by using an interferometric microscope (Zygo NewView 6300) setup.

Figure 3.7 (a) below gives the measured FR for the multilayer films. For comparison, the FR for one layer (50 nm) and for multilayer (250 nm) films made from the same solution are plotted.

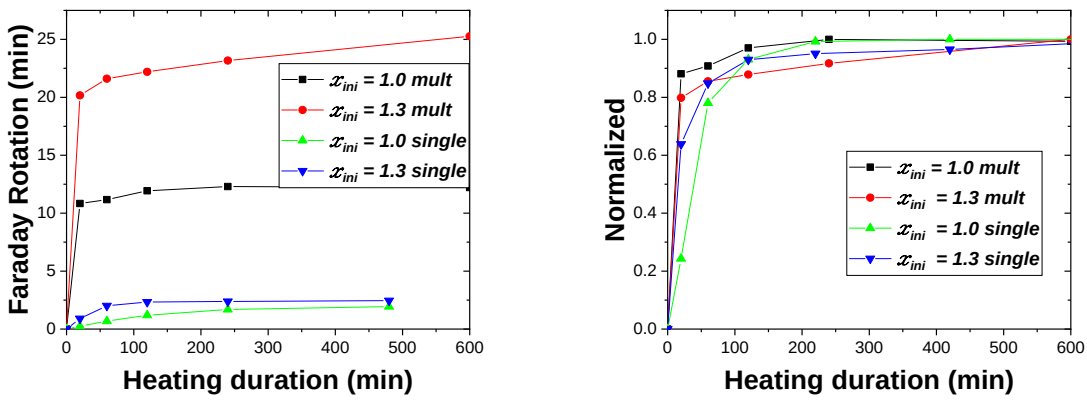

a. b.

Figure 3.7: (a) FR, (b) normalization of FR, for x_{ini} = 1.0 and x_{ini} = 1.3 with different film thicknesses 50 and 250 nm.

Figure 3.7 (b) presents the normalized data of Figure 3.7 (a). The slopes of the FR curves given in Figure 3.7 (b) for each initial composition do not change with increasing thickness, meaning that the thicknesses do not influence to rate of chemical reaction even at 250 nm. These results clearly show that the materials prepared with an initial amount of bismuth of x_{ini} = 1.3 exhibits better performance. This initial amount will be used for the preparation of the material for the sensing device.

These multilayer films will be also used for XRD measurements. Since a minimum thickness of 100 – 200 nm is required for XRD characterization.

3.2. Crystallization process of the Bi: YIG

3.2.1. The XRD analyses of Bi: YIG films

3.2.2. SEM and AFM measurements of Bi: YIG films

3.2.3. XRD and SEM measurements of Bi: YIG powders

3.2.4. DTA measurements for Bi: YIG powders

3.2.5. Activation energy of Bi: YIG film crystallization

3.2. Crystallization process of the Bi: YIG

The previous work set the parameters leading to the maximum FR values of the garnets prepared through the MOD process. Up to now, we have no idea about the effective composition of the final material and about the evolution of the crystallization process. In this part, we present the structural characterization of the materials and calorimetric measurements that shed some light on the chemical reactions taking place in the process. The objective is to understand why the MO response saturates at an initial amount of bismuth around 1.3 instead of increasing linearly until the full substitution is reached. Finally, we present a method to measure the activation energy of the crystallization of the garnet films based on the MO measurements. Here we circumvent the failure of the calorimetric methods due to the presence of the substrate.

3.2.1. The XRD analyses of Bi: YIG films

The XRD patterns (Brucker D8 Advance) of the Bi: YIG for x_{ini} = 1, 1.3, 1.6, 1.9 garnet on silica samples, annealed at 660°C are presented in Figure 3.8. As we increase the initial amount of bismuth the garnet (g) [4 2 0] peak corresponding to $Bi_xY_{3-x}Fe_5O_{12}$ increases and shifts. It is related respectively to an increase of the crystalline phase quantity and to the change of garnet lattice parameter. This is confirmed by variations of the large bump underlying the different spectra between 10°< 2Θ < 60° related to an amorphous phase.

As x_{ini} increases, we observe a decrease of the amorphous part but also the appearance of secondary phases identified as yttrium orthoferrite ($YFeO_3$), iron oxide (Fe_2O_3) or bismuth ferrite ($BiFeO_3$). At the highest bismuth concentration used, x_{ini} = 2.2, the amount of Bi: YIG dramatically drops and only the [4 2 0] peak can be observed on the XRD pattern while all the other peaks are related to side products.

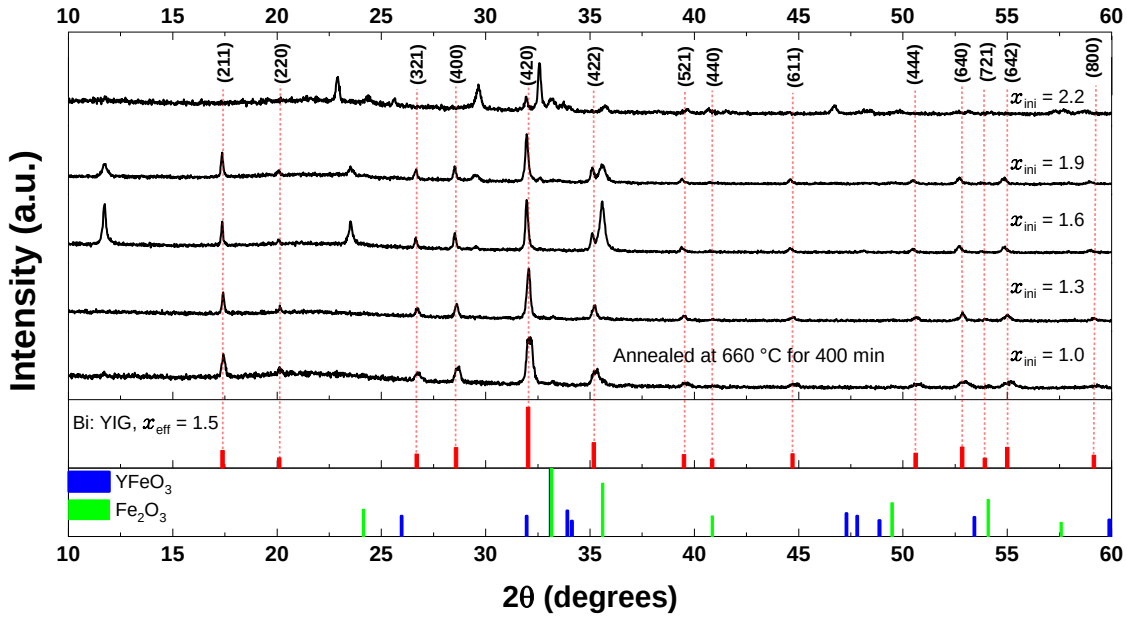

Figure 3.8: XRD patterns of the Bi: YIG films annealed at 660 °C during 400 min for different initial amounts of bismuth: x_{ini} = 1.0, 1.3, 1.6, 1.9, 2.2. At the bottom, the histograms give the tabulated positions and relative intensities of the diffraction peaks for Bi: YIG, $YFeO_3$ and Fe_2O_3.

The XRD spectra presented Figure 3.8 show no sign of crystallized oxides of the individual components (Bi_2O_3, Fe_2O_3, Y_2O_3). This suggests that, after the pyrolysis of the initial solution, these oxides remain in an amorphous state before the reaction leaves them available for the garnet synthesis. These measurements confirm that the reaction scheme strongly depends on the initial composition. Indeed, the increase of the initial amount of bismuth not only favors the garnet phase, but also triggers competing side reactions [131, 139]. Here, the measurements reveal the presence of $YFeO_3$ and Fe_2O_3 for $x_{ini} > 1.3$. The presence of side products is also evidenced by the diffraction line at 11.73° and 23.51°, but they could not be definitively assigned to any known phases. In the XRD spectrum corresponding to the composition $x_{ini} = 1.3$, the peaks corresponding to secondary phases or to the by-products are not observed and only those corresponding to the Bi: YIG appear. This means, that the initial reactants mainly participate in the formation of the Bi: YIG phase.

The calculation of the lattice parameters of the Bi: YIG from the XRD spectra shows a very linear positive evolution from $x_{ini} = 1$ until $x_{ini} = 1.3$, where the saturation is reached (see. Table 6 and Figure 3.9).

Sample	Lattice parameter, A	lattice parameter through Vegard's law.
x_{ini} = 1.0	12.456	12.456
x_{ini} = 1.3	12.48	12.48
x_{ini} = 1.6	12.51	12.505
x_{ini} = 1.9	12.516	12.53
x_{ini} = 2.2	12.52	12.554

Table 4:Lattice parameter for Bi: YIG with x_{ini} from 1.0 to 2.2.

This evolution and the poor efficiency of the garnet synthesis for high initial bismuth concentrations raise the problem of the effective substitution rate, x_{eff}, in the final product. This rate can be evaluated from the lattice parameter considering a simple linear law (Vegard Law) for the different x_{ini} values (see Table 6) [135, 150, 151]. As a result, the effective substitution appears to be equal to the amount of bismuth present in the initial solution for the low concentrations (see Figure 3.9) and clearly saturates for values above 1.6 in agreement with previous observations [131, 150].

Considering these results, we propose that the saturation of the MO properties of the Bi: YIG prepared by MOD process results mainly from a saturation of x_{eff} at 1.6. However, as the saturation of the FR is observed for x_{ini} = 1.3, we suggest that, above this point, the apparition of side products limits the concentration of Bi: YIG in the final material and lowers the MO response even if the substitution slightly increases up to 1.6 for higher x_{ini} values.

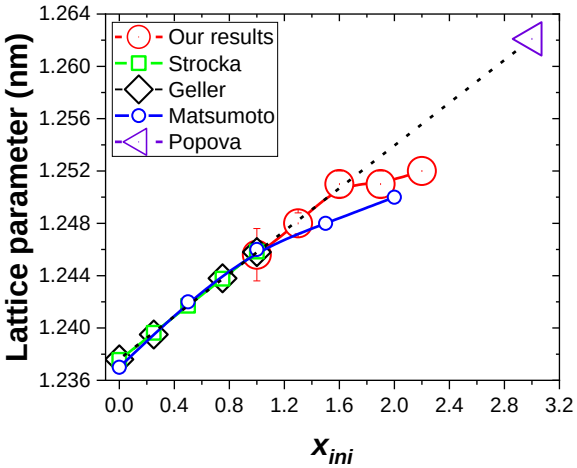

Figure 3.9: Evolution of the lattice parameter of the $Bi_xY_{3-x}Fe_5O_{12}$ with the amount of the initial part of Bi, compared with lattice parameters measured by Matsumoto et al. [131], Geller et al. [150], Strocka et al. [151] and Popova et al. [135].

3.2.2. SEM and AFM measurements of Bi: YIG films

The surface morphology observed by SEM (JEOL JSM-6700F) is shown in Figure 3.10. It can be seen from these micrographs that many cracks appear on the layer is with an average size of 2 µm to 5 µm. We observe three distinct grey levels assigned to three distinct phases: white grey can be assigned to the bismuth rich phase $BiFeO_3$, middle grey to the garnet phase Bi: YIG and dark grey to $YFeO_3$ assuming that mean atomic weights give corresponding atomic absorptions. To improve the quality of the material surface and avoid the appearance of cracks, we produced a low concentrated solution of Bi: YIG, which only affects the thicknesses of the deposited films after each spin coating procedure.

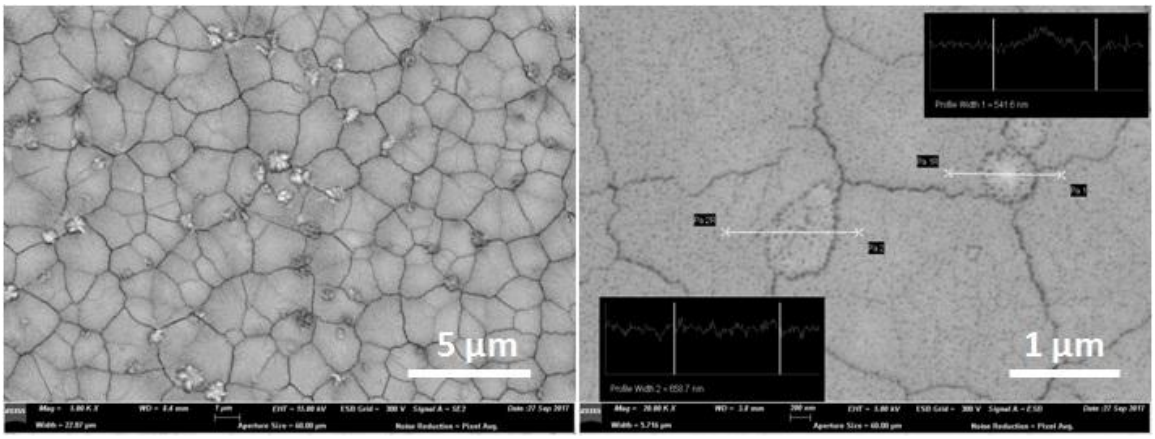

a. b.

Figure 3.10: SEM images of the Bi: YIG film with x_{ini} = 1.3 multilayer samples annealed at T = 660 °C.

In Figure 3.11 demonstrated the SEM images of multilayer garnet film in profile. The sample was prepared on a silica substrate with 5 repetitions of pyrolysis at 450 °C and annealed at 660 °C for 5 hours. The sample was cut, and the edge was polished for profile SEM measurements.

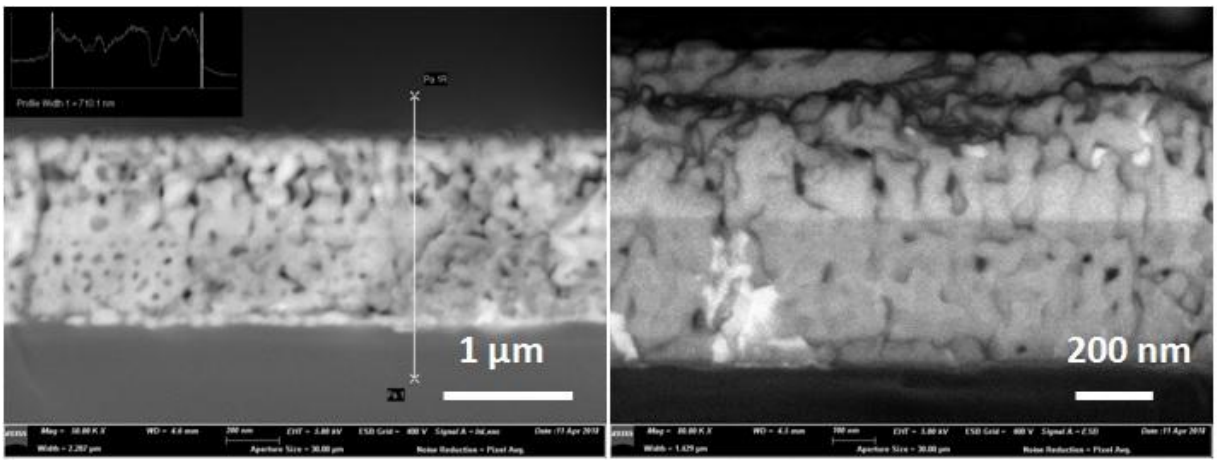

a. b.

Figure 3.11: SEM images for Bi: YIG multilayer film in profile with x_{ini} = 1.3 multilayer samples annealed at T = 660 °C.

For the first two layers, the liquid solution with x_{ini} = 1.0 was used, and for the other 3 layers, the solution with x_{ini} = 1.6 was used. Therefore, the border between the two different compositions of Bi: YIG can be easily recognized. The bismuth rich phase has a brighter color, which corresponds to x_{ini} = 1.6. Also, we observe the irregular appearance of voids in the garnet structure with a characteristic size of less than 10 nm. This can be explained by the fact that a fast heating of the sample enhances the evaporation rate of the organic part of the material in the pyrolysis step. This is may amount to boiling, where bubbles are released, but leave the solidified metal oxides behind. Reducing the rate of heating helps to avoid the appearance of such bubbles and improves the quality of the material.

The AFM measurements confirm that the surface has a granular structure and show that the size of the grains depends on sample composition. Figure 3.12 displays AFM images for samples x_{ini} = 1 and x_{ini} = 2.2 with the characteristic size of grains around 0.4 µm and 0.85 µm, respectively.

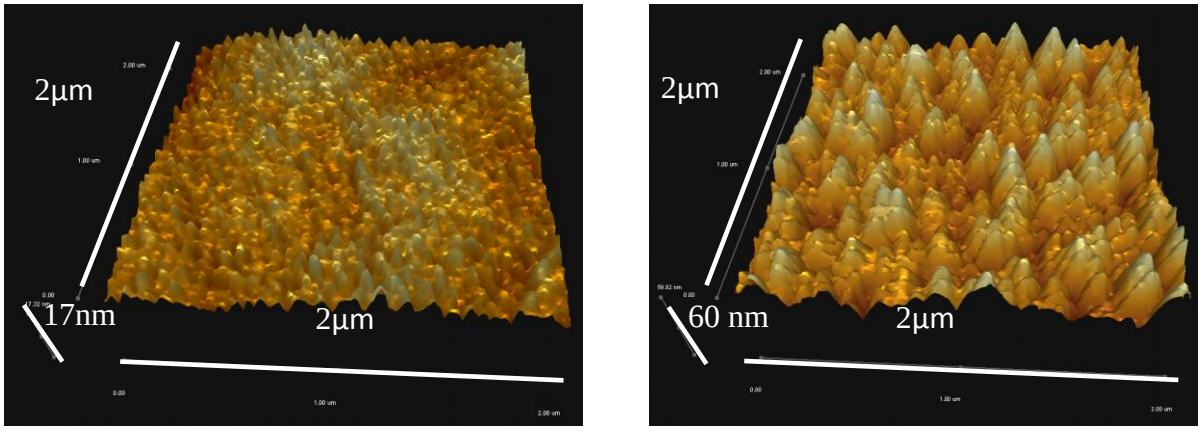

a. b.

Figure 3.12: AFM measurements for x_{ini} = 1 and x_{ini} = 2.2 of $Bi_xY_{3-x}Fe_5O_{12}$.

The characterization of the structure of the different samples shows that they clearly present inhomogeneities. These inhomogeneities induce optical diffusion and therefore losses. Nevertheless, these losses do not restrain the use of the Bi: YIG prepared by MOD as an efficient MO material, especially when considering fibered optical sensors, where the interaction region is confined to a few micrometers.

The problem of the structural dependency on the formulation and process parameters clearly deserves more attention. From our experience, the improvement of the homogeneity is possible, but requires a fine tuning of the pyrolysis and annealing processes. Unfortunately, considering the schedule of the project, we had no time to further study these aspects of the process and we were forced to postpone these investigations.

Up to now, we were focused on the characterization of Bi: YIG films, but some information concerning the preparation of the garnet can be retrieved from the Bi: YIG powder. XRD and SEM give some information on the material that can be compared with those obtained for the film, but the most interesting results are those obtained for the differential thermal analysis (DTA). These measurements are not available in the case of the film as the silica substrate is involved. In the case of powder, they give additional information on the chemical process and refine the vision of the chemical reactions involved in the MOD process.

3.2.3. XRD and SEM measurements of Bi: YIG powders

For the powder analysis, the liquid solution is just dried in the oven with a maximum heating rate of 5 °C/minute, up to a temperature of 660 °C held for 5 hours. Next, the prepared powders were used for SEM and XRD analyses.

The XRD patterns of Bi: YIG powders for x_{ini} = 0.8, 1.0, 1.3, 1.6 are taken in the range 20° < 2Θ < 70° (see Figure 3.13). These spectra show some clear discrepancies compared to the XRD patterns obtained for thin-films (see Figure 3.8). Firstly, in each pattern of the powders, we observe the garnet phases simultaneously with side products. Secondly, the appearance of these side products or extraneous phase vary with the formulation of the initial solution. For x_{ini} = 0.8 and x_{ini} = 1.0, where the amount of bismuth is relatively low, we observe the appearance of yttrium orthoferrite ($YFeO_3$) and iron oxide (Fe_2O_3). Increasing the bismuth concentration, x_{ini} = 1.3 and x_{ini} = 1.6, the amount of these side products decreases and new bismuth rich phases, as bismuth ferrites ($BiFeO_3$ and $Bi_2Fe_4O_9$), appear. The maximum amplitude for the Bi: YIG peaks are observed for x_{ini} = 1.3 and in this case, we also observe the minimum amplitude for all the side products. We interpret the difference in XRD patterns of thin-films and powders by different spatial distributions of the metal oxides after pyrolysis (450 °C). In the case where the spin-coating is used, the high surface/volume ratio insures the fast elimination of the solvent. This prevents the segregation of the different metal chelates. Consequently, after pyrolysis and during the annealing, the different amorphous oxides remain uniformly distributed. This favors the reaction leading to the Bi: YIG synthesis. In the case of liquid solutions used for the powder preparation, as the elimination of the solvent occurs progressively, the metal chelates may segregate and crystallize leading to the inhomogeneous distribution of the amorphous metal oxides. This poor homogeneity of the metal oxide then favors side reactions and the appearance of the side-products.

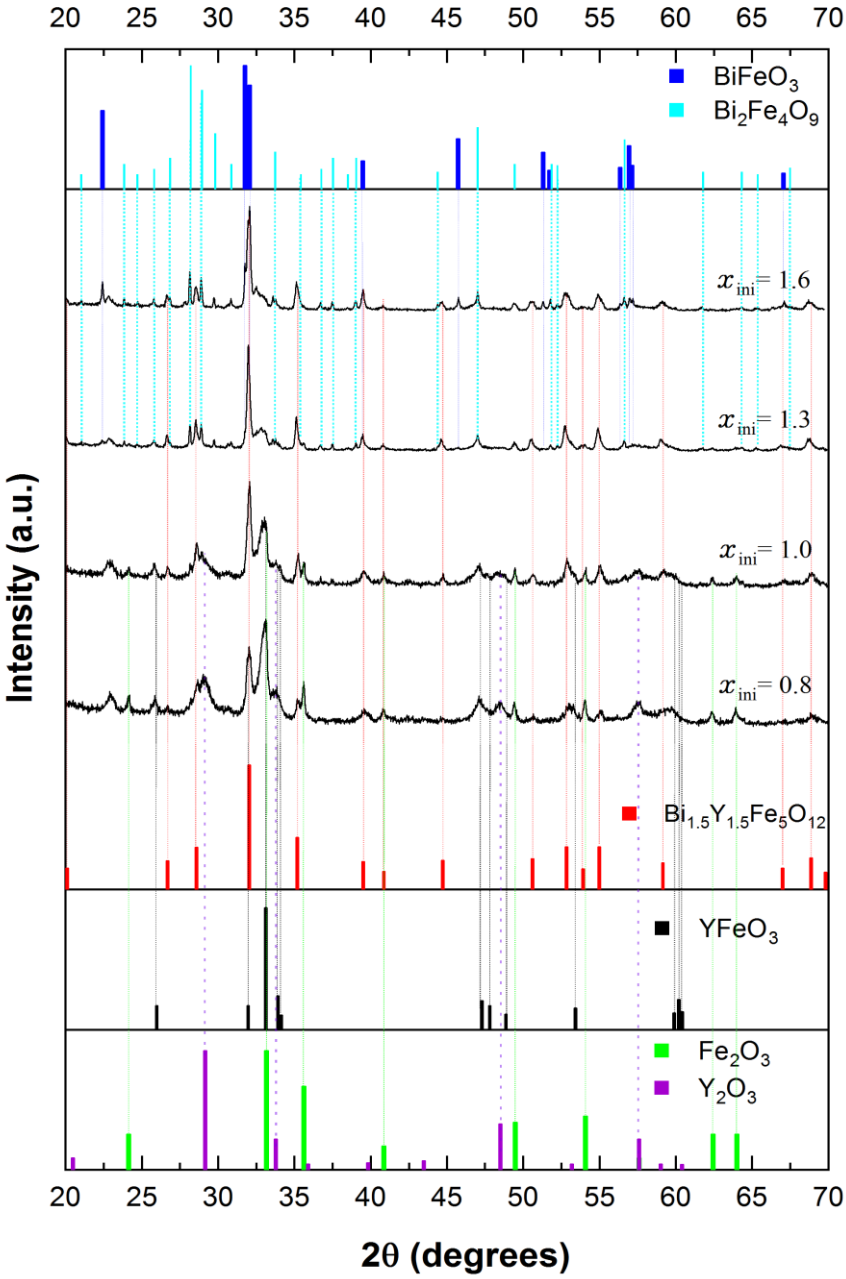

Figure 3.13: XRD patterns of the Bi: YIG powders annealed at 660 °C during 400 min for different initial amounts of bismuth: x_{ini} = 0.8, 1.0, 1.3, 1.6. At the bottom, the histograms give the tabulated positions and relative intensities of the diffraction peaks for Bi: YIG (x_{ini} = 1.5), $YFeO_3$, Y_2O_3, and Fe_2O_3. At the top, the tabulated positions and relative intensities of the diffraction peaks for $BiFeO_2$ and $Bi_2Fe_4O_9$.

The SEM images of Bi: YIG powders presented in Figure 3.14 tend to confirm this interpretation. As in Figure 3.10 corresponding to the garnet film, we observe a distribution of regions with different grey levels. Figure 3.14 (b) clearly shows that the powder is much more inhomogeneous than the films. The image shows much more and larger white grey spots, attributed to bismuth rich phases: $BiFeO_3$ and $Bi_2Fe_4O_9$. The middle grey level should correspond to the garnet phase.

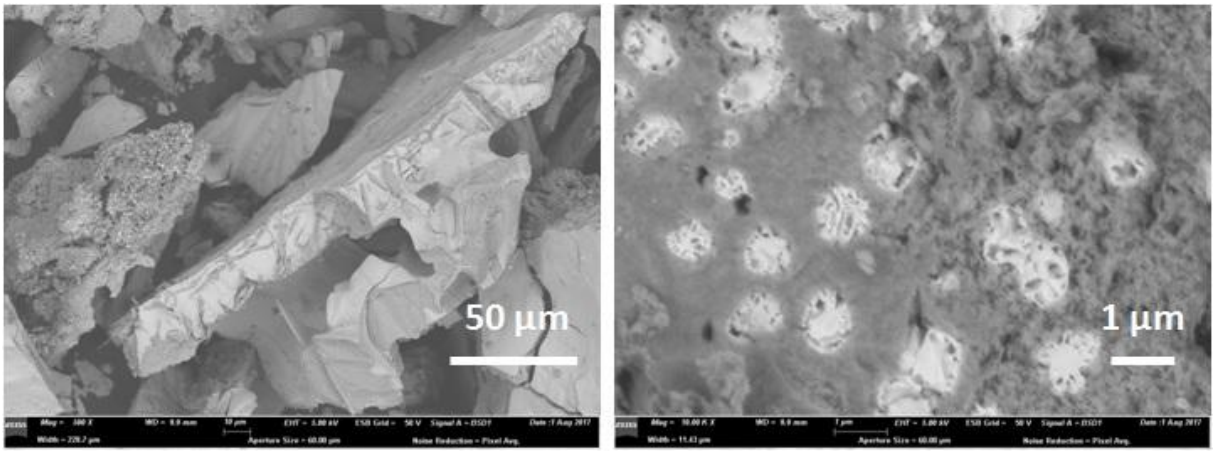

a. b.

Figure 3.14: SEM images at different scales for Bi: YIG powder prepared from a x_{ini} = 1.0 solution.

To complete these results, we perform the DTA measurements on the different compositions.

3.2.4. DTA measurements for Bi: YIG powders

Figure 3.15 shows the first derivative of the DTA (SDT Q600) curves at a heating rate of 15 °C/min for all compositions of the Bi: YIG's dried MOD powdered mixture in the range 25 °C – 800 °C. Three main exothermic peaks are observed in the temperature range 500 – 750 °C. According to the literature, the first exothermic peak, below 600 °C can be attributed to the crystallization of the $YFeO_3$ (1 a in equations 3.15) phase from the amorphous oxides. An additional reaction (1 b and 1 c in equations 3.15) can occur at low temperatures for bismuth richer compounds. The peaks between 600 °C and 700 °C (previous results clearly obtained in this range) are attributed to the Bi: YIG crystallization either directly from the amorphous oxides (2 a in equations 3.15) or involving the intermediates $YFeO_3$ (2 b in equations 3.15) or $BiFeO_3$ (2 c in equations 3.15) which have also been identified in the diffraction spectra (see Figure 3.13). Above 700 °C the decomposition of Bi: YIG dramatically accelerates (3 in equations 3.15). According the DTA and XRD results we propose tentative set of reactions for the annealing procedure:

1 a. $$Y_2O_3 + Fe_2O_3 \xrightarrow{T \approx 550\,°C} 2YFeO_3\,,$$

1 b. $$Bi_2O_3 + Fe_2O_3 \xrightarrow{T \approx 600\,°C} 2BiFeO_3\,,$$

1 c. $$Bi_2O_3 + 2Fe_2O_3 \xrightarrow{T \approx 600\,°C} Bi_2Fe_4O_9\,,$$

2 a. $$(3-x)Y_2O_3 + \frac{x}{2}Bi_2O_3 + \frac{5}{2}Fe_2O_3 \xrightarrow{600-780\,°C} Bi_xY_{3-x}Fe_5O_{12}\,, \qquad (3.15)$$

2 b. $$(3-x)YFeO_3 + \frac{x}{2}Bi_2O_3 + \frac{2+x}{2}Fe_2O_3 \xrightarrow{600-780\,°C} Bi_xY_{3-x}Fe_5O_{12}\,,$$

2 c. $$(3-x)YFeO_3 + xBiFeO_3 + Fe_2O_3 \xrightarrow{600-780\,°C} Bi_xY_{3-x}Fe_5O_{12}\,,$$

3. $$Bi_xY_{3-x}Fe_5O_{12} \xrightarrow{>700\,°C} BiFeO_3 + YFeO_3 + Fe_2O_3 + \cdots\,,$$

Also, a further reaction (3.16) may happen at high temperatures (> 750 °C) following from the sublimation of BiO from the garnet phase or other rich Bi reach phases, which induces the degradation of the material:

4. $$Bi_2O_3 \xrightarrow{T \approx 800\,°C} 2BiO + O_2\,. \tag{3.16}$$

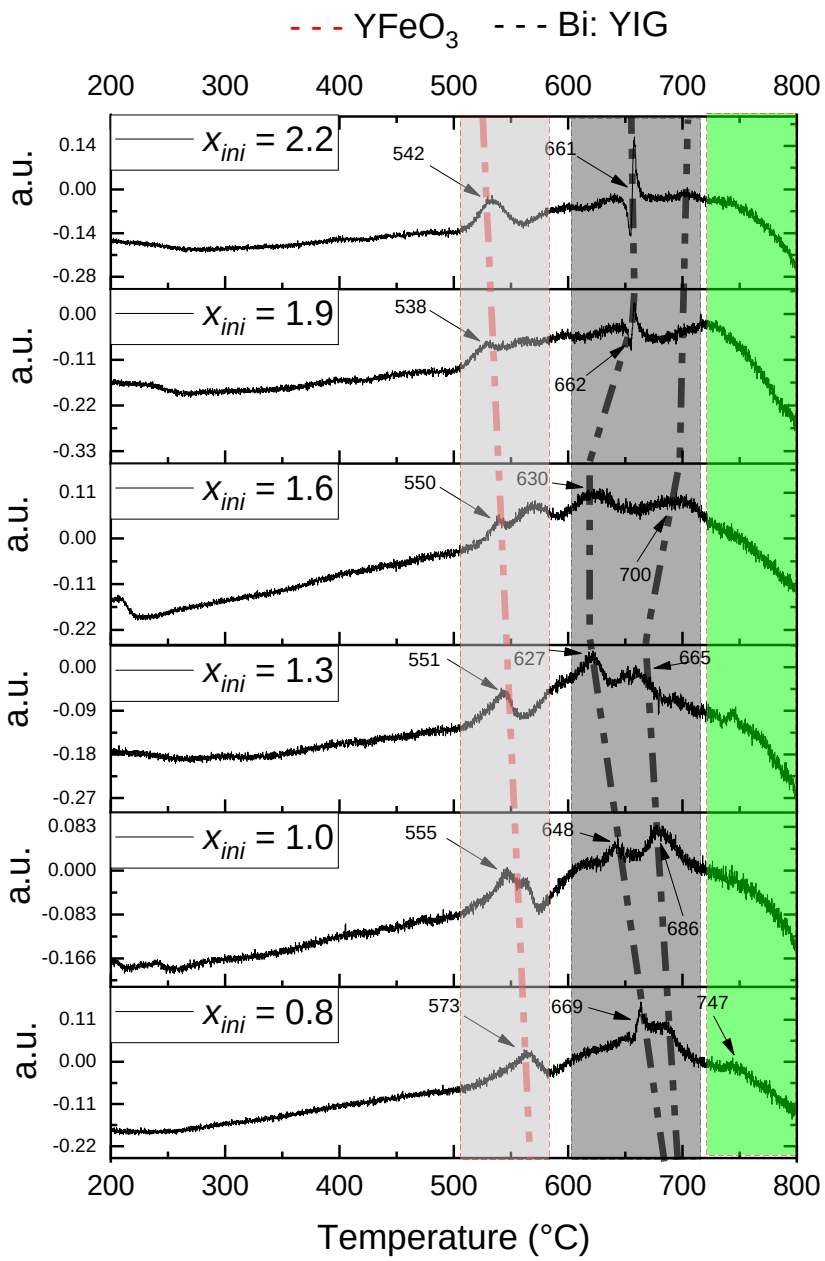

Figure 3.15: DTA for Bi: YIG powders prepared from solutions with x_{ini} = 0.8 – 2.2.

Thus, the best strategy for $Bi_xY_{3-x}Fe_5O_{12}$ garnet preparation is to try to avoid or at least to reduce the impact of the degradation by controlling the temperature and heating rate. Thus, optimal range of temperatures for garnet preparation has been found to be 640 – 700 °C.

3.2.5. Activation energy of Bi: YIG film crystallization

The measurement of the variation of the MO properties during the annealing gives us the opportunity to get access to the activation energy of the crystallization of Bi: YIG films prepared by the MOD process. This parameter is not accessible via calorimetric measurements because of the mass ratio between the 1 mm thick silica substrate and the few hundreds of nanometers thick garnet layer. The calculation of the activation energy required some simplifying hypotheses. The first one is that the MO activity fully depends on the Bi: YIG only. This consideration appears reasonable as the MO activity of all other phases identified during the preparation of the material are much lower. The second one is that all reactants can be considered as a single product. This is for sure the more drastic approximation as the crystallization reaction particularly appears as complex. Nevertheless, the calorimetric methods used for the measurements of the activation energy of crystallization are somehow using the same approximations [152, 153]. Indeed, the parameter used for the calculation of the activation energy is the variation of the temperature of the exothermic peak, attributed to the crystallization, for different heating rates in DTA measurements. No considerations are taken about the details of the reactions leading to the crystal.

In order to model our crystallization processes two parameters are required: the rate of disappearance of reactants, k_C, which lead to the formation of Bi: YIG products and the rate of destruction of Bi: YIG, k_D. These processes can be expressed with the following differential equations:

$$\begin{cases} \frac{dN_i(t)}{dt} = -k_C \cdot N_i(t) \\ \frac{dN_f(t)}{dt} = k_C \cdot N_i(t) - k_D \cdot N_f(t) \end{cases}, \tag{3.17}$$

where $N_i(t)$ is the amount of reactants for crystallization of Bi: YIG, $N_f(t)$ is the amount of Bi: YIG in the material, and k_C and k_D are the rates of chemical reaction corresponding to the formation and the destruction of Bi: YIG in the material, respectively.

The solution is given by:

$$N_f(t) = \frac{A_{const} \cdot k_C}{k_C - k_D} \cdot [e^{-k_D \cdot t} - e^{-k_C \cdot t}], \tag{3.18}$$

Where, A_{const} is a constant amplitude determined by the boundary conditions for $N_f(t)$ ($N_f(0) = 0$ and $N_f(\infty) = 0$).

Figures 3.16 below shows normalized curves of FR as a function of heating duration for different compositions of Bi: YIG from $x_{ini} = 0.8$ to $x_{ini} = 1.9$ at different steady-state temperatures in the range 640 °C – 740 °C. For each composition, the variation of the reaction rates with the annealing temperature is obtained from the adjustment of the time dependent variation of the MO response with equation (3.18).

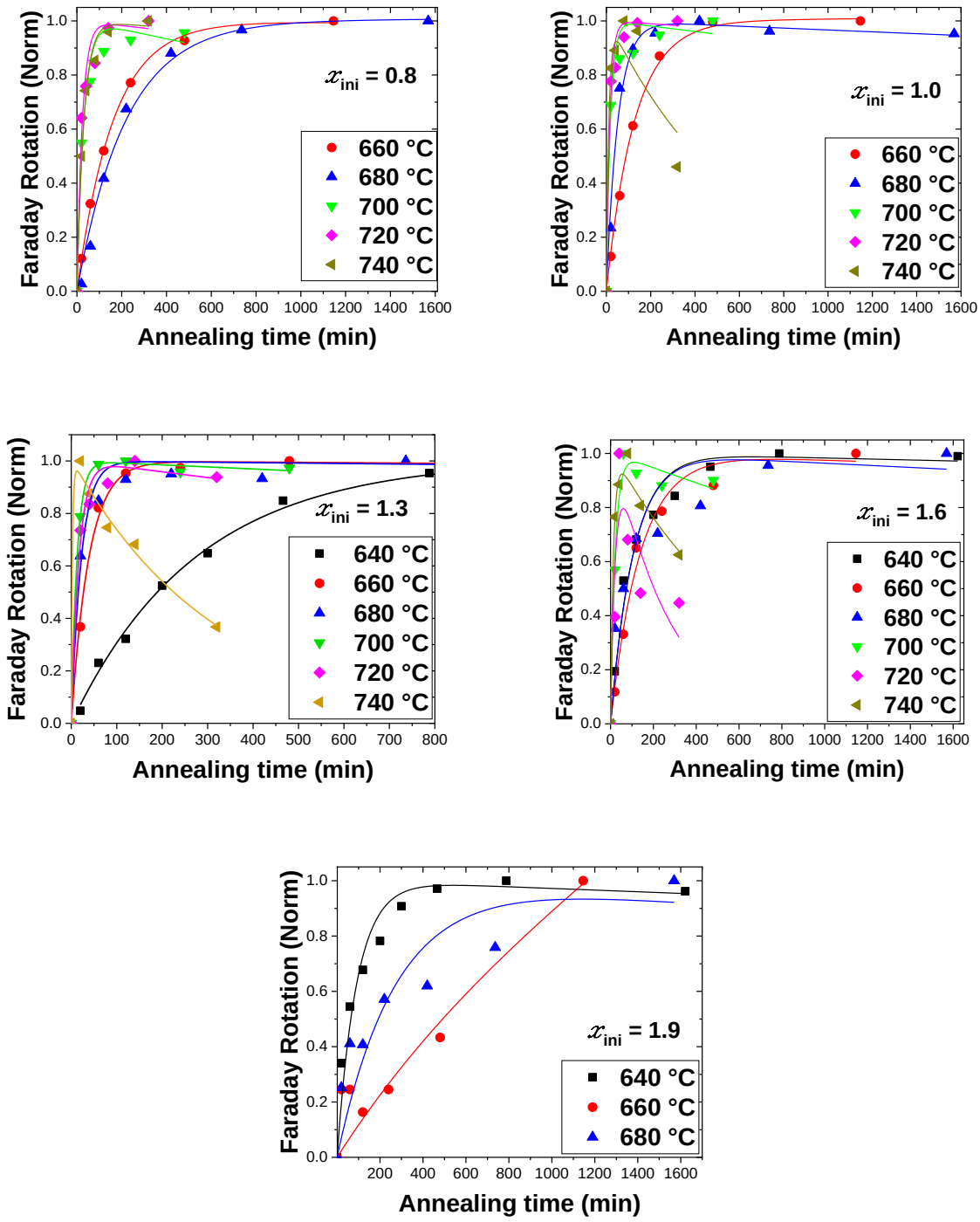

Figure 3.16: (a) Time dependent FR angle induced by the material for an initial compostions x_{ini} = 0.8, x_{ini} = 1.0, x_{ini} = 1.3, x_{ini} = 1.6, x_{ini} = 1.9 of $Bi_xY_{3-x}Fe_5O_{12}$ at different annealing temperatures. Lines are the adjustments by the solution in equation (3.18).

The calculated values for the rate of chemical reaction k_C are shown in Figure 3.17 for compositions of Bi: YIG with x_{ini} = 0.8, 1, 1.3, 1.6, at different temperatures (T = 640 °C, 660 °C, 680 °C, 700 °C, 720 °C, 740 °C).

Clearly, the rate of chemical reaction strongly depends on the annealing temperature and initial composition of the materials. Their positive evolution with temperature is quite expected, since with

increasing temperatures, the internal energy of the molecules increases, which make them more likely to react with other molecules, thus leading to faster rates of chemical reactions. Further, the annealing temperature dependence on the rates of crystallization reactions is used to estimate the activation energy of crystallization and degradation of Bi: YIG by using the Arrhenius equation (3.19):

$$k(T) = k_{const} \cdot e^{-\frac{Ea}{RT}}, \tag{3.19}$$

where, Ea is the activation energy and R = 8.314 J/mol is the ideal gas constant.

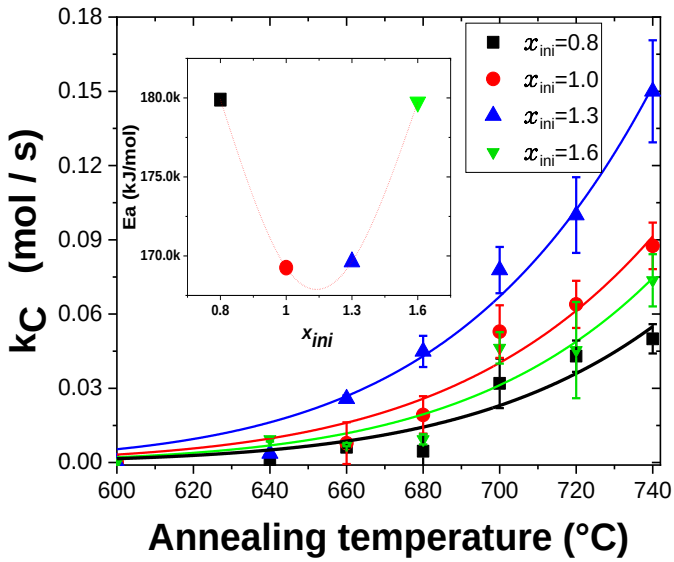

Figure 3.17: Variation with the temperature of the creation rates of MO phase for the different x_{ini}, the initial amounts of Bi. Lines are adjustments using an Arrhenius law. Inset: Activation energies of the creation of the MO phase for different initial amount of bismuth (The dashed line is a guide for the eyes).

The activation energies of crystallization are calculated using equation (3.19): Ea[x_{ini} = 0.8] = 180 kJ/mol; Ea[x_{ini} = 1] = 169.3 kJ/mol; Ea[x_{ini} = 1.3] = 169.6 kJ/mol; Ea[x_{ini} = 1.6] = 180 kJ/mol. It is noteworthy that the minimum of activation energy is obtained for the formulation leading to the materials with the best MO performances. Figure 3.18 presents the variation of the rate of destruction. The activation energies of garnet destruction deduced from these data are: Ea[x_{ini} = 0.8] = 600 kJ/ mol; Ea[x_{ini} = 1] = 700 kJ/mol; Ea[x_{ini} = 1.3] = 688 kJ/ mol; Ea[x_{ini} = 1.6] = 679 kJ/mol.

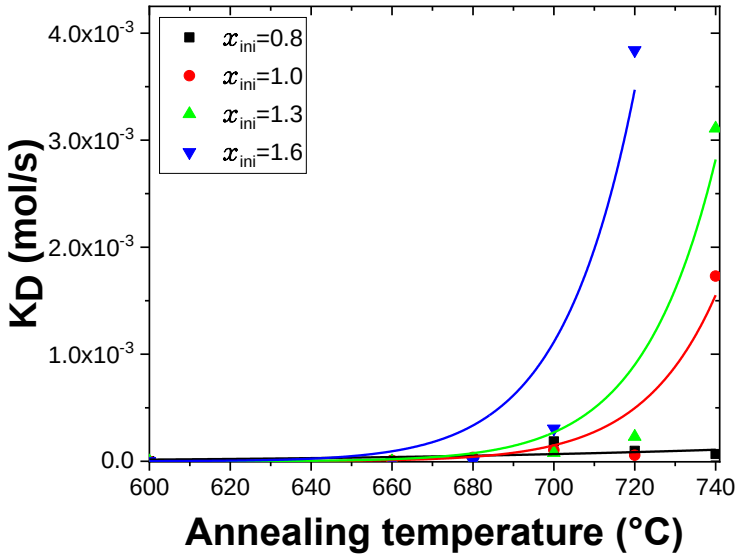

Figure 3.18: Variation with the temperature of the destruction rates of the MO phase for different initial amounts of Bi x_{ini}. Lines are adjustments by Arrhenius law.

As expected, the value of the activation energy of the garnet destruction is higher than the activation energy of the garnet crystallization. In Figure 3.18, we also observe that the destruction rate is much slower compared to the rate of crystallization, which means that the decomposition reactions spend much more energy than the crystallization.

Previous measurements of the activation energies of $Bi_{1.25}Y_{1.75}Fe_5O_{12}$ powders prepared by the coprecipitation process and measured by differential scanning calorimetry (DSC) [153] give values approximately a 4 times greater than those we have obtained. This can be explained by a better homogeneity and by the confinement of the amorphous oxides, which lower the energy of the grain barrier and therefore ease the crystallization.

The composition of Bi: YIG with x_{ini} = 1.3 has shown the best performance in MO properties. In the next chapter, we will use this composition for crystallization of Bi: YIG material at the end of an optical fiber. Also, we will present the experimental setup for magnetic field measurements, where the fiber with the garnet at the end is implemented.

Chapter 4

This chapter is dedicated to the development of the fibered MO sensor. It presents the optimization of the synthesis process of Bi: YIG in the end of optical fiber without and specific mechanical holder or alignment device, which will make its production simple and low cost. As a result, we able to prepare not only the garnet thin layers but also microcrystals with 2 – 3 μm size on the core of the optical fiber. The detection setup is detailed showing how the measurement of the magnetic field can work not only on FR but also on FE. FE based measurements enables a significant simplification of the detection and open new perspectives in magnetic field measurements.

4.1. Functionalization of an optical fiber with a garnet

4.1.1. The synthesis of Bi: YIG film at fiber end.

4.1.2. The synthesis of Bi: YIG pattern on the fiber core.

4.1. Functionalization of an optical fiber with a garnet

The principle of employing a MO sensing material along with optical fibers has been demonstrated in the previous chapter. The obvious advantages over some electrical magnetic sensors are: compact size (size of the optical fiber and the scale of sensing element), lightweight, fast response time. Nowadays, the characteristic size of the smallest known magnetic sensing element of the MO sensor [1] is around 5 mm. However, for the future devices, sizes of about 5 μm will be needed especially for medical applications involving in vivo measurements. This challenges us to refine the sensors, make them much smaller, lighter, more efficient, and, most importantly, simplify their production.

In the previous chapter, we have obtained a reliable process for the preparation of the Bi: YIG garnet with high efficiency on silica glass plates by the MOD method starting from metal solution. The material with the composition x_{ini} = 1.3 (see previous chapter) demonstrated the best performance of high FR and low optical absorption. This section is dedicated to the functionalization of the end of the optical fiber with Bi: YIG crystals using the exact same metal solution with identical composition x_{ini} = 1.3. For this purpose, we have developed an original technique, which allows us to grow the MO material on the end of the optical fiber. Just like in the case of the MOD method this technique is very simple in realization and it does not require special equipment or difficult manipulations during garnet film preparation. Two possible ways are available to synthesize the garnet on the fiber end. The first is simply to cover the end of the fiber with the initial solution and to perform the garnet synthesis process to obtain a film covering the whole surface. In this case, the size of MO film material will be limited by surface of the end, which is around 100 micrometers in diameter. The other possibility is to pattern the material to obtain a microsized garnet at the core of the fiber. This is achieved by inducing a first drying of the deposited solution by injecting light into the fiber. The exiting mode being absorbed by the solution, leads to the local heating and drying of the deposited solution. After rinsing off the uncured solution, a small amount of pre-dried material remains, centered on the fiber's core. The final micrometric garnet is obtained after a subsequent thermal treatment. In the next section, we are going to describe the functionalization processes in more detail.

4.1.1. The synthesis of Bi: YIG film at fiber end.

In Section 3.3.1. we have already described the method of preparation of liquid solution with low concentration and composition $x_{ini} = 1.3$ for $Bi_xY_{3-x}Fe_5O_{12}$. The procedure of fiber functionalization with garnet starts with the preparation of the optical fiber, specifically, the fiber-end where the solution will be deposited. Here only two things are important: the shape of the fiber-end, which has to be flat, and the state of the fiber surface, without any dust on it.

In our experiments we used two types of fiber: Single-Mode Fiber (SM 450, 488 – 633 nm, ThorLabs) and Polarization- Maintaining Fiber (PM-S405-XP, 400 - 686 nm, ThorLabs) with a cladding diameter of 125 ± 1 μm and a core diameter around of 3 μm. The cladding surrounded by plastic coating for damage protection with thicknesses of 120 ± 15 μm. For the PM fiber, type PANDA has been used, which is based on the stress rods. This stress rod has a cylindrical shape and runs parallel to the fiber core and applies some stress that creates birefringence within the core. This is needed to keep the linear polarization state of the propagated light in the fiber. This type of fiber became very popular due to its wide use in telecom application.

To start, the fiber coating is stripped with FTS4 (ThorLabs) and cleaned with the special wipes impregnated with an alcohol solvent to remove the rest of the cladding particles. Then the cleaned part of the fiber is cut with Fiber Cleaver (XL411, ThorLabs) using. As a result, we have a smooth and clean surface of the fiber end without any additional cleaning. Then, we can cover the freshly cut end of the optical fiber with the metal chelates solution. The fiber-end is dipped a few mm into the solution for a few seconds, and then it is lifted. Since the spin coating procedure cannot be used in this case, we shake the fiber-end manually a few times and let it dry at room temperature, the end facing up. As a result, we have a flat amorphous thin layer. After 5 – 10 minutes, the fiber-end is placed inside laboratory tubular oven (Carbolite MTF 10/15/130 tubular oven) at T = 450 °C for 15 – 30 minutes with the slow a heating rate of 5 – 10 °C/min. This slow increase of the temperature limits the appearance of voids in the garnet structure during the pre-annealing process (see Section 3.2.2). This step is equivalent to the pre-annealing (pyrolysis) process of the MOD method. The deposition and pre-annealing step can be repeated at will in order to increase the final thickness of the material. When the desired thickness of the garnet is reached, the fiber-end is placed once again inside the oven at T = 660 °C for 5 – 7 hours. In Section 3.1.5., these annealing parameters were chosen in order to reach the highest FR performances. In Figure 4.1 shows the scheme of the garnet film preparation.

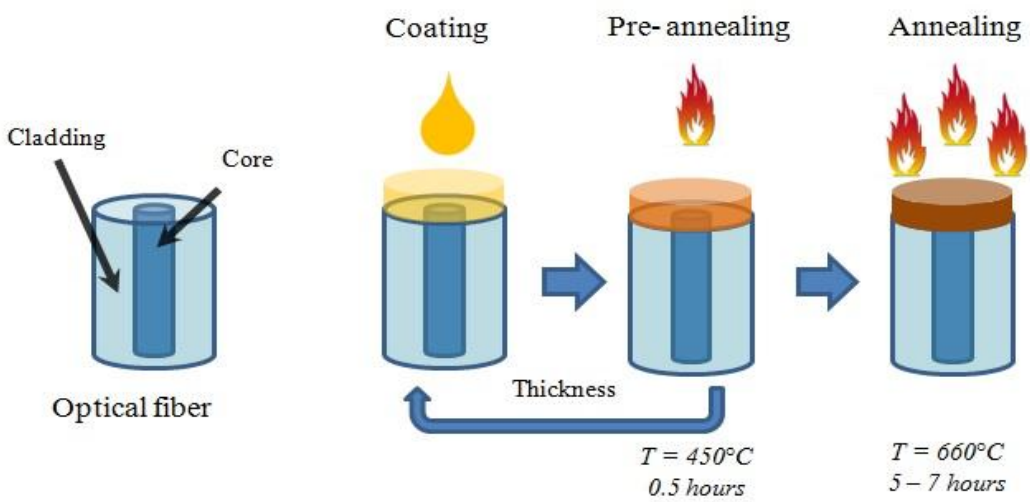

Figure 4.1: Scheme of the production the Bi: YIG film at the end the optical fiber.

In Figure 4.2 the SEM images clearly show the multilayer structure of the film at the end of the optical fiber. The structures of the first and second layer are different and can be easily distinguished. Here we just want to point out that the quality of the second layer looks much better compared to the first one, as the voids are absent and the structure looks more regular and smoother. This can be explained by the influence of the structure of the surface, where the solution is deposited. The influence of the buffer layer on the structure of the material has been studied in [154] describing bismuth iron garnet (BIG) deposited by the PLD method on GGG and silica substrates for comparison. This work showed that, the Bi: YIG material is grown easily and regularly on provided an initial buffer layer.

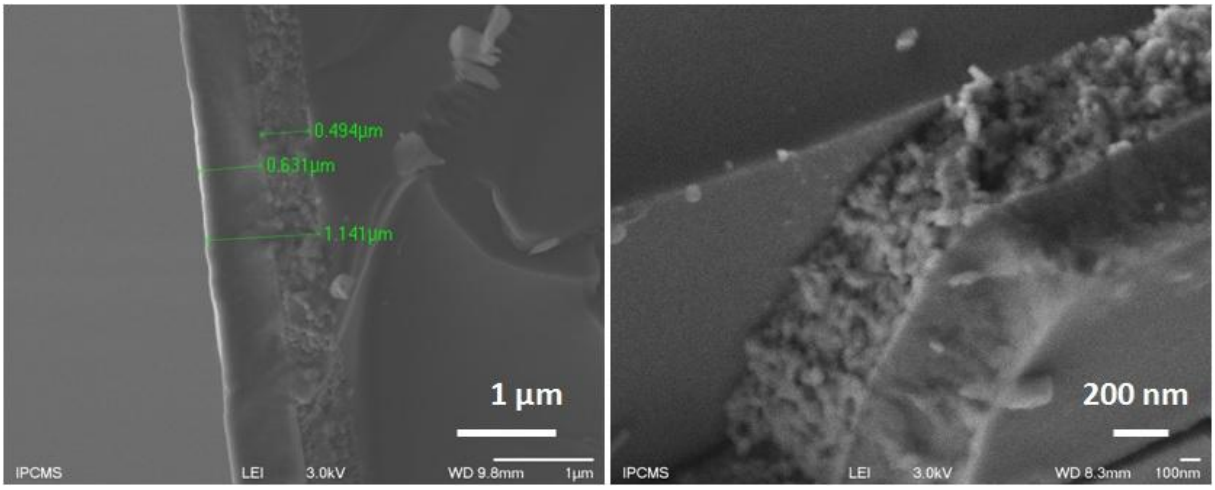

a. b.

Figure 4.2: (a) SEM images of the synthesized Bi: YIG microcrystal on the cladding surface of the optical fiber with the initial composition x_{ini} = 1.3. The deposition procedure was repeated 2 times before the annealing at 660 °C for 5 hours.

4.1.2. The synthesis of Bi: YIG pattern on the fiber core.

We can also limit the size of the garnet to the diameter of the core of the optical (2 – 3 µm) and insure that it is perfectly centered. This is achieved by injecting a light beam at the uncoated end of the fiber. At the output on the coated end, the light is absorbed and heats the liquid precursor in the region defined by the exiting light mode. The heating is controlled by the power of the laser source. The power density (≈100 kW/cm^2) of the light confined in the fiber core is high enough to achieve the evaporation of the solvent and probably to degrade the organic part in the area of the core of the fiber. Outside the exposed area, rinsing the end of the fiber in ethanol remove the uncured solution and leaves the desired garnet precursor material in the region of the core only. Then, the end of the optical fiber is placed in the oven to secure the pre-annealing procedure at T = 450 °C for 15 – 30 minutes. The thicknesses of the material limited to the core area can also be improved by repeating the processes from the beginning. Finally, the material is annealed at 660 °C during 5 – 7 hours. The scheme of Bi: YIG synthesis on the fiber core is shown in Figure 4.3. This figure, displays the interferometry images of the fiber end at each step of the preparation process. They have been taken with a Zygo NewView 6300. After these steps, we end up with a 2 µm wide and 0.2 – 10 µm thick Bi: YIG material attached to the core of the optical fiber (see Figure 4.3 (d)).

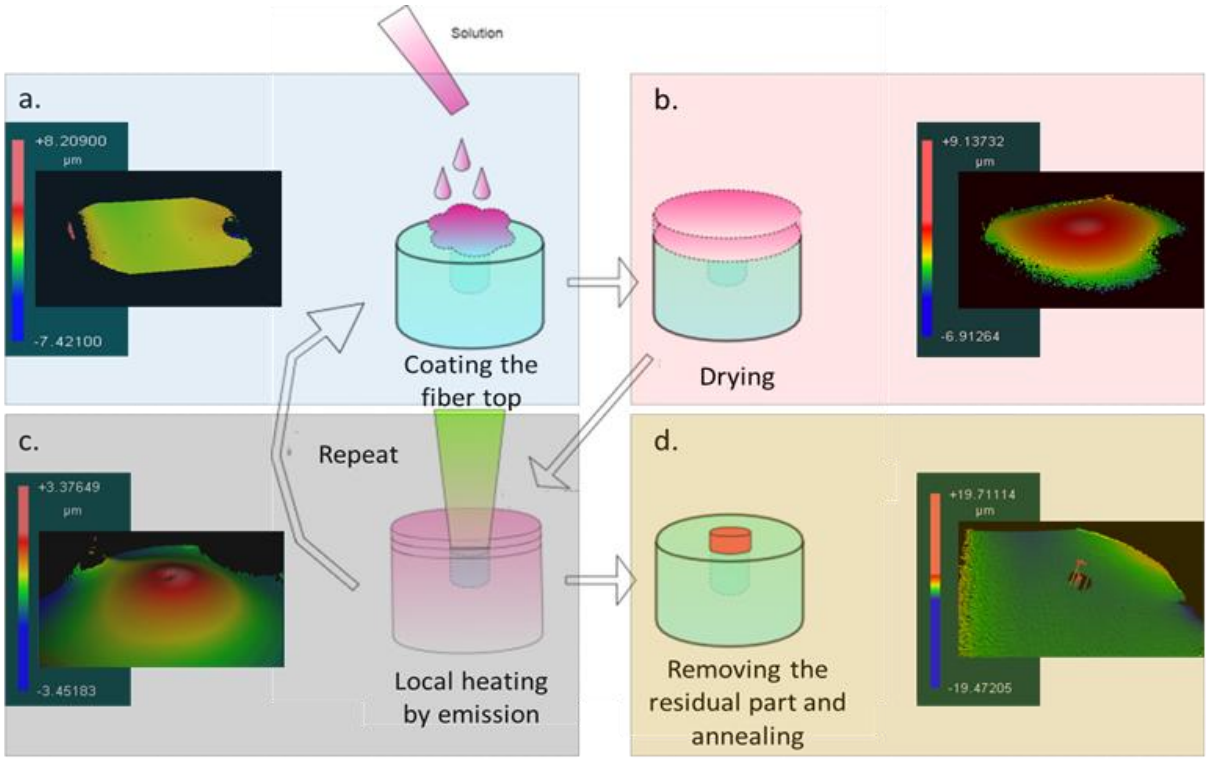

Figure 4.3: Scheme of the production of Bi: YIG on the core of the optical fiber accompanied by microscopic-interferometry measurements of the surface topography.

On Figure 4.3 (a), the topography of the fiber's end clearly shows a perfectly flat surface. After the deposition of the precursor, it is clear that the thickness of the layer is greater at the center of the fiber (see Figure 4.3 (b)). After the injection of the light, the dried part in the illuminated region shrinks (see Figure 4.3 (c)). At this stage, the viscosity of the liquid is high enough to restrain the flow and the filling of the dip due to the light induced drying. Finally, Figure 4.3 (d) shows the remaining material after rinsing the unheated solution.

The scanning electron microscopy (SEM) and microscopic-interferometry images of the Bi: YIG grown at the end of the optical fiber are displayed in Figure 4.4. In contrast to magnetic sensing fibered devices, the size of the sensitive part is strictly limited to the size of the core of the fiber. The size depends on the diamater of the fiber only. Compared to the fibered sensor based on Bi: YIG developed by H. Solhstrom et al. [1], no mechanical holder or alignment devices are required making this sensor one of the simplest and smallest possible.

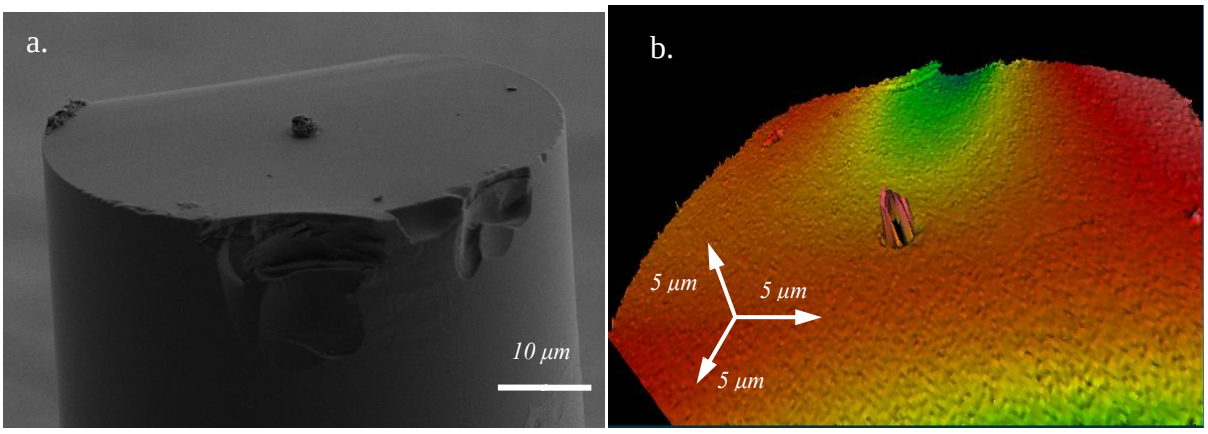

a. b.

Figure 4.4: (a) SEM image (b) Interferometric microscopy image of the Bi: YIG microcrystal on the core of optical fiber with the initial composition x_{ini} = 1.3. The deposition procedure was repeated 5 times before the annealing at 660°C for 5 – 7 hours.

The last step is the coating of the synthesized garnet at the fiber-end with a gold layer in order to improve the reflection of the light. This layer is deposited via RF sputtering (SCD 040 Balzers). The pressure inside the sputtering chamber is 0.05 mbar approximately after admitting argon gas. The fiber-end is positioned between the cathode, which is a gold target, and the anode. The fiber is flexible enough to allow to put several meters of it inside the chamber. The thickness of the gold film is controlled by the gas pressure, the distance from the target, the discharge current and the duration of the process. The SEM studies (see Figure 4.5 (a)) showed thicknesses of 50 nm for the coated gold films after 5 min of sputtering. Figure 4.5 (b) exhibits the garnet on the core of the optical fiber coated with the gold film.

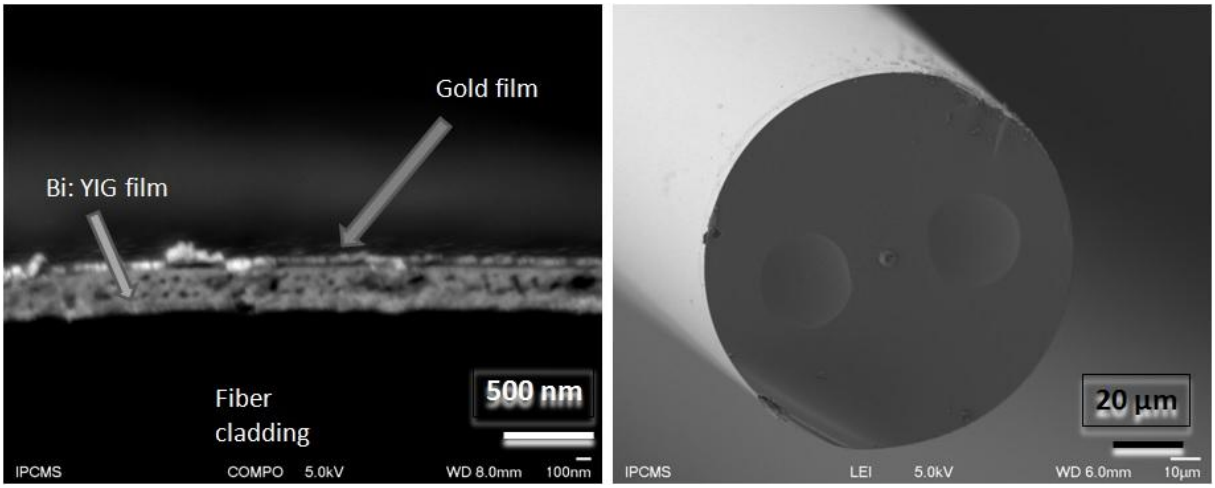

a. b.

Figure 4.5: SEM images (a) of Bi: YIG film at the edge of optical fiber coated with gold, (b) Bi: YIG microcrystal on the core of optical fiber coated with cold.

At this stage of the project, we have a potential sensor head for magnetic measurement via MO effect. The next part will present the setup developed for the interrogation of this sensor and the effective measurement of a magnetic field.

4.2 Magneto-optic sensor based on the Faraday effect

4.2.1 Magnetic field sensor device

4.2.2. Description the experimental setup through the Jones matrix formalism

4.2.3 Result of Faraday rotation and Faraday ellipticity measurements

4.2.4 Calculation of the dephasing φ

4.2 Magneto-optic sensor based on the Faraday effect

The final task of this work is to demonstrate the possibility to build a magnetic sensor using the functionalized fiber. Our main concern is here to preserve the small size of the sensor head. Indeed, in similar setups described in the literature [49], the sensing operations require additional optical elements positioned near the MO head to be able to compensate for the random and time varying birefringence of the different optical elements and especially of the optical fiber. This increases considerably the footprint of the sensor. We have developed a new solution based on the polarization modulation which avoids the use of such additional elements. Moreover, the detection scheme is able to not only on the FR, but also on the FE related to the MCD. If MCD is well described for the characterization of magnetic properties of materials, we did not found any description of its use for magnetic field measurement in the literature (journals or patents). In the next part we describe the different sensing setups and demonstrate that our devices are able to measure magnetic fields down to a few microteslas.

4.2.1. Magnetic field sensor device

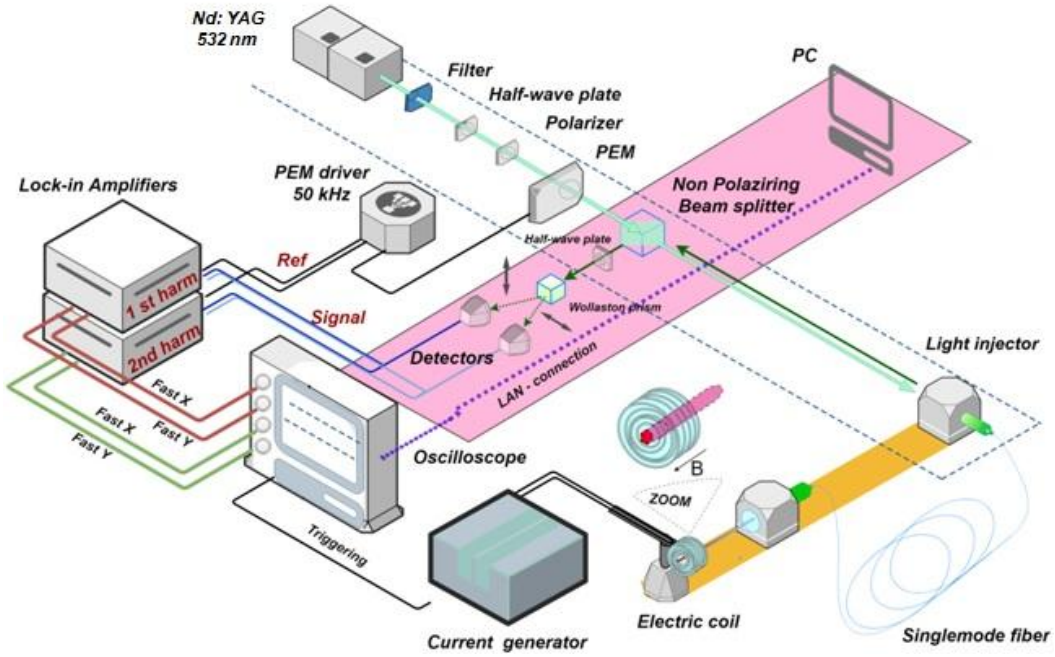

Figure 4.6: The scheme of the magnetic field sensor device.

The experimental setup (see Figure 4.6) is designed to operate with a laser source at a wavelength of 532 nm, a convenient wavelength because of the availability of commercial high-power diode pumped Nd: YAG lasers. The laser (Coherent Verdi) delivers a DC beam, linearly polarized. We use a set of neutral density filters, a half-wave plate and a polarizer to control the intensity and the polarization of the beam at the entrance of the PEM modulating the polarization of the light at a frequency of 50 kHz. The orientation of the PEM is used as the reference for the polarization orientation and the x and y directions refer to these of its major axes. Then, the beam passes through a beam splitter and is injected into the fiber that guides the light to the garnet implemented at its end. When a polarization maintaining (PM) fiber is used, the orientation of its major axis in relation with the polarization of the light has to be controlled. Here, we adjust the orientation of the fiber with an accuracy better than 0.5°. The effect of the fiber orientation on the FR measurements will be discussed in more detail in Section 4.3.3. The length of the single mode fibers used in our experiments varies from 20 cm to 5 meters. The functionalized end of the fiber is placed close to an electric coil providing the magnetic field. The orientation of the magnetic field produced by the coil is set parallel to the fiber. The coil is driven by a current generator, which allows us to produce DC or AC magnetic fields from few μT to 3 mT. The value of the field is measured via a Hall probe magnetometer (HIRST, GM08 Gaussmeter). After the garnet, the light is reflected by the gold layer, passes a second time through the garnet and propagates back in the fiber. A beam splitter positioned extracts a part of the back coming light and directs it to the detector. The measurement of the magnetic field is achieved by the analysis of the polarization of the back-reflected light using a simple polarimetric scheme composed of a half-wave plate, a Wollaston prism, and a differential detection. The half-wave plate is needed to adjust the orientation of the polarization before the Wollaston prism extraction of the two orthogonal components corresponding to the direction of the PEM axis.

The measured signals are sent to different channels (A, B) of two lock-in amplifiers (Stanford SR810). The difference between A and B is defined by the internal operation of the lock-in amplifier. The reference of the modulation frequency at 50 kHz is defined by the PEM driver. The two lock-in amplifiers detect the first and second harmonic components of the signal. The outputs from both lock-in amplifiers are sent to an oscilloscope which is connected to a personal computer.

4.2.2. Description the experimental setup through the Jones matrix formalism

To measure the MO response due to the garnet at the fiber end, we need to define the polarization state of the light after it passes all optical elements as measured by the differential detection. For this purpose, we use the Jones formalism as in the description of the MO setup measurement given in Section 3.1.2. The different elements and the corresponding Jones matrices are displayed in Figure 4.7.

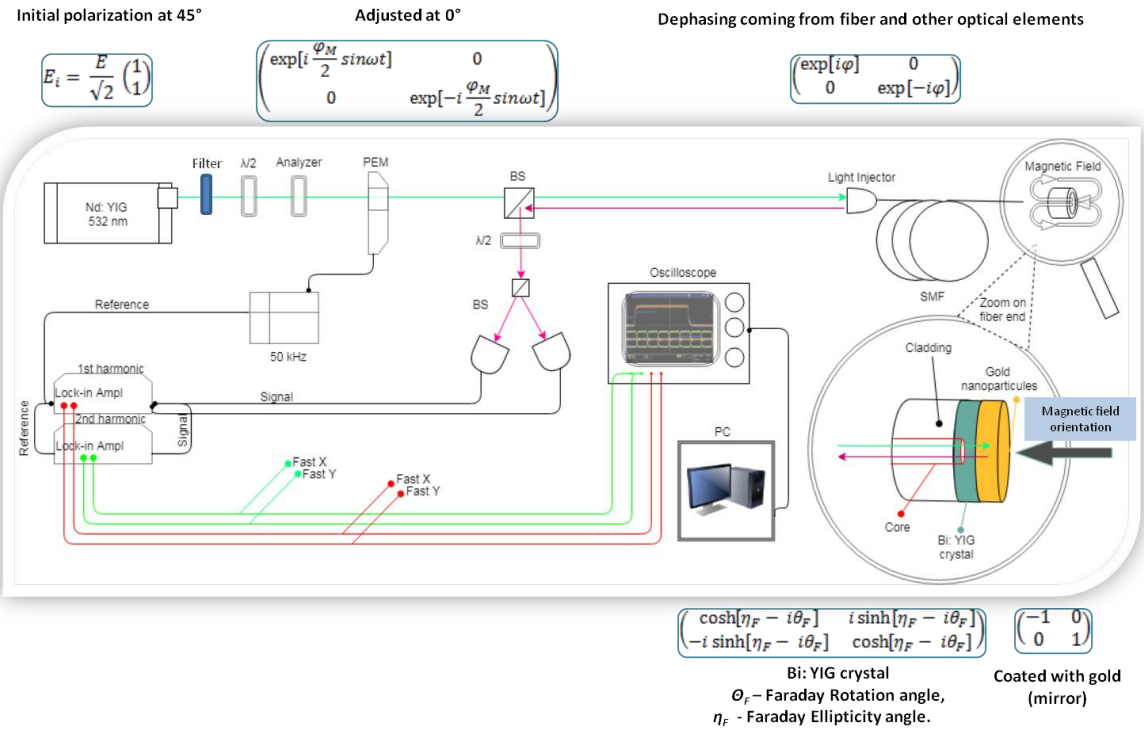

Figure 4.7: The scheme of the magnetic field sensor device with indications of the Jones matrices for each optical element in the setup. Here φ_M is the amplitude of the dephasing generated by the PEM, ω is the frequency of the modulation of the light, θ_F is the angle of the FR, η_F is the angle of the FE and φ is the dephasing coming from the optical fiber and other optical elements and related to their birefringence.

To begin, we define the Jones vector for linearly polarized light at 45° of the major axis of the PEM by:

$$E_i = \frac{E}{\sqrt{2}}\begin{pmatrix}1\\1\end{pmatrix}. \tag{4.1}$$

At the peak of activity, PEM modulator can be expressed by the matrix 4.2 introducing a symmetric phase shift on the polarization components. The phase shift is modulated at the circular frequency ω:

$$PEM = \begin{pmatrix} exp[i\frac{\varphi_M}{2}sin\omega t] & 0 \\ 0 & exp[-i\frac{\varphi_M}{2}sin\omega t] \end{pmatrix}, \tag{4.2}$$

where the φ_M is the amplitude of the dephasing generated by the PEM. The value of φ_M can be set from 0 to 5 rad. Also, our setup contains different optical elements and the fiber itself, which together

produce some change in light polarization, related to their birefringence. This change can depend on the room temperature or on the stress inside the fiber and can be expressed by:

$$B = \begin{pmatrix} \exp[i\varphi] & 0 \\ 0 & \exp[-i\varphi] \end{pmatrix}, \tag{4.3}$$

where φ is the random dephasing coming from the optical fiber and other optical elements.

The matrix representing the MO material (Bi: YIG) at the end of optical fiber can be written as:

$$G = \begin{pmatrix} \cosh[\eta_F - i\theta_F] & i\sinh[\eta_F - i\theta_F] \\ -i\sinh[\eta_F - i\theta_F] & \cosh[\eta_F - i\theta_F] \end{pmatrix}, \tag{4.4}$$

where θ_F is the angle of the FR, η_F the angle of the FE after one passage through the garnet material. At the end, once the light is transmitted through the garnet material it is reflected by the coated gold film represented by the mirror matrix:

$$M = \begin{pmatrix} -1 & 0 \\ 0 & 1 \end{pmatrix}. \tag{4.5}$$

The calculation of the final polarization state $\boldsymbol{E_f} = \begin{pmatrix} E_x \\ E_y \end{pmatrix}$ of the light before the detection is equal to the product of all matrices in reverse order:

$$\begin{pmatrix} E_x \\ E_y \end{pmatrix} = B \cdot G \cdot M \cdot G \cdot B \cdot PEM \cdot E_i \tag{4.6}$$

The polarization state of the light at the detector is given by the product of the initial vector by the resulting matrix. Then, we have to get the intensities of the signal for two projections of the polarization, which can be obtained from $\boldsymbol{E_f} \cdot \boldsymbol{E_f}^*$:

$$\begin{pmatrix} I_x \\ I_y \end{pmatrix} = \begin{pmatrix} E_x E_x^* \\ E_y E_y^* \end{pmatrix}, \tag{4.7}$$

$$I_x = \frac{E_i^2}{2}\left(cosh\, 4\eta_F + sin(\varphi + \varphi_M sin\omega t)\, sinh\, 4\eta_F + cos(\varphi + \varphi_M sin\omega t)\, sin\, 4\theta_F\right), \tag{4.8}$$

$$I_y = \frac{E_i^2}{2}\left(cosh\, 4\eta_F + sin(\varphi + \varphi_M sin\omega t)\, sinh\, 4\eta_F - cos(\varphi + \varphi_M sin\omega t)\, sin\, 4\theta_F\right). \tag{4.9}$$

In order to get a simplified expression for these equations (4.8) and (4.9), we can take the difference $I_x - I_y$, which clearly gives us dependencies on the angle of FR, the dephasing coming mainly from the fiber, and the amplitude of the dephasing generated by the PEM:

$$\Delta I = I_x - I_y = E_i^2\, cos(\varphi + \varphi_M sin\omega t)\, sin\, 4\theta_F\,. \tag{4.10}$$

After Fourier development of the expression $cos(\varphi + \varphi_M sin\omega t)$ the different harmonic components for the intensity difference ΔI can be obtained in the form:

$$cos(\varphi + \varphi_M sin\omega t) = J_0(\varphi_M)\cos(\varphi) - 2J_1(\varphi_M)\sin(\varphi)\sin(\omega t) + 2J_2(\varphi_M)\cos(\varphi)\cos(2\omega t), \tag{4.11}$$

which leads to:

$$\Delta I(0) = E_i^2 J_0(\varphi_M)\cos\varphi\ \sin 4\theta_F, \tag{4.12}$$

$$\Delta I(\omega) = -2E_i^2 J_1(\varphi_M)\, sin\, \varphi\ \ sin\, 4\theta_F\ , \tag{4.13}$$

$$\Delta I(2\omega) = 2E_i^2 J_2(\varphi_M)\, cos\, \varphi\ \ sin\, 4\theta_F\ , \tag{4.14}$$

where $J_0(\varphi_M)$,$J_1(\varphi_M)$,$J_2(\varphi_M)$ are the zero, first, and second orders of Bessel function, respectively. $\Delta I(0)$ is the difference between the intensities of the vertical and horizontal measured at $\omega = 0$, $\Delta I(\omega)$ is the difference between the intensities of the vertical and horizontal polarizations measured at ω, $\Delta I(2\omega)$ the difference between the intensities of the vertical and horizontal polarizations measured at 2ω, and E_i^2 is the DC component of the output signal.

To solve the system of the last two equations we need to take the same value for $J_1(\varphi_M)\ and\ J_2(\varphi_M)$ (see Figure 4.8). This is possible only when $\varphi_M = 0.4632$ rad:

$$\begin{gathered} J_1(\varphi_{12}) = J_2(\varphi_{12}) \\ J_1(2.5\, rad) = J_2(2.5\, rad) = 0.4623 \end{gathered} \tag{4.15}$$

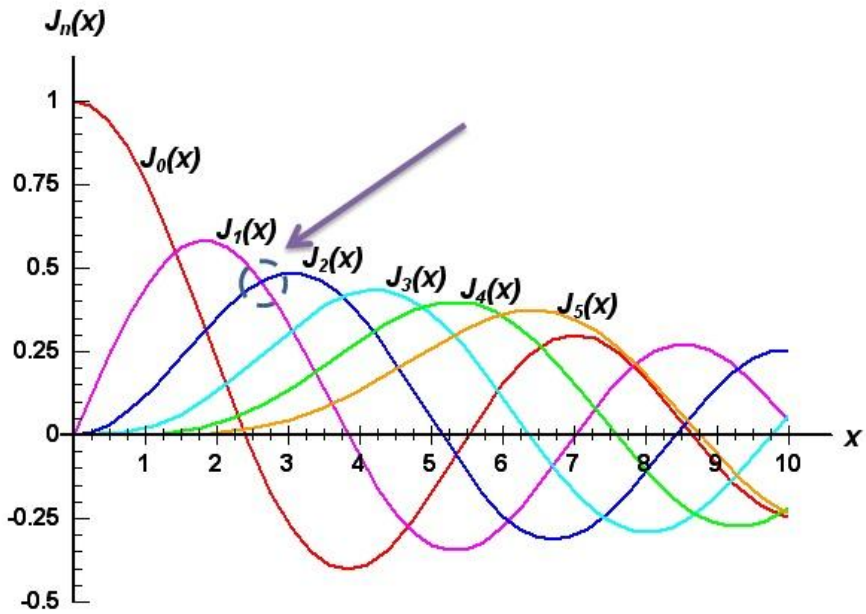

Figure 4.8: The plot of Bessel function $J_n(\varphi_M)$, where n = 1, 2, 3, 4, 5.

Solving equations (4.13) and (4.14) describing the setup leads to the following equation for the FR angle:

$$\theta_F = \frac{1}{4} asin \frac{\sqrt{\Delta I(\omega)^2 + \Delta I(2\omega)^2}}{2E_i^2 J_1(\varphi_{12})}\ . \tag{4.16}$$

Adding the two polarization intensities modulated at ω and $2\ \omega$, stemming from equations (4.8) and (4.9) respectively, leads to the determination of the FE related to the MCD. After the Fourier development of the sum of equations (4.8) and (4.9), we get the intensities for the different harmonics, which depend on the value of the FE angle:

$$I_{x+y}(\omega) = 2E_i^2 J_1(\varphi_{12})\, cos\, \varphi\ \ sinh\, 4\eta_F\ , \tag{4.17}$$

$$I_{x+y}(2\omega) = 2E_i^2 J_2(\varphi_{12}) \sin\varphi \ \sinh 4\eta_F \ . \tag{4.18}$$

Solving equations (4.17) and (4.18) we obtain the value of FE angle given by the following equation:

$$\eta_F = \frac{1}{4}\operatorname{asinh}\frac{\sqrt{I_{x+y}(\omega)^2 + I_{x+y}(2\omega)^2}}{2E_i^2 J_1(\varphi_{12})} . \tag{4.19}$$

At the output of the optical fiber, we perform the synchronous detection not only of the FR angle but also of the FE. It is important to note that these two expressions depend on sine functions (trigonometric or hyperbolic) enabling a higher sensitivity at low signal amplitudes compared to the other schemes described in the literature having a response that depends on the cosine of the FR.

It is important to note that the integration time needed for the measurement of the different value via the lock-in amplifier has to be shorter than the characteristic time of the variation of the random phase shift, but long enough to obtain a good integration of the signal modulated at 50 kHz.

4.2.3. Result of Faraday rotation and Faraday ellipticity measurements

To measure the response of the setup, we use a time varying magnetic field at applied the end of the optical fiber via the electric coil. The modulation is controlled via the current generator and set at an arbitrary chosen frequency of 23 Hz with amplitude suitable to produce magnetic fields in the range from 2 mT to 10 µT. The MO response is measured for a synthesized garnet with about 200 nm thicknesses at the end of SM optical fiber with of 0.5-meter length. It is important to note that the time constant of the lock-in amplifiers, needed for the measurement of the different parameters, has to be long enough to perform an accurate integration of the 50 kHz modulated signal and short enough compared to the characteristics time of the random phase φ variations. It is generally set below 1 ms.

The results are presented in Figure 4.9. The Fourier spectrum of FR measurements (Figure 4.9 (a)) shows a clear and narrow peaks at 23 Hz with amplitudes varying with this of the magnetic field.

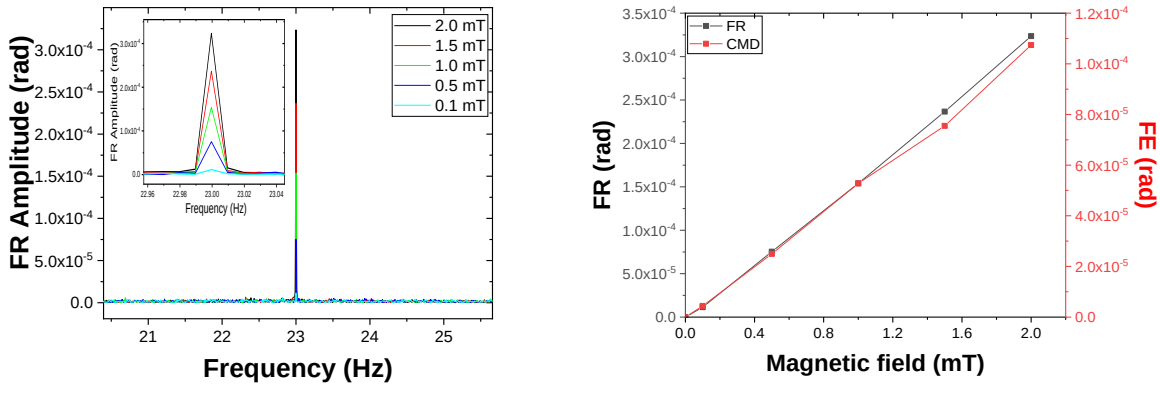

a. b.

Figure 4.9: (a) Fourier spectrum of the FR response, (b) FR and FE dependency on the amplitude of the magnetic field.

The Figure 4.9 (b) presents the FR and the FE modulation amplitudes as a function of the magnetic field. As expected, they clearly follow a linear law. The detection of 10 µT magnetic fields is here easily achieved.

In addition, we measured the MO response dependency on the magnetic field in the range from -200 mT to 200 mT amplitude range, which was generated by the DC Power Supply (FI 3030, Francaise d'instrumentation) with voltage and current parameters programmable in time. The applied magnetic field was changed in steps of 33 mT and was held constant for a minimum duration of 1 s. In Figure 4.10 the measured time dependent MO response from the fiber functionalized by garnet while the magnetic field is varied from 0 to 200 mT.

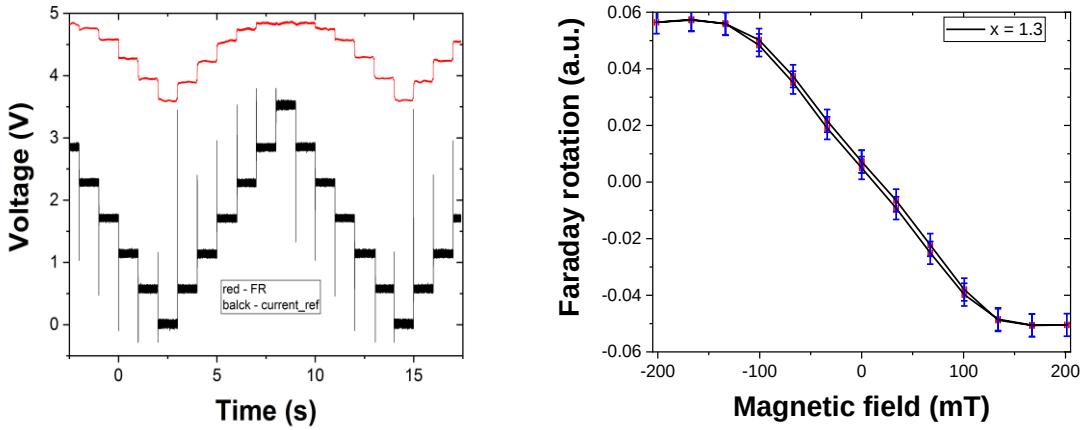

a. b.

Figure 4.10: (a) MO response (red curve) as function of time while varying the magnetic field in the range 0 to 200 mT (black curve), (b) Hysteresis loop of Bi: YIG synthesized at the end of optical fiber.

In Figure 4.10 (a), we can clearly see, that the MO response from the garnet (red curve) follows the changes in magnetic field (black curve) until 100 mT. In the range 100 – 200 mT we see the saturation of the MO response (see Figure 4.10 (b)). These results are in good agreement with the MO results obtained for the Bi: YIG films prepared on a silica substrate. This proves that the measured MO response is related to the garnet only and that the contribution of the MO properties of the fiber can be fully neglected.

4.2.4. Calculation of the dephasing φ

To confirm the validity of our measurements, we check that the variations of the amplitude of the dephasing introduced by the PEM is coherent with our results.

The ratio between the intensities of $\Delta I(2\omega)$ and $\Delta I(\omega)$ which correspond to equations (4.13) and (4.14), gives access to the value of the dephasing φ due to the birefringence the optical fiber, which can be written as:

$$\frac{\Delta I(2\omega)}{\Delta I(\omega)} = \frac{2E_i^2 J_2(\varphi_{12}) \sin\varphi \ \sinh 4\eta_F}{2E_i^2 J_1(\varphi_{12}) \cos\varphi \ \sinh 4\eta_F} = \frac{\sin\varphi}{\cos\varphi}. \tag{4.20}$$

This value is varying depending on the temperature or/and the stress inside the fiber induced by mechanical instabilities. In particular, each movement of the fiber may change the value of the phase φ. The value of φ can be then simply extracted from equations (4.20):

$$\varphi = acrtan\left(\frac{I(2\omega)}{I(\omega)}\right). \tag{4.21}$$

In Figure 4.11 (a) the measured intensities for the first and second harmonic components are given as functions of the phase-amplitude, φ_M, of the PEM. These intensities clearly change with phase φ_M corresponding to the variations of the Bessel functions $J_2(\varphi_M)$ and $J_1(\varphi_M)$, respectively. The calculated value for the dephasing φ as a ratio between the intensities of $\Delta I(2\omega)$ and $\Delta I(\omega)$ is given in Figure 4.11 (b) as a function of the phase φ_M of the PEM.

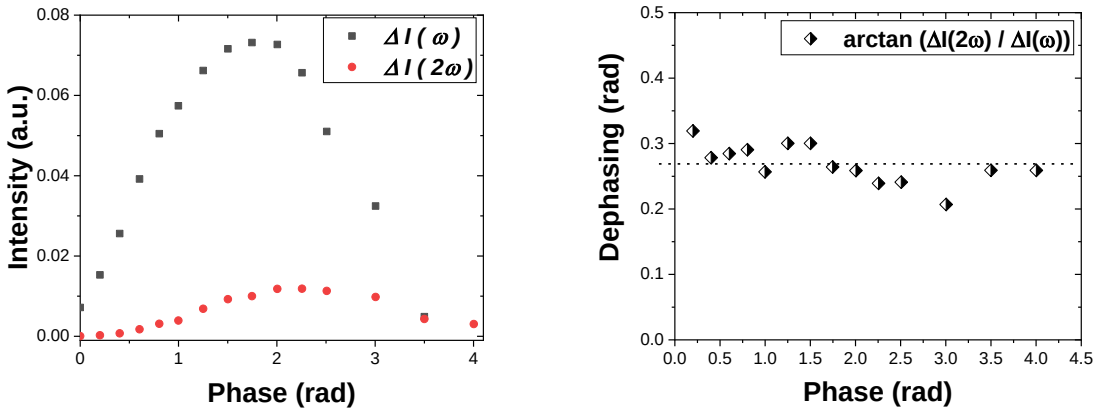

a. b.

Figure 4.11: (a) The difference between the intensities of the vertical and horizontal polarizations measured at ω and 2ω (b) The calculated value of φ as a function of φ_M.

We observe that the random phase varies slightly along the whole measurement time. The calculated mean value of the dephasing is $\varphi = 0.22$ rad. If we compensate for the effect of φ on $\Delta I(\omega)$ and $\Delta I(2\omega)$, meaning, that we substitute the value $\varphi = 0.22$ into equations (4.13) and (4.14) and re-plot them, we will be obtain Figure 4.12 a. In these new plots, we clearly see that $\Delta I(2\omega)$ and $\Delta I(\omega)$ follow the Bessel functions $J_2(\varphi_M)$ and $J_1(\varphi_M)$ respectively. In Figure 4.12 (b) the plot of the Bessel functions $J_n(\varphi_M)$, where n = 0, 1, 2 are compared to the graph 4.12 (a).

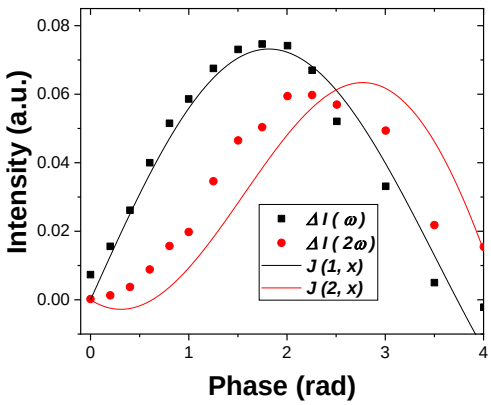

Figure 4.12: (a) Corrected values of differences between the intensities of the vertical and horizontal polarizations measured at ω (black squares) and 2ω (red disks). The lines correspond to the adjustment by the Bessel functions.

The value of $\Delta I(0)$ can also be obtained by monitoring the amplitude change in the detectors directly connected to the oscilloscope (not a synchronous detection anymore). In Figure 4.13 the measured

values of $\Delta I(0)$ is given as function of the amplitude of the phase modulation φ_M of the PEM. Here we also observe that $\Delta I(0)$ follows the Bessel function $J_0(\varphi_M)$ (see curve *J(0,x)* in Figure 4.12 (b)).

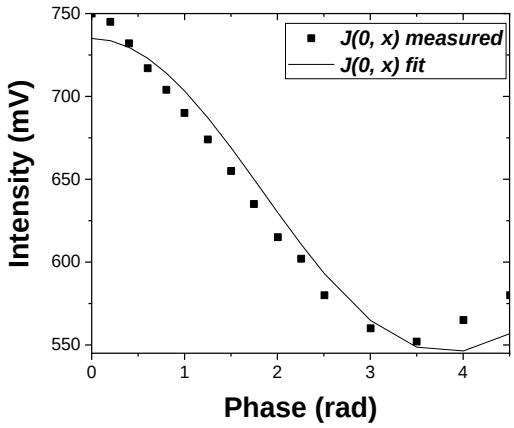

Figure 4.13: $\Delta I(0)$, the difference between the intensities of the vertical and horizontal components measured at $\omega = 0$ as a function of the phase φ_M of PEM with the Bessel function fit.

Our measurements prove that setup is behaving as expected considering the variation of φ_M. What is even more important, during the FR and the FE measurements, the value of the dephasing due to the birefringence in the optical fiber can be calculated and compensated. The offset observed for measured $J_0(\varphi_M)$ in Figure 4.13 is related to the background illumination coming from reflections on the different optical elements.

4.3 Magneto-optic sensor based on MCD

4.3.1. Magnetic field sensor device with one detector

4.3.2. Result of Faraday ellipticity only measurements

4.3.3. Effect of fiber orientation on the dephasing in the fiber

4.3.4. Using the fiber coupler in a magnetic field sensor device

4.3 Magneto-optic sensor based on MCD

4.3.1. Magnetic field sensor device with one detector

Considering equations (4.17) to (4.19), the intensities of the two orthogonal components of the beam passing through the Wollaston polarizer are added afterward! The detection scheme can then be simplified by using a single detector, instead of using the system: Wollaston polarizer, half-wave plate, and detectors. Doing so, the measurement is only sensitive to the FE but requires less elements and alignments. The MO response is measured for a synthesized garnet with about 150 nm thicknesses at the end of PM optical fiber with of 2-meter length.

In Section 2.1.1 we have described the nature of MCD and the related FE in MO materials. In Figure 4.14 we show schematically the magnetic field sensor-setup based on the single detector scheme.

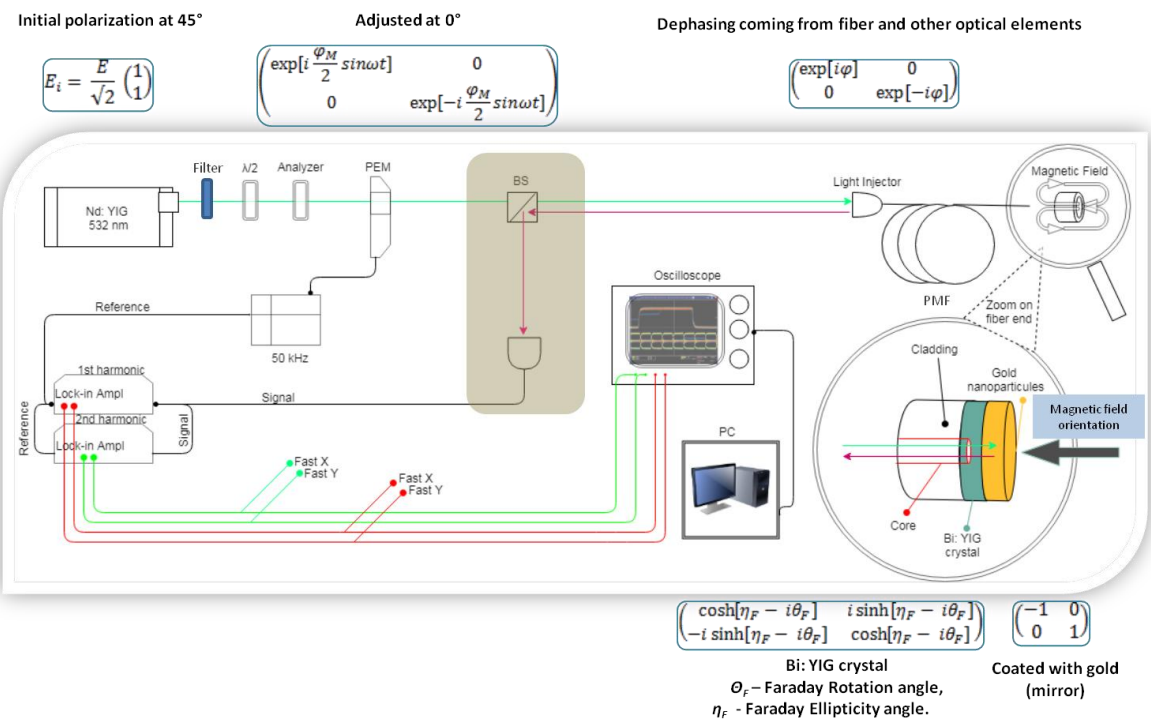

Figure 4.14: The scheme of the magnetic field sensor device based on the FE measurements indicating the Jones matrices for each optical element in the setup.

The Figure 4.14 presents almost the same scheme as given in Figure 4.7 but without the half-wave plate, the Wollaston polarizer, and with a single detector. This means, that we need to re-calculate the polarization state of the light after all the optical elements in the new setup, to measure the MO response. All other optical elements and parameters used for PEM, lock-in amplifiers, and magnetic field generators for magnetic field measurements are the same as the ones used previously. In this case, the final intensity will be defined from equation (4.6) as:

$$I(t) = E\{cosh\, 4\eta_F + \ (J_0(\varphi_M)\, sin\, \varphi + 2J_1(\varphi_M) sin\omega t\, cos\, \varphi + \ 2J_2(\varphi_M)\, sin\, 2\omega t\, sin\, \varphi\ )\, sinh\, 4\eta_F\}\,, \qquad (4.22)$$

where, once again, $J_{\mathrm{n}}(\varphi_M)$ are the Bessel functions for the orders n = 0, 1, 2 and φ_M is the amplitude of the dephasing generated by the PEM, ω is the frequency of the modulation of the light, η_F is the angle of the FE, and φ is the random dephasing related to the birefringences of the optical fiber and other optical elements. The intensity, in this case, depends only on the FE η_F, and do not on the FR θ_F. The intensities for the dc, first and second harmonic components can be retrieved from equation (4.22) and written as:

$$I(0) = \ E_i^2\ [\ cosh\, 4\eta_F + J_0(\varphi_{12})\, sin\, \varphi\ \ sinh\, 4\eta_F\ ]\,, \qquad (4.23)$$

$$I(\omega) = \ 2E_i^2 J_1(\varphi_{12})\, cos\, \varphi\ \ sinh\, 4\eta_F\ , \qquad (4.24)$$

$$I(2\omega) = \ 2E_i^2 J_2(\varphi_{12})\, sin\, \varphi\ \ sinh\, 4\eta_F\ , \qquad (4.25)$$

where, $\varphi_M = \varphi_{12} = 2.5\, rad$, and thus $J_1(\varphi_{12}) = \ J_2(\varphi_{12}) = 0.4623$. The value of the FE angle can be retrieved from equations (4.24) and (4.25) and is given by:

$$\eta_F = \ \frac{1}{4} asinh \frac{\sqrt{I(\omega)^2 + I(2\omega)^2}}{2E_i^2 J_1(\varphi_{12})}\,. \qquad (4.26)$$

Here we have, as expected, the same hyperbolic sine function in the expressions of the intensities as we had for the previous scheme with two detectors and a Wollaston polarizer (see equation (4.19)).

4.3.2. Result of Faraday ellipticity only measurements

As before, the magnetic field at end of the optical fiber is modulated at 23 Hz with amplitudes varying in the range 2 mT – 10 µT. The results are presented in Figure 4.15, where the Fourier spectrum of the FE response (Figure 4.15 (a,b)) shows the expected narrow peak at 23 Hz.

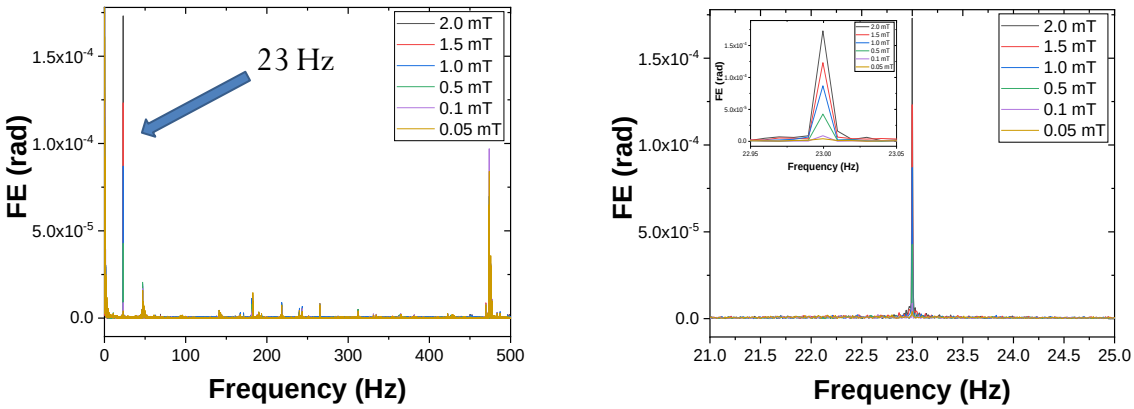

a. b.

Figure 4.15: (a) Fourier spectrum of the FE response, (b) FE dependency on the amplitude of the magnetic field.

In Figure 4.15, the highest peak at 23 Hz corresponds to the MO response. It is easily distinguished from other peaks with low amplitudes, which correspond to FE signal harmonics at 46, 69, 92 Hz and so on. The FE dependence on the amplitude of the magnetic field is given in Figure 4.16.

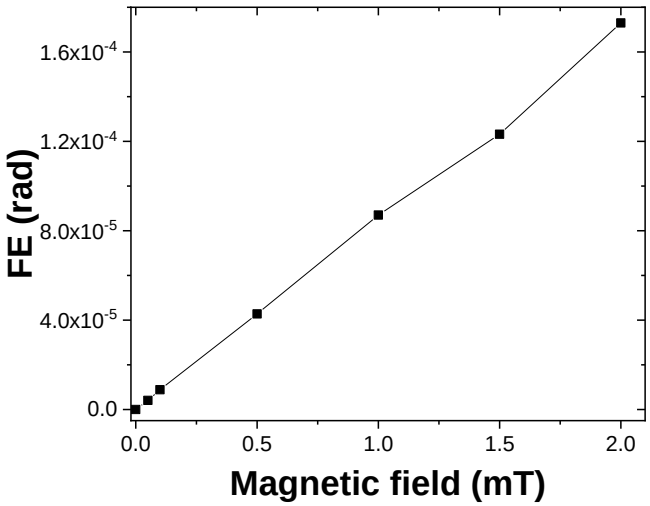

Figure 4.16: Measured FE as a function of the amplitudes of the magnetic field.

In Figure 4.16, we observe the expected linear dependence of FE on the amplitude of the applied magnetic field.

The Figure 4.17 shows the measured FE response as a function of time for different shapes of the amplitude variation of the magnetic field with s 1 mT amplitude and a 23 Hz modulation frequency.

The FE accurately follows the change in the magnetic field. Figure 4.18 displays the changes in the FE response as a function of the frequency of the generated magnetic field signal with a square function. The frequency is varied in the range from 23 Hz up to 0.5 kHz. Here, we observe the changes in the shape of the signal with increasing the frequency, and as a result, the square signal at 23 Hz becomes close to sine function at 0.5 kHz. This is due to the slow changes in the magnetization of the iron core. Consequently, we forced work below 100 Hz.

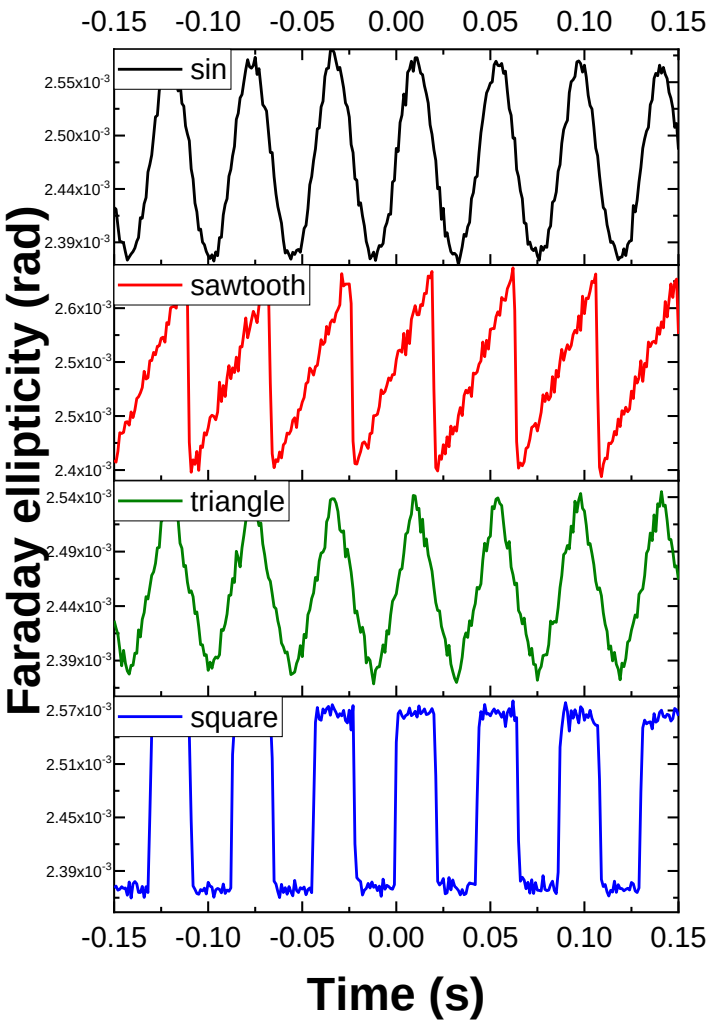

Figure 4.17: FE as a function of time with different variation functions for the applied magnetic field.

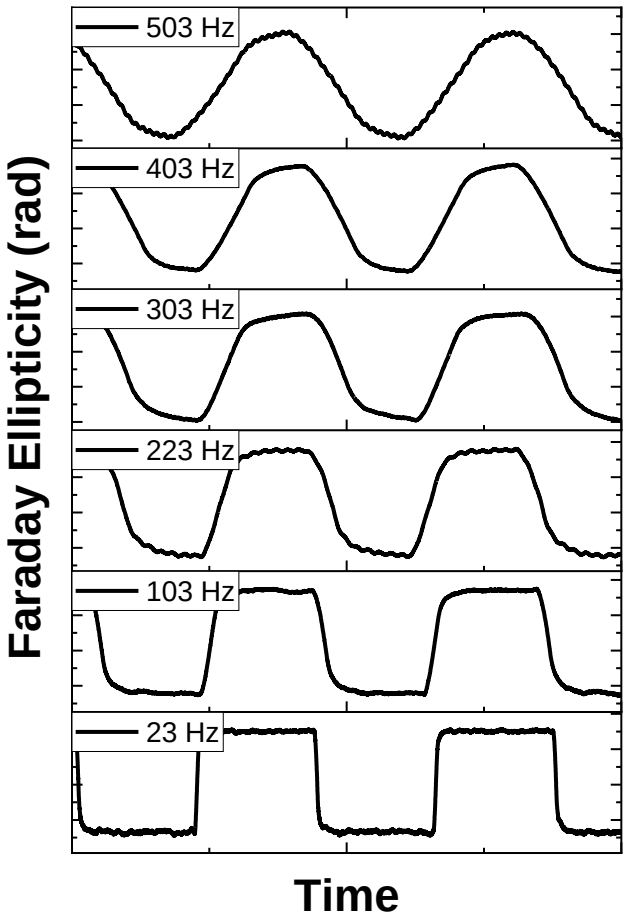

Figure 4.18: FE as a function of the frequency of the generated square magnetic field.

4.3.3. Effect of fiber orientation on the dephasing in the fiber

In Section 4.2.4, to check the model of the setup, we showed the variation of the signal with the amplitude of phase modulation generated by the PEM. Again, to check the validity of the model and consequently of the measurements, we compare the calculation of the effect of the rotation of a polarization maintaining fiber considering a fixed input linear polarization.

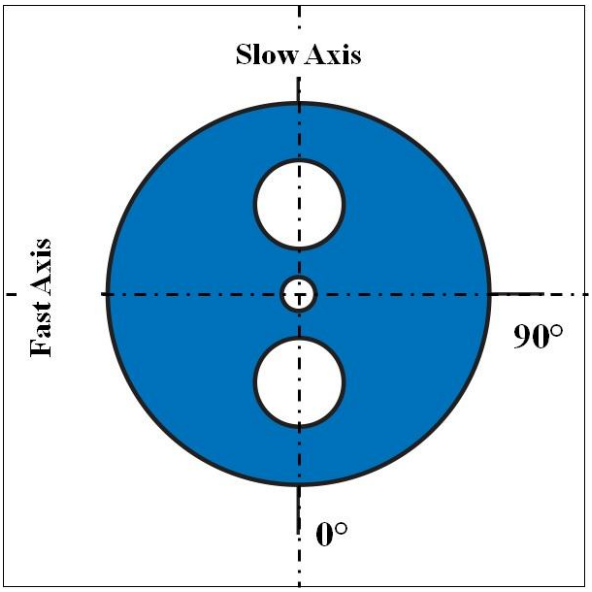

Figure 4.19: Polarization maintaining (PM) "Panda" type fiber, with slow and fast axes indicated.

The equation (4.20) we used can be modified to take into the account the orientation of the fiber before the injection of the beam. The expressions (4.18) and (4.25) need to be modified by adding an additional parameter, an angle of orientation ξ, compared to the direction of the major axis of the PEM. A scheme of a PM fiber is presented in Figure 4.19. The equations (4.17) and (4.24) for $I(\omega)$ will remain unchanged. The modified equations corresponding to (4.18) and (4.25) can be expressed in the following form:

$$I(2\omega) = 2E_i^2 J_2(\varphi_{12}) \cos 2\xi \sin\varphi \ \sinh 4\eta_F \ . \tag{4.27}$$

Next, equation (4.20) can be rewritten as:

$$\frac{I(2\omega)}{I(\omega)} = \frac{2E_i^2 J_2(\varphi_{12}) \cos 2\xi \sin\varphi \ \sinh 4\eta_F}{2E_i^2 J_1(\varphi_{12}) \cos\varphi \ \sinh 4\eta_F} = \frac{\cos 2\xi \sin\varphi}{\cos\varphi} . \tag{4.28}$$

The dephasing φ can be extracted from equation (4.28) as:

$$\varphi = \arctan\left(\frac{I(2\omega)}{I(\omega)\cos 2\xi}\right) . \tag{4.29}$$

To monitor the actual effect of the fiber orientation angle ξ on the FE measurements, we carry out the experiment where the intensity $I(\omega)$ and $I(2\omega)$ are measured as a function of the orientation angle ξ in the range from 0° to 180°. The results are presented in Figure 4.20 (a). Here, we observe, that the intensity *I(2ω)* varies with the increase orientation angle as a cosine function, while the value $I(\omega)$ is not changing. These results are in good agreement with our model. Also, the experimental value for $I(\omega)$ at $2\xi = 90°$ is out of range, as the argument of the arctangent function is undefined in equation (4.29) (see Figure 4.20 (a)).

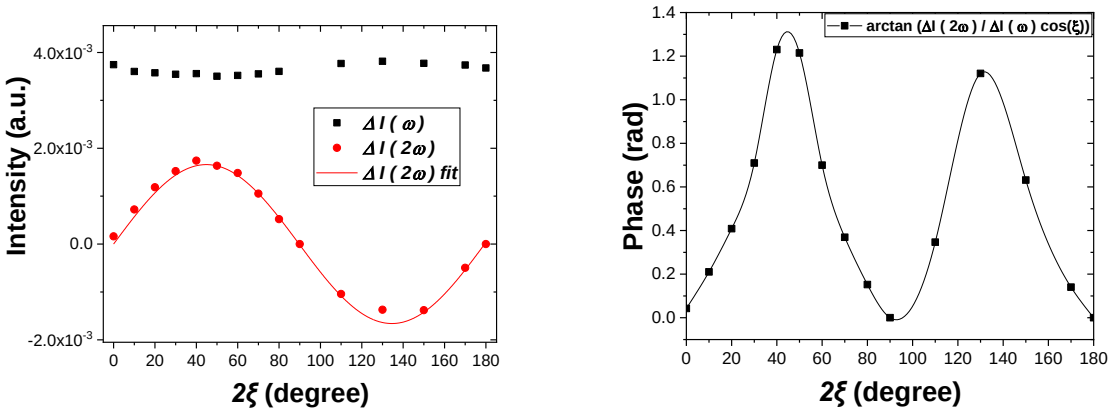

a. b.

Figure 4.20: (a) Dependence of the intensities of the first and second harmonic components on the orientation angle of the fiber. The line correspond to the adjustment by the calculated response of the setup. (b) dephasing φ as a function of the orientation angle of the fiber ξ.

In Figure 4.20 (b) the dephasing φ is plotted as a function of the orientation angle of the fiber ξ. As we see in this figure the value of FE has a strong dependence on the orientation angle of the fiber. The impact of this parameter can be lessened or even cancelled if we set the orientation at 0° (slow axis) or 90° (fast axis) relatively to the incoming beam's polarization state.

4.3.4.Conclusion

To conclude, we are able to prepare not only the garnet thin layers but also microcrystals with 2-3 µm size on the core of the optical fiber. The obtained results of FR and FE showed that magnetic fields from 100 mT down to a few µT for such fibered MO sensor can be easily detected. The magnetic field measurements based on FE is very promising, as far the sensitivity is comparable to the device based on FR, but with a much-simplified detection system.

General Conclusion

The main results of this work are:

- We have studied the crystallization of Bi: YIG films prepared on silica substrates using the MOD process by systematically varying the initial composition and annealing temperate and annealing time duration. Different initial compositions of $Bi_xY_{3-x}Fe_5O_{12}$ has been prepared varying the ratio between yttrium and bismuth for the same amount of iron (x_{ini} = 0.8, 1, 1.3, 1.6, 1.9 and 2.2). The annealing temperature varied in the 650 °C to 750 °C range at variable durations from 4 to 26 hours. The best performances of the FR of -5°/µm at 532 nm have been obtained for Bi: YIG films with initial composition x_{ini} = 1.3 prepared ay 680 °C for 10 hours.

- The crystal structure and surface morphology of films annealed at 660 °C have been analyzed by XRD, SEM, and AFM measurements. These measurements confirm that the reaction scheme strongly depends on the initial composition. Indeed, the increase of the initial amount of bismuth favors the garnet phase but also triggers competing side reactions. The measurements reveal the presence of $YFeO_3$ and Fe_2O_3 for x > 1.3.

- Powders for different compositions of Bi: YIG has been also prepared at 660 °C for 5 hours. The powders used for DTA and SEM analyses. These results helped for understanding the crystallization Bi: YIG process and present the reaction scheme during the Bi: YIG annealing.

- Measurements of the evolution of the FR during the annealing procedures have been used to calculate of the rate of chemical reaction of the synthesis and decomposition of Bi: YIG crystals in the film material, which in turn give access for calculation the activation energy of the Bi: YIG synthesis for thin films. The crystallization activation energy of 175 ±5 kJ/mol for Bi: YIG in the films have been done through the MO measurements, while the calorimetric method cannot be used.

- We have shown two methods of preparation of Bi: YIG material at the end of an optical fiber, by using liquid metal-solution with initial composition x_{ini} = 1.3. The first method allows us to obtain a thin film of Bi: YIG covering the end of an optical fiber. The second method allows us to obtain the Bi: YIG particle, which is self-centered on the exiting optical mode with approximate size 2-3 micrometers. The thickness of MO material can be controlled by repeating the coating process.

- The experimental setup for the magnetic field measurements has been developed and its operation has been demonstrated. The obtained results for FR and FE measurements showed that magnetic fields from 100 mT down to a few µT for such a fibered MO sensor can be easily detected. In addition, the MO sensor device based on FE measurements has been demonstrated. The obtained results comparable to the device based on FR, but with a much-simplified detection system.

This study is conducted in the framework of the ANR project FOGAMO; The main objective of this was to demonstrate the possibility to perform the measurement of a magnetic field via an optical fiber functionalized with a Bi: YIG. We consider that the objective has been successfully reached. The limited time of the project forced us to progress continuously and some aspects have therefore been neglected. The preparation of the material can still be improved especially concerning the

homogeneity of the films. The measurement setup can also be upgraded. Going to a full fibered setup including a fiber coupled laser source, a fiber splitter and fiber electro-optic modulator will certainly improve the performances reducing the noise coming from the parasitic reflections of the optics.

We will conduct part of this tasks in the framework of a new ATTRACT/CERN/H2020 contract. Here, we are considering the preparation of other garnet phases or of polymer doped with magnetite nanoparticles that may exhibit higher sensitivity in the NIR that will fit with the telecom wavelength technology. New developments considering the MO properties of conjugated polymer are also being considered. These materials show tremendous MO properties and can also be considered for optical fiber functionalization. We expect this work to help to define the origin of the MO response that is still not clearly understood in these polymers.

Scientific production:

Oral presentations:

SPIE Photonics Europe 2018, Strasbourg, Paper: 10680-52.

SPIE Optics + Photonics 2019, San-Diego, paper 11088-24.

SPIE Security + Defence 2019, Strasbourg, paper 11165-6. (Invited)

Article :

I. Nadinov, O. Kovalenko, J.-L. Rehspringer, M. Vomir, L. Mager, « *Limits of the magneto-optical properties of Bi: YIG films prepared on silica* by metal organic decomposition », Ceram. Int., In press, available online: doi.org/10.1016/j.ceramint.2019.07.129 (2019)

RÉSUMÉ DE LA THÈSE DE DOCTORAT

Introduction

La plupart des dispositifs à fibres décrits dans la littérature trouvent leur application dans la détection de courant électrique, principalement pour des lignes à haute tension. Ils utilisent l'effet Faraday induit dans une fibre enroulée autour du conducteur. Une mesure plus locale du champ magnétique, à l'échelle millimétrique ou inférieure, nécessite des valeurs de rotation de Faraday beaucoup plus élevées que celles accessibles dans les fibres de silice. Pour accéder à une résolution spatiale élevée, une solution consiste donc à fonctionnaliser l'extrémité d'une fibre optique avec un matériau magnéto-optique (MO) efficace qui permettra la détection. Le rôle de la fibre se réduit alors à guider la lumière entre les systèmes d'illumination / analyse du signal et le matériau MO distant. Pour de telles applications, le matériau apparaissant le plus pertinent est le Bi: YIG qui présente une rotation de Faraday d'environ 1000 °/cm à saturation de l'aimantation. Cette solution a déjà été démontrée par H. Sohlström et K. Svantesson [1] en utilisant des cristaux de Bi : YIG obtenus par épitaxie sur des substrats de GGG. Ici, le cristal est coupé, poli, puis soigneusement aligné et fixé à l'extrémité de la fibre optique. Un support mécanique assure la résistance de la tête de détection. La taille d'un tel capteur est de l'ordre de quelques millimètres. Nous proposons de réduire considérablement la taille de la partie sensible au champ magnétique et de simplifier considérablement la procédure d'assemblage en synthétisant in situ un microcristal de Bi: YIG , directement à l'extrémité d'une fibre optique.

Nous avons développé une méthode originale pour la préparation de Bi: YIG à partir de précurseurs organométalliques liquides. Ces liquides peuvent être préparés à température ambiante, dans une atmosphère normale et ils présentent une très faible toxicité. L'optimisation du processus passant par celle de la formulation initiale et des traitements thermiques a permis la réalisation de films minces de Bi: YIG sur des plaques de silice. Ces films permettent d'atteindre des rotations Faraday de l'ordre de 1600 °/cm à saturation de l'aimantation [2, 3]. Comme la solution initiale est sensible à la lumière, la croissance de la phase grenat à partir de la solution peut être limitée à la zone du mode sortant de la fibre en injectant un faisceau lumineux par l'autre extrémité de la fibre pour induire une structuration. Il est alors possible d'obtenir un cristal de quelques micromètres, auto-centré sur le cœur de la fibre, sans qu'il soit besoin de mise en forme ni d'alignement délicats.

Préparation, caractérisation et optimisation du matériau

La première étape de ce projet, a été consacrée à l'étude du processus de synthèse du grenat et à son optimisation. Notre préoccupation était de d'approfondir la compréhension du processus de synthèse du matériau MO afin de contrôler sa mise en œuvre dans les dispositifs prévus. Les propriétés MO du matériau augmentent avec le taux de substitution du bismuth et avec la concentration de la phase grenat dans le produit final. Comme ces quantités dépendent de la formulation de la solution initiale, de la durée et de la température de recuit, nous avons effectué une étude systématique en faisant varier ces paramètres. Notre intérêt s'est porté principalement sur l'efficacité MO qui a guidé l'optimisation du processus. Mais la compréhension complète de la réaction de synthèse a nécessité des caractérisations supplémentaires (DRX, AFM, DSC…). Nous avons pu ainsi démontrer que le taux de substitution accessible via le procédé MOD était limité à 1,6 et que, pour une concentration élevée de bismuth dans la solution initiale, des produits annexes apparaissent dans le matériau final, réduisant ainsi la concentration de grenat et donc les performances MO. Au cours de la procédure de recuit, nous avons pu suivre l'évolution des performances du MO qui peuvent être attribuée à la croissance de la seule phase grenat. En effet, les propriétés MO des produits secondaires sont inférieures de plusieurs ordres de grandeur à celles du Bi: YIG. À partir de ces données, nous avons pu extraire l'énergie d'activation de la cristallisation et de la dégradation de la phase grenat sans faire appel à des mesures calorimétriques.

Ce travail nous permet à présent de contrôler efficacement la synthèse du grenat et préparer le matériau avec une efficacité de MO maximale et cela de façon reproductible.

A. Procédure MOD pour la préparation de Bi: YIG

La solution liquide initiale contient les différents chélates de métal (MC), dissous dans de l'acide propionique. Différentes compositions initiales sont préparées en faisant varier le rapport entre l'yttrium et le bismuth pour une même quantité de fer (x_{ini} Bi, (3-x_{ini}) Y, 5 Fe avec x_{ini} = 0,8 ; 1,0 ; 1,3 ; 1,6 ; 1,9 et 2,2). Pour rester dans les limites de solubilité, la concentration totale de MC est fixée à 1 mol / L. Ces solutions sont déposées par centrifugation sur des substrats de silice de 1 cm x 1 cm à 2000 tr / min pendant 1 minute pour la préparation du film. Immédiatement après le dépôt, leurs épaisseurs sont mesurées par microscopie interférométrique sans contact (Zygo NewView 6300) donnant des valeurs de l'ordre de 500 nm. Un premier séchage à l'air libre suivi d'une pyrolyse de 40 minutes à 300 °C élimine la partie organique et laisse une couche d'oxyde métallique amorphe d'environ 50 nm d'épaisseur. Ce processus de dépôt et de séchage est répété jusqu'à cinq fois pour atteindre une épaisseur d'environ 250 nm avant le processus de recuit final. La dernière étape est un recuit thermique (650 °C – 750 °C, 1 – 20 heures) conduisant à la synthèse de la phase grenat.

B. Caractérisation magnéto-optique du matériau

Pour étudier les propriétés magnéto-optiques du grenat, nous avons préparé des films minces sur un substrat de silice et mesuré les angles de rotation et d'ellipticité de Faraday. Le montage expérimental pour les mesures FR est présenté sur la Figure 1. La source de lumière est une lampe au xénon permettant une mesure résolue spectralement entre 300 nm à 800 nm. Le faisceau est polarisé avant de traverser le modulateur photoelastique (PEM) qui module l'état de polarisation. L'échantillon placé dans un champ magnétique continu qui induit la variation de la polarisation de la lumière via l'effet Faraday. La lumière sortant de l'échantillon traverse l'analyseur, puis le spectromètre et est finalement détectée par un photomultiplicateur.

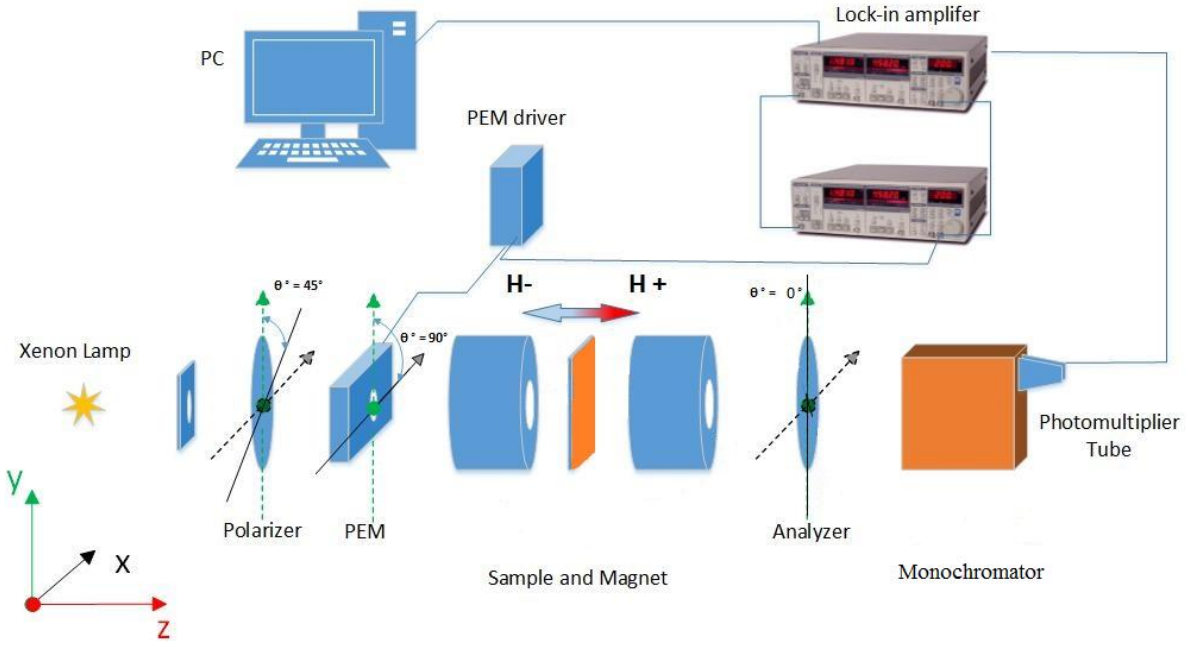

Figure 1 : Configuration expérimentale pour les mesures de l'effet Faraday.

Nous avons effectué une étude systématique de la préparation de grenats substitués en faisant varier la composition initiale, la durée et la température de l'étape de recuit. Le seul paramètre qui a guidé l'optimisation était l'efficacité de rotation Faraday à 532 nm, la longueur d'onde ciblée pour le dispositif de détection magnétique fibré.

La Figure 2 (a) présente la variation spectrale de la rotation de Faraday à saturation pour les films préparés au début de cette étude avec des quantités initiales de bismuth différentes et un recuit à 700 °C pendant 1 heure. La saturation de l'aimantation a été vérifiée à $\lambda = 532$ nm pour les différentes compositions. Cette saturation est obtenue autour de 0,1 T, comme cela est généralement observé dans Bi: YIG.

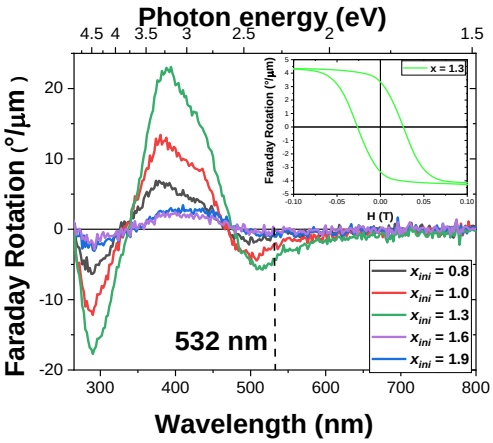

a.

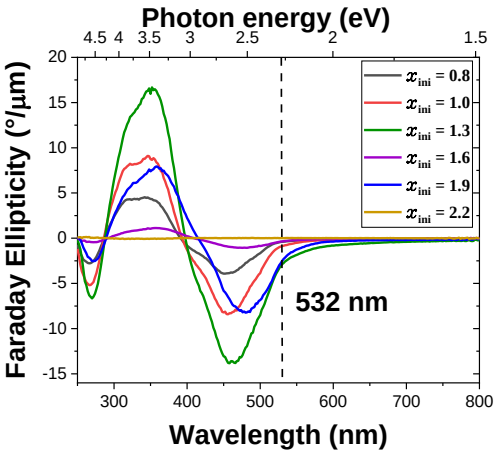

b.

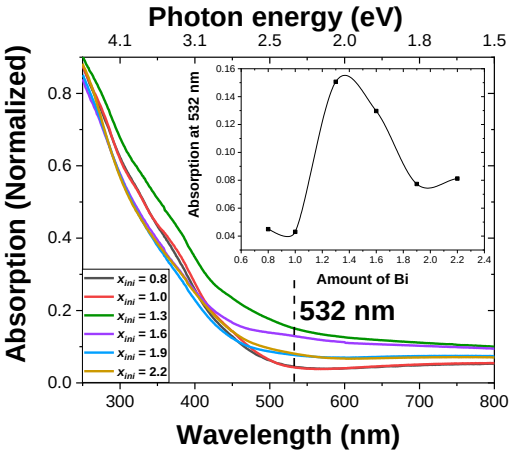

c.

Figure 2 : (a) Spectre de rotation de Faraday (Encart: mesure de l'hystérésis MO à 532 nm pour x_{ini} = 1.3), (b) Spectre de ellipticité de Faraday à saturation pour les films de Bi: YIG sur substrat de silice avec différentes quantités initiales de bismuth, recuit à 700 ° C pendant 1 heure. (c) L'absorption optique pour les mêmes films. Encart: absorption optique à 532 nm (la ligne sert de guide pour les yeux).

Les amplitudes des pics de 390 nm et 516 nm, attribuées au grenat substitué bismuth, augmentent d'abord avec la quantité initiale de bismuth, puis diminuent après un maximum observé pour x_{ini} = 1,3. L'absorption optique à 532 nm, variant également avec le taux de substitution du bismuth, montre une variation similaire (voir Figure 2 (b)).

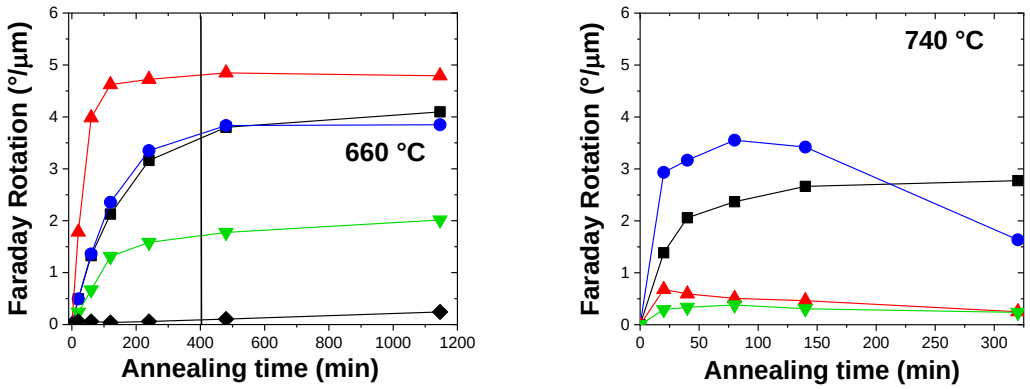

a. b.

Figure 3 : Evolution de l'angle de rotation de Faraday avec le temps de recuit pour les différentes quantités initiales de bismuth à (a) 660 ° C et (b) 740 ° C. Carré noir: x_{ini} = 0,8 ; disque bleu: x_{ini} = 1,0 ; triangle rouge: x_{ini} = 1,3 ; triangle vert: x_{ini} = 1,6 ; carré noir: x_{ini} = 1,9.

L'utilisation d'un four (LINKAM Scientific TS1500) inséré directement dans le dispositif expérimental nous a permis de suivre l'évolution de la rotation de Faraday pendant le recuit, en évitant ainsi toute erreur de repositionnement. Les recuits ont été faits pour des températures variant entre 650 °C et 750 °C pour des durées variables. Pour la mesure de l'angle de rotation de Faraday, θ_F, l'échantillon est rapidement refroidi sous le point de Curie (mesuré autour de 315 °C dans nos matériaux), puis ramené tout aussi rapidement à la température de recuit. La Figure 3 présente deux exemples d'évolution de l'angle de rotation de Faraday mesuré à saturation de l'aimantation pour deux températures de recuit. Ils ont clairement démontré que les trois paramètres: la température de recuit, la durée du recuit et la composition initiale affectaient la réponse de MO. Nous avons optimisé ces paramètres simultanément et obtenu un effet MO maximum pour une substitution autour de x_{ini} = 1,3, et un recuit à 660 °C pendant 400 minutes donnant une rotation de Faraday à saturation de 5 °/µm à 532 nm.

C. Caractérisation structurelle du matériau

La diffraction des rayons X (XRD) et la caractérisation structurelle (SEM, AFM) nous ont apporté les informations nécessaires à l'identification des différentes phases présentes dans le matériau final. Les mesures de XRD des échantillons recuits à 660 °C pendant 400 minutes sont présentés figure 4.

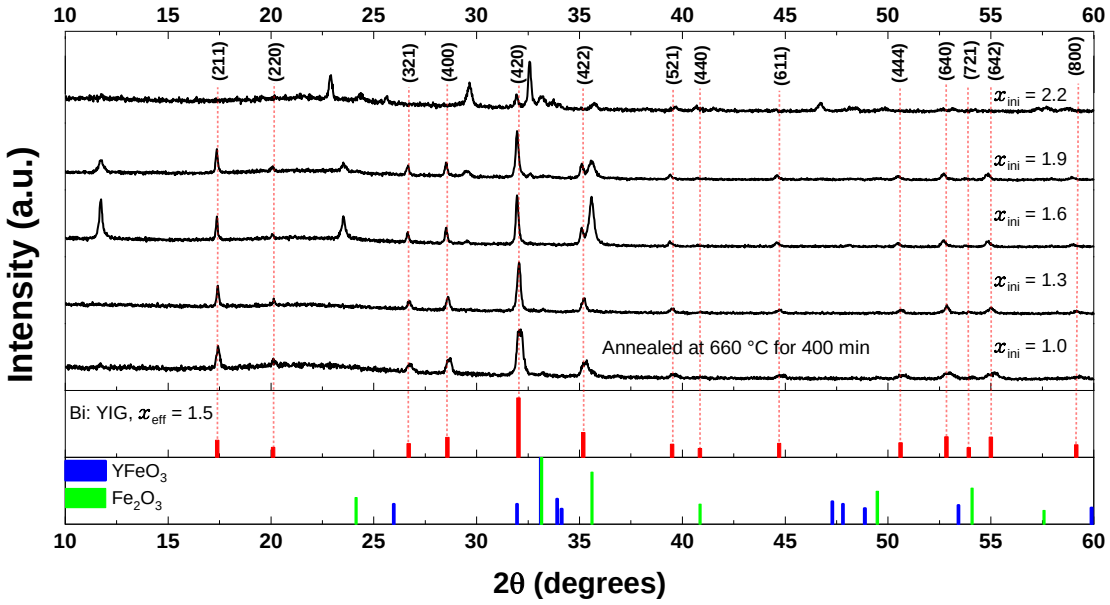

Figure 4 : Diagrammes XRD des films Bi: YIG recuits à 660 °C pendant 400 min. pour différentes quantités initiales de bismuth: x_{ini} = 1,0 ; 1,3 ; 1,6 ; 1,9 ; 2,2. En bas, les histogrammes donnent les positions tabulées et les intensités relatives des pics de diffraction pour Bi: YIG, $YFeO_3$ et Fe_2O_3.

Pour des quantités initiales de bismuth allant jusqu'à x_{ini} = 1,3, aucune autre espèce cristalline en dehors de Bi: YIG n'a été détectée. En augmentant encore la concentration initiale en bismuth, de l'orthoferrite d'yttrium ($YFeO_3$) et de l'oxyde de fer (Fe_2O_3) sont apparus, coexistant avec une phase homogène Bi: YIG, comme l'indique l'étroitesse des pics. À la concentration de bismuth la plus élevée, x_{ini} = 2,2, la quantité de Bi: YIG chute très fortement.

Connaissant le paramètre de réseau, on peut estimer la quantité effective de bismuth dans la phase de grenat. Le calcul de ces paramètres, d'après les données XRD, a montré une nette augmentation avec la quantité initiale de bismuth saturant au-dessus de x_{ini} = 1,6 (voir la Figure 5).

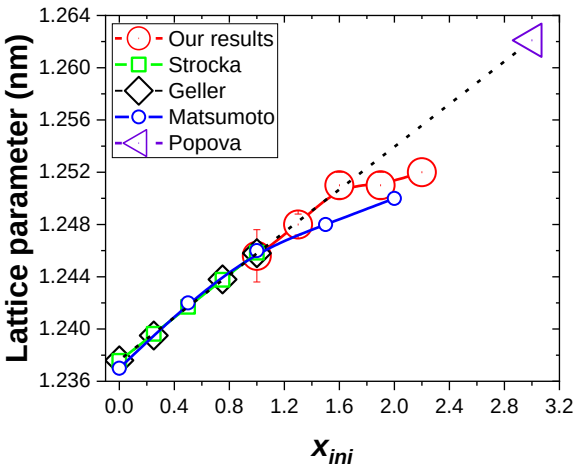

Figure 5 : Evolution du paramètre de réseau du Bi: YIG avec la quantité de la partie initiale de Bi comparée aux paramètres de réseau mesurés parMatsumoto et al. [131], Geller et al. [150], Strocka et al. [151] and Popova et al. [135].

Des techniques de microscope électronique à balayage (SEM) et de microscope à force atomique (AFM) ont été utilisées pour produire les images des échantillons nécessaire à un aperçu de la morphologie du matériau synthétisé et d'apporter quelques corrections dans la préparation des solutions et des échantillons.

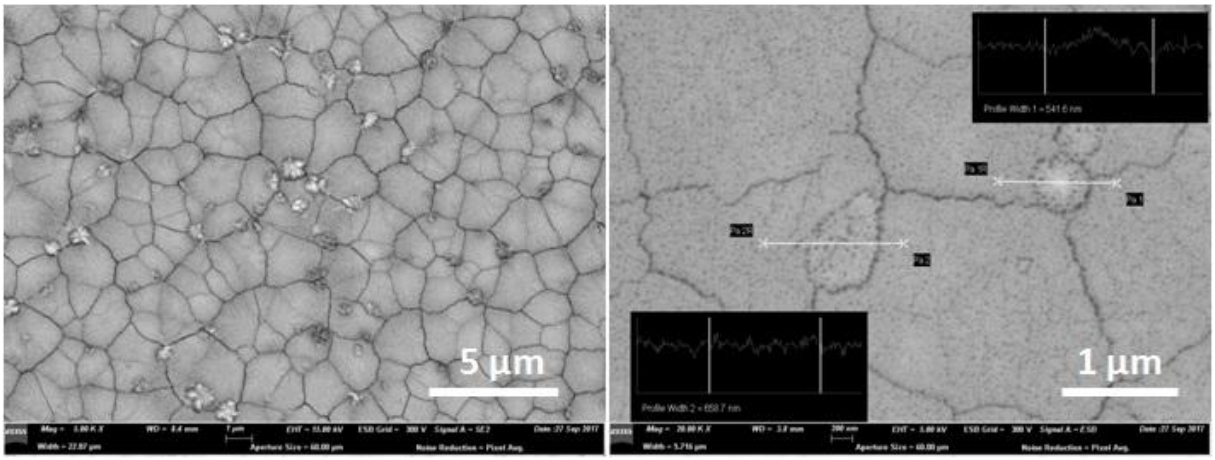

(a)

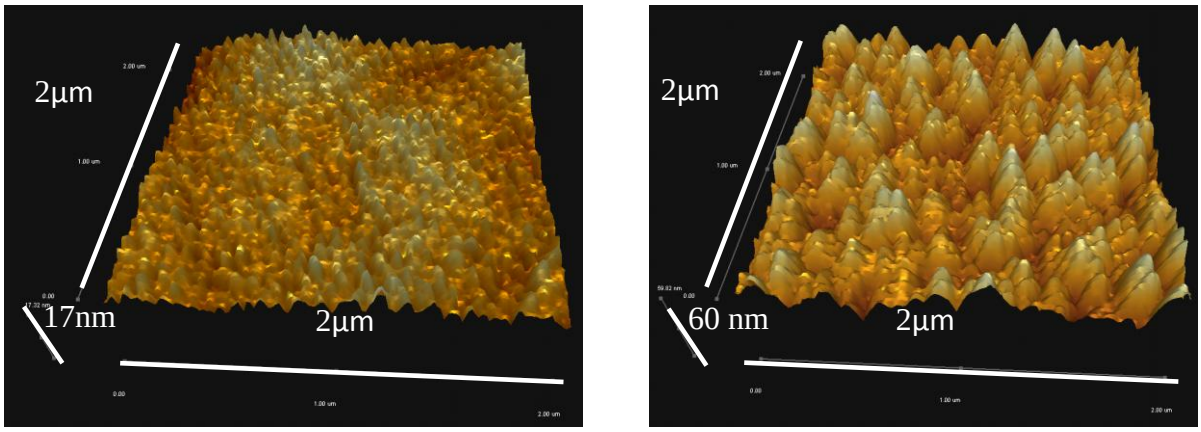

(b)

Figure 6: (a). Mesures SEM des films de Bi: YIG de x_{ini} = 1,0 et x_{ini} = 1,3 multicouches recuits à T = 660 °C; (b) images AFM des films de Bi: YIG pour x_{ini} = 1,0 et x_{ini} = 2,2.

La morphologie de surface observée par SEM est présentée à la Figure 6 (a). Il en ressort que de nombreuses fissures apparaissent sur la couche avec une taille moyenne de 2 à 5 µm. Nous observons trois niveaux de gris distincts attribués à trois phases distinctes : le gris clair peut être attribué à la phase $BiFeO_3$, le gris moyen au grenat et le gris foncé à $YFeO_3$,en supposant que le poids atomique moyen correspond à une absorption atomique relative.

Avec les mesures AFM, nous avons réalisé que la surface avait une structure granuleuse et que la taille des grains dépend de la composition de l'échantillon. Figure 6 (b), par exemple, pour l'échantillon x_{ini} = 1,0 la taille caractéristique des grains d'environ 0,4 µm et de 0.85 µm pour x_{ini} = 2,2.

Fonctionnalisation d'une fibre optique par le grenat

La préparation du grenat Bi: YIG à haute efficacité sur des plaques de verre de silice maitrisée, nous nous sommes tournés vers la fonctionnalisation de la fibre optique. Ici, deux possibilités sont ouvertes. La première consiste simplement à recouvrir l'extrémité de la fibre avec la solution initiale et à effectuer le processus de synthèse du grenat pour obtenir un film couvrant toute la surface. L'autre possibilité consiste à structurer le matériau pour obtenir un grenat microscopique à l'extrémité de la fibre. Pour ce faire, nous avons induit un premier séchage de la solution en injectant de la lumière dans la fibre. Le mode sortant est absorbé par la solution, ce qui entraîne un chauffage et un séchage local de la solution. Après avoir rincé la solution non solidifiée, il reste une petite quantité de matière séchée, centrée sur le cœur de la fibre. Le grenat micrométrique final est obtenu après le traitement thermique.

Tout d'abord, nous recouvrons l'extrémité fraîchement coupée de la fibre optique avec la solution puis l'agitons manuellement la fibre pour éliminer la solution en excès et laissons sécher la solution restante à température ambiante afin d'obtenir une couche mince amorphe et plate. Puis, nous induisons un chauffage local au niveau du cœur de la fibre optique en injectant de la lumière. Le chauffage est contrôlé par la puissance de la source laser. En pratique, la densité de puissance ($\approx$ 100 kW/cm^2) de la lumière confinée dans le cœur de la fibre suffit pour réaliser l'évaporation du solvant et l'élimination de la partie organique de la couche mince au niveau du cœur de la fibre optique. Un rinçage élimine la partie non séchée et conserve la partie irradidiée. Cette étape reproduit l'étape de pyrolyse du processus MOD. Dans la dernière étape, l'extrémité de la fibre optique est placée dans le four à T = 300 – 400 °C pendant 15 à 30 minutes.

La procédure présentée dans le paragraphe précédent peut être répétée aussi souvent que nécessaire pour atteindre les épaisseurs de matériau souhaitées. Finalement, l'extrémité est recuite à 660 °C pendant 3 – 4 heures. On obtient ainsi un grenat Bi: YIG de 2 µm de large et 0,2 à 10 µm d'épaisseur fixée (voir figure 7).

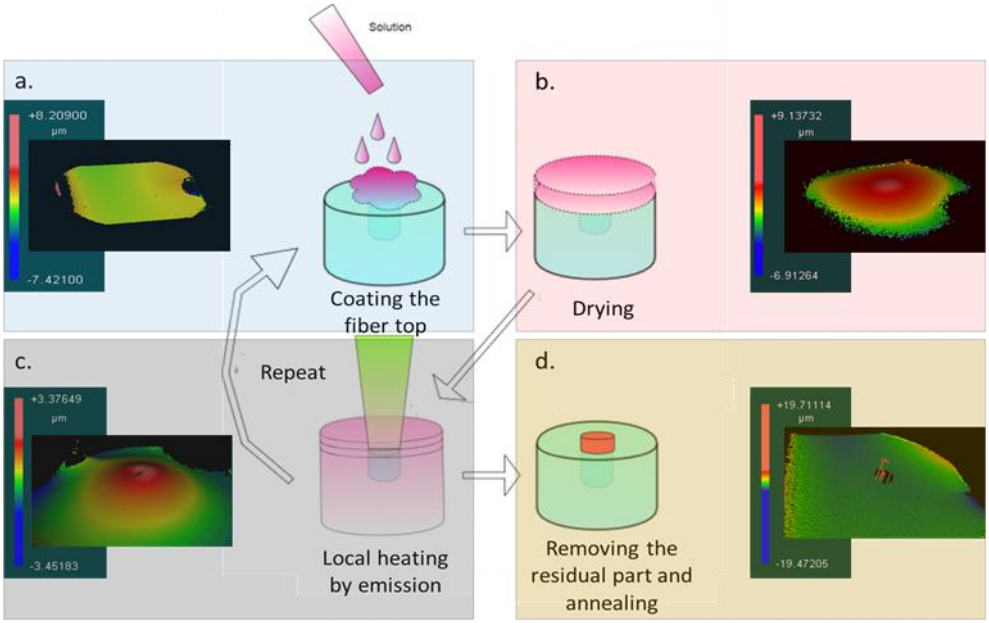

Figure 7: Schéma de la production du Bi: YIG sur le coeur de la fibre optique accompagné de mesures d'interférométrie microscopique de la topographie de surface.

Les images en microscopie électronique à balayage (SEM) et interférométrie microscopique du Bi: YIG développé à l'extrémité de la fibre optique sont illustrées à la Figure 8. Ici, la taille de la partie sensible est limitée à la taille du coeur de la fibre. Comparé au capteur fibré à base de Bi: YIG développé par H. Solhstrom et al. [1], aucun dispositif de maintien mécanique ni aucun dispositif d'alignement ne sont nécessaires, ce qui en fait l'un des capteurs les plus simples et les plus compacts possible.

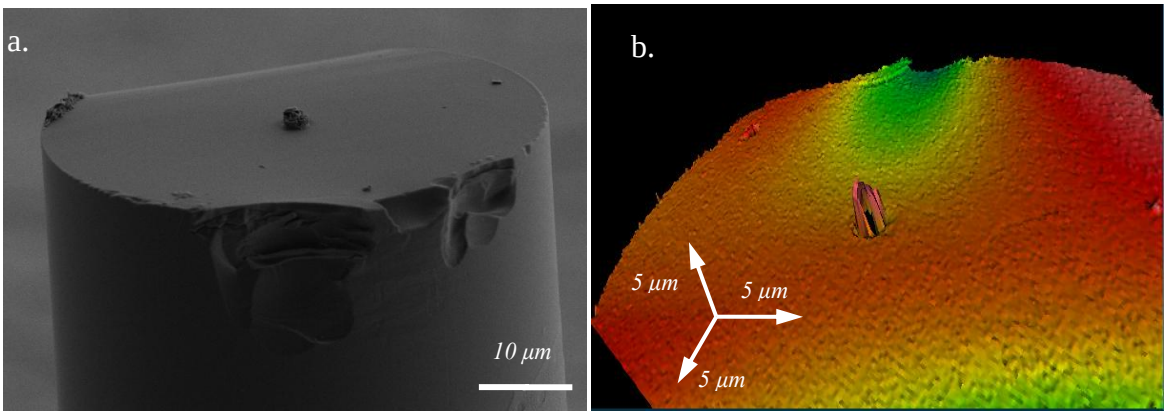

Figure 8 (a) Images MEB du microcristal Bi: YIG synthétisé sur le cœur de la fibre optique de composition initiale x_{ini} = 1,3. La procédure de dépôt par la méthode MOD a été répétée 5 fois et recuite à 660 °C pendant 400 minutes. (b) Image de microscopie interférométrique du microcristal Bi: YIG sur le cœur de la fibre optique.

Détecteur magnéto-optique utilisant la fibre fonctionnalisée

La dernière partie de ce travail consistait à démontrer la possibilité de construire un capteur magnétique utilisant la fibre fonctionnalisée. Notre principale préoccupation était ici de préserver la petite taille de l'extrémité de détection. En effet, dans les configurations similaires décrites dans la littérature, les opérations de détection nécessitent un élément optique supplémentaire positionné à proximité de la tête MO. Cela augmente considérablement la taille du capteur. Nous développons une nouvelle solution basée sur la modulation de polarisation qui évite l'utilisation de cet élément supplémentaire. De plus, le schéma de détection fonctionne sur l'effet Faraday mais également sur le dichroïsme circulaire magnétique, ce qui n'a pas été décrit dans la littérature (revues ou brevets). Nous avons démontré que notre appareil est capable de mesurer un champ magnétique jusqu'à quelques microteslas.

Le dispositif expérimental a été conçu pour fonctionner 532 nm, de nombreuses sources laser étant disponibles à cette longueur d'onde. La lumière est modulée par un modulateur photo-élastique (PEM) à une fréquence de 50 kHz. Notre configuration nécessite une fibre optique monomode (SMF) ou une fibre à maintien de polarisation pour transmettre la lumière laser jusqu'au grenat. La mesure du champ magnétique est réalisée par l'analyse de la polarisation de la lumière réfléchie en utilisant un prisme de Wollaston et une détection différentielle, comme illustré Figure 9. Nous séparons une fraction du signal avec un séparateur de faisceau, positionné avant l'injection de la lumière dans la fibre.

Pour mesurer la réponse MO provenant du grenat synthétisé à l'extrémité de la fibre, nous devons définir la réponse du dispositif et l'état de polarisation de la lumière après son passage à travers tous les éléments optiques du montage. Pour cela, nous utilisons le formalisme de Jones, où la polarisation de la lumière est représentée par un vecteur et les éléments optiques sont représentés par des matrices, comme indiqué Figure 9.

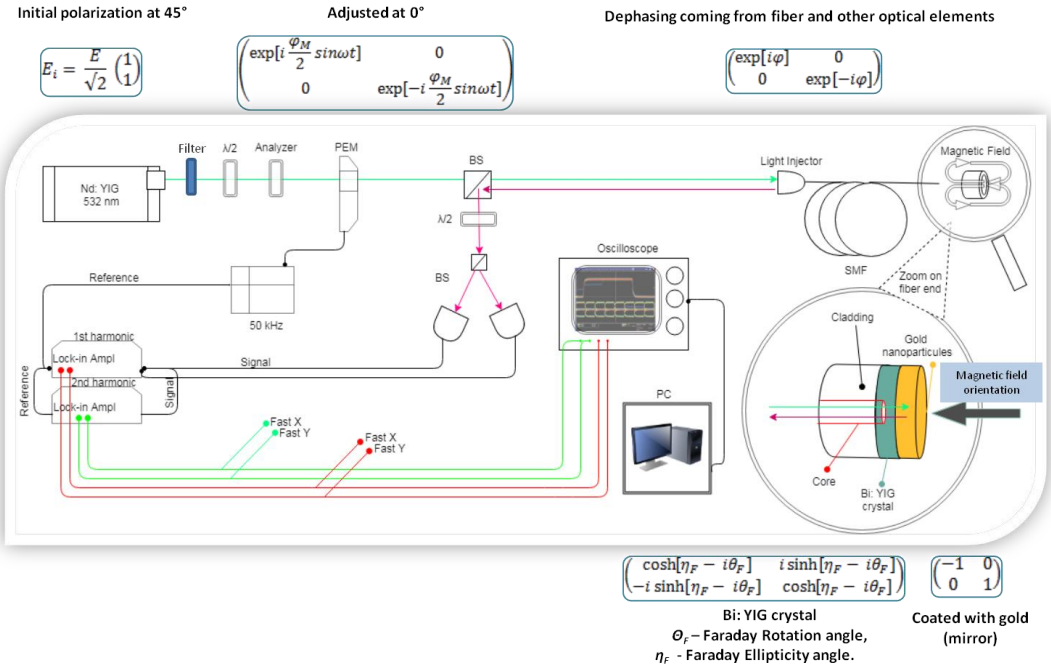

Figure 9: Schéma du capteur de champ magnétique fibré avec indication des matrices de Jones pour chaque élément optique.

Dans la Figure 9, φ_M est l'amplitude du déphasage générée par le PEM, ω est la fréquence de la modulation de la lumière, θ_F est l'angle de la rotation de Faraday, η_F l'angle de l'ellipticité de Faraday et φ est le déphasage dus à la biréfringence de la fibre et d'autres éléments optiques.

A la sortie de la fibre optique, nous effectuons une détection synchrone de l'intensité des polarisations suivant les axes du PEM. Le premier et second harmonique des signaux sont récupérés via deux amplificateurs à détection synchrone. La résolution des équations décrivant le montage conduit à l'angle de rotation de Faraday par l'équation (1)

$$\theta_F = \frac{1}{4}\text{asin}\frac{\sqrt{\Delta I(\omega)^2+\Delta I(2\omega)^2}}{2E_i^2 J_1(\varphi_{12})} \qquad (1)$$

où $J_1(\varphi_{12})$est la fonction de Bessel, $\Delta I(\omega)$ la différence entre les intensités des polarisations verticale et horizontale mesurées à ω, $\Delta I(2\omega)$ la différence entre les intensités des polarisations verticale et horizontale mesurées à 2ω, et E_i^2 la composante continue du signal de sortie. L'ajout des deux intensités de polarisation en ω et en 2ω conduit à l'ellipticité de Faraday, liée au dichroïsme circulaire magnétique et donnée par l'équation (2):

$$\eta_F = \frac{1}{4}\text{asinh}\frac{\sqrt{I_{x+y}(\omega)^2+I_{x+y}(2\omega)^2}}{2E_i^2 J_1(\varphi_{12})} \qquad (2)$$

Il est à noter que les deux expressions dépendent de fonctions sinusoïdales (trigonométriques ou hyperboliques) permettant une sensibilité élevée aux faibles amplitudes du signal. Les autres configurations décrites dans la littérature présentent généralement une réponse en cosinus.

Avec nos matériaux MO, le montage permet la détection de champs magnétiques jusqu'à 1 µT. Notre méthode de production de fibre optique fonctionnalisé nous a permis de synthétiser un microcristal Bi: YIG au bout d'une SMF de 0,5 m avec des épaisseurs de grenat d'environ 200 nm.

Pour la mesure, le champ magnétique à l'extrémité de la fibre optique est modulé à une fréquence arbitraire de 23 Hz pour des amplitudes comprises entre 2 mT et 10 µT. Les résultats sont donnés Figure 10, où la dépendance de rotation Faraday en fonction de la fréquence du champ magnétique (Figure 10 (a)), et la dépendance de la rotation Faraday et l'ellipticité Faraday en fonction de l'amplitude du champ magnétique (Figure 10 (b)) sont indiquées.

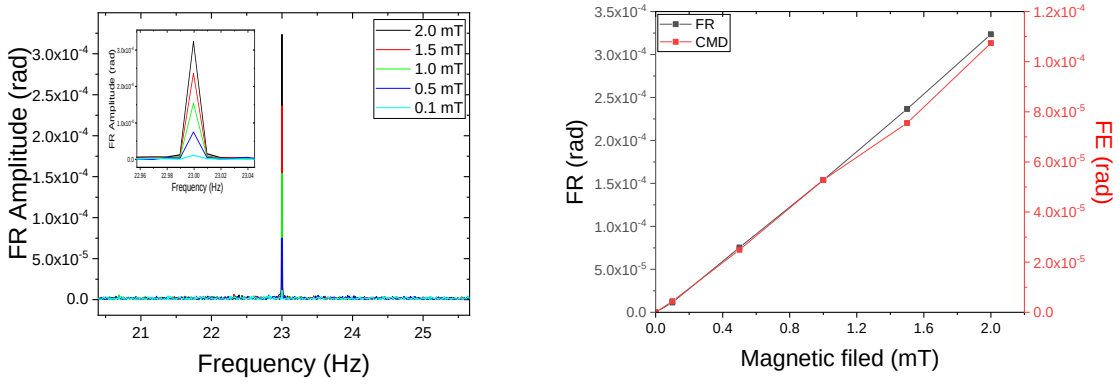

a. b.

Figure 11: (a) Dépendance de rotation de Faraday en fonction de la fréquence modulée du champ magnétique, (b) dépendance de rotation de Faraday et de l'ellipticité de Faraday vs. l'amplitude du champ magnétique.

Conclusion

Actuellement, les objectifs définis au début de mon travail de thèse peuvent être considérés comme atteints. La synthèse du grenat par le procédé MOD a été bien comprise et optimisée. La fonctionnalisation de la fibre est efficace et hautement reproductible. Le fonctionnement d'un capteur magnétique à fibre optique a été démontré avec une taille de la tête de détection limitée à la taille de la fibre optique uniquement.

Pour l'instant, les travaux sont principalement consacrés à l'amélioration du système de détection. Dans le cadre d'un nouveau contrat ATTRACT / CERN / H2020, nous envisageons la préparation d'autres phases grenat ou d'un polymère dopé avec des nanoparticules de magnétite pouvant présenter une sensibilité plus élevée dans le NIR permettant d'utiliser des éléments courant développés pour les télécom. De nouveaux développements prenant en compte les propriétés MO de polymères conjugués sont également à l'étude. Ces matériaux présentent de très importants effets Faraday et peuvent également être considérés pour la fonctionnalisation de fibres optique. Nous espérons que ces travaux aideront à définir l'origine de la réponse de MO qui n'est pas encore clairement comprise dans ces polymères.

Bibliography

[1] Sohlstrom, H. B., & Svantesson, K. G., «Waveguide-based fiber optic magnetic field sensor with directional sensitivity,» *Fiber Optic Sensors: Engineering and Applications,* vol. 1511, pp. 142-149, August 1991.

[2] Rehspringer, J. L., Bursik, J., Niznansky, D., & Klarikova, A., "Characterisation of bismuth-doped yttrium iron garnet layers prepared by sol–gel process," *Journal of magnetism and magnetic materials,* vol. 211, no. 1-3, pp. 291-295, 2000.

[3] Deb, M., Vomir, M., Rehspringer, J. L., & Bigot, J. Y., "Ultrafast optical control of magnetization dynamics in polycrystalline bismuth doped iron garnet thin films," *Applied Physics Letters,* vol. 107, no. 25, p. 252404, 2015.

[4] C. Gauss, "Die Intensität der erdmagnetischen Kraft, zurückgeführt auf absolutes Maass," *Annalen der Physik,* vol. 104, no. 6, pp. 241-273, 1833.

[5] E. Tiberg, "Om magnetiska mätningar vid jernmalmfält medelst den magnetiska inklinationsvågen," *Jernkontorets Annaler,* vol. 39, pp. 29-66, 1884.

[6] A. B. EDGE, "Geophysical methods of prospecting," *Journal of the Royal Society of Arts,* vol. 80, no. 4144, pp. 553-579, 1932.

[7] Shaw, H., Bruckshaw, J. M., & Newing, S. T., "A Brief Survey of the Development of Apparatus and Methods Employed in the Investigation of Subterranean Structural Conditions and the Location of Mineral Deposits," *Applied Geophysics,* 1932.

[8] C. E. J. Delzenne, "Notices elementaire sur les phenomenes d'induction," *Memoires de la societe royale des sciences, de l'agriculture et des arts de Lilles,* vol. 23, pp. 1-132, 1844.

[9] L. S. E. &. S. A. Beck, "Vehicle wheel anti-skid or anti brake-lock system". Washington, DC Patent U.S. Patent No. 4468740, 25 Aug 1984.

[10] Breschi, E., Grujić, Z. D., Knowles, P., & Weis, A., "A high-sensitivity push-pull magnetometer," *Applied Physics Letters,* vol. 104, no. 2, p. 023501, 2014.

[11] A. G. Bell, "Sur un appareil permettant de déterminer, sans douleur pour le patient, la position d'un projectile de plomb ou d'autre métal dans le corps humain," *Gauthier-Villars,* 1881.

[12] Ripka, P., Primdahl, F., Nielsen, O. V., Petersen, J. R., & Ranta, A., "Ac magnetic-field measurement using the fluxgate," *Sensors and Actuators A: Physical,* vol. 46, no. 1-3, pp. 307-311, 1995.

[13] Rabi, I. I., Millman, S., Kusch, P., & Zacharias, J. R., "The molecular beam resonance method for measuring nuclear magnetic moments. the magnetic moments of li 6 3, li 7 3 and f 19 9,"

Physical review, vol. 55, no. 6, p. 526, 1939.

[14] R. H. Varian, "Method and means for correlating nuclear properties of atoms and magnetic fields". Washington, DC Patent U.S. Patent No: 2561490, 24 Jul 1951.

[15] Bell, W. E., Bloom, A. L., "Optical detection of magnetic resonance in alkali metal vapor," *Physical Review,* vol. 107, no. 6, p. 1559, 1957.

[16] Baibich, M. N., Broto, J. M., Fert, A., Van Dau, F. N., Petroff, F., Etienne, P., ... & Chazelas, J., "Giant magnetoresistance of (001) Fe/(001) Cr magnetic superlattices," *Physical review letters,* vol. 61, no. 21, p. 2472, 1988.

[17] R. S. K'doah, "Gravity Probe B: Exploring Einstein's Universe with Gyroscopes," *NASA,* p. 26, 2004.

[18] Cole, J. H., Lagakos, N., Jarzynski, J., & Bucaro, J. A., "Magneto-optic coupling coefficient for fiber interferometric sensors," *Optics letters,* vol. 6, no. 5, pp. 216-218, 1981.

[19] Yariv, A., & Winsor, H. V., "Proposal for detection of magnetic fields through magnetostrictive perturbation of optical fibers," *Optics Letters,* vol. 5, no. 3, pp. 87-89, 1980.

[20] Dandridge, A., Tveten, A. B., Sigel, G. H., West, E. J., & Giallorenzi, T. G., "Optical fibre magnetic field sensors.," *Electronics Letters,* vol. 16, no. 11, pp. 408-409, 1980.

[21] Koo, K. P., & Sigel, G. H., "Characteristics of fiber-optic magnetic-field sensors employing metallic glasses," *Optics letters,* vol. 7, no. 7, pp. 34-336, 1982.

[22] Jarzynski, J., Cole, J. H., Bucaro, J. A., & Davis, C. M., "Magnetic field sensitivity of an optical fiber with magnetostrictive jacket," *Applied optics,* vol. 19, no. 22, pp. 3746-3748, 1980.

[23] Sedlar, M., Paulicka, I., & Sayer, M., "Optical fiber magnetic field sensors with ceramic magnetostrictive jackets," *Applied optics,* vol. 35, no. 27, pp. 5340-5344, 1996.

[24] Mora, J., Diez, A., Cruz, J. L., & Andres, M. V., "A magnetostrictive sensor interrogated by fiber gratings for DC-current and temperature discrimination," *IEEE Photonics Technology Letters,* vol. 12, no. 12, pp. 1680-1682, 2000.

[25] Quintero, S. M., Martelli, C., Braga, A., Valente, L. C., & Kato, C. C., "Magnetic field measurements based on terfenol coated photonic crystal fibers," *Sensors,* vol. 11, no. 12, pp. 11103-11111, 2011.

[26] Reilly, D., Willshire, A. J., Fusiek, G., Niewczas, P., & McDonald, J. R., "A fiber-Bragg-grating-based sensor for simultaneous AC current and temperature measurement.," *IEEE Sensors Journal,* vol. 6, no. 6, pp. 1539-1542, 2006.

[27] Yang, M., Dai, J., Zhou, C., & Jiang, D., "Optical fiber magnetic field sensors with TbDyFe magnetostrictive thin films as sensing materials," *Optics express,* vol. 17, no. 23, pp. 20777-20782, 2009.

[28] Yang, S. Y., Chiu, Y. P., Jeang, B. Y., Horng, H. E., Hong, C. Y., & Yang, H. C., "Origin of field-dependent optical transmission of magnetic fluid films," *Applied Physics Letters,* vol. 19, no. 15, pp. 2372-2374, 2001.

[29] Hu, T., Zhao, Y., Li, X., Chen, J., & Lv, Z., "Novel optical fiber current sensor based on magnetic fluid," *Chinese Optics Letters,* vol. 8, no. 4, pp. 392-394, 2010.

[30] Zhao, Y., Lv, R. Q., Ying, Y., & Wang, Q., "Hollow-core photonic crystal fiber Fabry–Perot sensor for magnetic field measurement based on magnetic fluid," *Optics & Laser Technology,* vol. 44, no. 4, pp. 899-902, 2012.

[31] T. T. G. &. I. Y. Sato, "Method and apparatus for optically measuring a current". Washington, DC Patent U.S. Patent No. 4564754, 14 Jan 1986.

[32] Ning, Y. N., Chu, B. C. B., & Jackson, D. A., "Miniature Faraday current sensor based on multiple critical angle reflections in a bulk-optic ring," *Optics letters,* vol. 16, no. 24, pp. 1996-1998, 1991.

[33] Wang, M., Zhao, J., Liu, S., Liu, F., Wan, X., & Zhang, P., "Optical current sensor immune to reflection phase shift based on graded-index magneto-optical glass," *Applied optics,* vol. 48, no. 32, pp. 6264-6270, 2009.

[34] Sohlström, H., Holm, U., & Svantesson, K., "A polarization based fibre optical sensor system using a YIG optical waveguide for magnetic field sensing," *The 6th International Conference, OFS'89, Paris, France (Springer-Verlag),* vol. 44, pp. 273-278, 1989.

[35] Svantesson, K. G., Sohlstrom, H. B., & Holm, U., "Magneto-optical garnet materials in fiber optic sensor systems for magnetic field sensing," *Electro-Optic and Magneto-Optic Materials II (International Society for Optics and Photonics),* vol. 1274, pp. 260-269, 1990.

[36] Massey G. A., Erickson D. C., Kadlec R. A., "Electromagnetic field components: their measurement using linear electrooptic and magnetooptic effects," *Applied Optics,* vol. 14, no. 11, pp. 2712-2719, 1975.

[37] Bergh, R. A., Lefevre, H. C., & Shaw, H. J., "All-single-mode fiber-optic gyroscope," *Optics letters,* vol. 6, no. 4, pp. 198-200, 1981.

[38] Blake, J., Tantaswadi, P., & De Carvalho, R. T., "In-line Sagnac interferometer current sensor," *IEEE Transactions on Power Delivery,* vol. 11, no. 1, pp. 116-121, 1996.

[39] Kurosawa, K., Yoshida, S., & Sakamoto, K., "Polarization maintaining properties of the flint glass fiber for the Faraday sensor element," *Tenth International Conference on Optical Fibre Sensors (International Society for Optics and Photonics.),* vol. 2360, pp. 28-31, 1994.

[40] Yamashita, T., Watabe, A., Masuda, I., Sakamoto, K., Kurosawa, K., & Yoshida, S., "Extremely small stress-optic coefficient glass single mode fibers for current sensor," *Optical Fiber Sensors (Optical Society of America),* p. We24, 1996.

[41] K. Kurosawa, "Optical current transducers using flint glass fiber as the Faraday sensor element," *Optical Review,* vol. 4, no. 1, p. A38, 1997.

[42] Hotate, K., Thai, B. T., & Saida, T., "Comparison between flint glass fiber and twisted/bent single-mode fiber as a Faraday element in an interferometric fiber optic current sensor," *European Workshop on Optical Fibre Sensors (International Society for Optics and Photonics),* vol. 3483, pp. 233-237, 1998.

[43] Barczak, K., Pustelny, T., Dorosz, D., & Dorosz, J., "New optical glasses with high refractive indices for applications in optical current sensors," *Acta Physica Polonica A,* vol. 116, no. 3, pp. 247-249, 2009.

[44] Sun, L., Jiang, S., Zuegel, J. D., & Marciante, J. R., "Effective Verdet constant in a terbium-doped-core phosphate fiber," *Optics letters,* vol. 34, no. 11, pp. 1699-1701, 2009.

[45] Sun, L., Jiang, S., & Marciante, J. R., "Compact all-fiber optical Faraday components using 65-wt%-terbium–doped fiber with a record Verdet constant of− 32 rad/(Tm)," *Optics express,* vol. 18, no. 12, pp. 12191-12196, 2010.

[46] Yasuhara, R., Tokita, S., Kawanaka, J., Kawashima, T., Kan, H., Yagi, H., ... & Nakatsuka, M., "Cryogenic temperature characteristics of Verdet constant on terbium gallium garnet ceramics," *Optics express,* vol. 15, no. 18, pp. 11255-11261, 2007.

[47] Tang, D., Rose, A. H., Day, G. W., & Etzel, S. M., "Annealing of linear birefringence in single-mode fiber coils: application to optical fiber current sensors," *Journal of Lightwave Technology,* vol. 9, no. 8, pp. 1031-1037, 1991.

[48] Drexler, P., & Fiala, P., "Utilization of Faraday Mirror in Fiber Optic Current Sensors," *Radioengineering,* vol. 17, no. 4, 2008.

[49] Amirsolaimani, B., Gangopadhyay, P., Persoons, A. P., Showghi, S. A., LaComb, L. J., Norwood, R. A., & Peyghambarian, N., "High sensitivity magnetometer using nanocomposite polymers with large magneto-optic response," *Optics letters,* vol. 43, no. 19, pp. 4615-4618, 2018.

[50] K. Shinagawa, " Faraday effect of magnetic garnets," *J. Magn. Soc. Jpn.,* vol. 6, pp. 247-252, 1982.

[51] Zvezdin, A. K., & Kotov, V. A., "Modern magnetooptics and magnetooptical materials," 1997.

[52] Cho, J., Gomi, M., & Abe, M., "Ferromagnetic (LaSr) MnO3 films deposited by RF sputtering," *Japanese journal of applied physics,* vol. 29, no. 9R, p. 1686, 1990.

[53] Martens, J. W. D., & Peeters, W. L., "Interference Enhanced Magneto Optic Kerr Rotation Of Thin Cobalt Ferrite Films," *Optical Storage Media (International Society for Optics and Photonics.),* vol. 420, pp. 231-235, 1983.

[54] Nakamura, H., Ohmi, F., Kaneko, Y., Sawada, Y., Watada, A., & Machida, H., "Cobalt-titanium substituted barium ferrite films for magneto-optical memory," *Journal of Applied Physics,* vol.

61, no. 8, pp. 3346-3348, 1987.

[55] Kurtzig, A. J., Wolfe, R., LeCraw, R. C., & Nielsen, J. W., "Magneto-optical properties of a green room-temperature ferromagnet: FeBO3," *Applied Physics Letters,* vol. 14, no. 11, pp. 350-352, 1969.

[56] Kurtzig, A. J., & Guggenheim, H. J., "Magneto-optical properties of a green room-temperature ferromagnet FeF3," *Applied Physics Letters,* vol. 16, no. 1, pp. 43-45, 1970.

[57] Ahrenkiel, R. K., Moser, F., Carnall, E., Martin, T., Pearlman, D., Lyu, S. L., ... & Lee, T. H., "Hot-Pressed CdCr2S4: an efficient magneto-optic material," *Applied Physics Letters,* vol. 18, no. 5, pp. 171-173, 1971.

[58] Dillon Jr, J. F., Kamimura, H., & Remeika, J. P., "Magneto-optical properties of ferromagnetic chromium trihalides," *Journal of Physics and Chemistry of Solids,* vol. 27, no. 9, pp. 1531-1549, 1966.

[59] Wang, H. Y., Schoenes, J., & Kaldis, E., "Magnetooptical Polar Kerr Effect of EuO," *HELVETICA PHYSICA ACTA,* vol. 59, no. 1, pp. 102-105, 1986.

[60] Chen, Z., Yang, L., Hang, Y., & Wang, X., " Improving characteristic of Faraday effect based on the Tm3+ doped terbium gallium garnet single crystal," *Journal of Alloys and Compounds,* vol. 661, pp. 62-65, 2016.

[61] Popma, T. J. A., & Kamminga, M. G. J., "The polar magneto-optic Kerr rotation of ferromagnetic perovskites (La, Bi, Sr) MnO3," *Solid State Communications,* vol. 17, no. 9, pp. 1073-1075, 1975.

[62] Hwang, H. J., Towata, A., & Awano, M., "Fabrication of Lanthanum Manganese Oxide Thin Films on Yttria-Stabilized Zirconia Substrates by a Chemically Modified Alkoxide Method," *Journal of the American Ceramic Society,* vol. 84, no. 10, pp. 2323-2327, 2001.

[63] Andrews, K., & Kaye, A. B., "Optimized procedure for sol–gel production of La 2/3 Ca 1/3 MnO 3 thin films.," *Journal of Sol-Gel Science and Technology,* vol. 76, no. 2, pp. 372-377, 2015.

[64] Kim, G. W., Kumar, S., Chang, J., Lee, C. G., & Koo, B. H., "Magnetic and electrical properties of La0. 7Ca0. 3Mn0. 95Co0. 05O3 epitaxial layers by pulsed laser deposition," *Ceramics International,* vol. 38, pp. S443-S446, 2012.

[65] B. X. Gu, "Magnetic properties and magneto-optical effect of Co 0.5 Fe 2.5 O 4 nanostructured films," *Applied physics letters,* vol. 82, no. 21, pp. 3707-3709, 2003.

[66] Wu, C., Yu, Z., Sun, K., Nie, J., Guo, R., Liu, H., ... & Lan, Z., "Calculation of exchange integrals and Curie temperature for La-substituted barium hexaferrites," vol. 6, no. 36200, 2016.

[67] J. M. D. Coey, "Amorphous magnetic order," *Journal of Applied Physics,* vol. 49, no. 3, pp. 1646-1652, 1978.

[68] Masterson, H. J., Lunney, J. G., Coey, J. M. D., Atkinson, R., Salter, I. W., & Papakonstantinou, P., "hin films of barium ferrite with perpendicular magnetic anisotropy produced by laser ablation deposition," *Journal of applied physics,* vol. 73, no. 8, pp. 3917-3921, 1993.

[69] Zanmarchi, G., & Bongers, P. F., "Infrared faraday rotation in ferrites," *Journal of Applied Physics,* vol. 40, no. 3, pp. 1230-1231, 1969.

[70] Sherwood, R. C., Remeika, J. P., & Williams, H. J., "Domain behavior in some transparent magnetic oxides," *Journal of Applied Physics,* vol. 30, no. 2, pp. 217-225, 1959.

[71] Shono, K., Gomi, M., & Abe, M., "Magneto-Optical Properties of Magnetoplumbites BaFe12O19, SrFe12-xAlxO19 and PbFe12O19," *Japanese Journal of Applied Physics,* vol. 21, no. 10R, p. 1451, 1982.

[72] Teh, G. B., Saravanan, N., & Jefferson, D. A., "A study of magnetoplumbite-type (M-type) cobalt–titanium-substituted barium ferrite, BaCoxTixFe12− 2xO19 (x= 1–6)," *Materials Chemistry and Physics,* vol. 105, no. 2-3, pp. 253-259, 2007.

[73] Pang, C., Gao, L., Singh, A. V., Chen, H., Bowman, M. K., Bao, N., ... & Gupta, A., "Synthesis, Formation Mechanism, and Magnetic Properties of Monodisperse Semiconducting Spinel CdCr2S4 Nanocrystals via a Facile “Seed-Mediated” Growth Method," *Chemistry of Materials,* vol. 30, no. 5, pp. 1701-1709, 2018.

[74] Moser, F., Ahrenkiel, R. K., Carnall, E., Coburn, T., Lyu, S. L., Lee, T. H., ... & Pearlman, D., "Optical and Magneto-Optic Properties of Polycrystalline CdCr2S4," *Journal of Applied Physics,* vol. 42, no. 4, pp. 1449-1451, 1971.

[75] Yan, L. Q., Shen, J., Li, Y. X., Wang, F. W., Jiang, Z. W., Hu, F. X., ... & Shen, B. G., "Large magnetocaloric effect in spinel Cd Cr 2 S 4," *Applied physics letters,* vol. 90, no. 26, p. 262502, 2007.

[76] Kalashnikova, A. M., Kimel, A. V., Pisarev, R. V., Gridnev, V. N., Usachev, P. A., Kirilyuk, A., & Rasing, T., "Impulsive excitation of coherent magnons and phonons by subpicosecond laser pulses in the weak ferromagnet FeBO 3," *Physical Review B,* vol. 78, no. 10, p. 104301, 2008.

[77] Wolfe, R., Kurtzig, A. J., & LeCraw, R. C, "Room-Temperature Ferromagnetic Materials Transparent in the Visible," *Journal of Applied Physics,* vol. 41, no. 3, pp. 1218-1224, 1970.

[78] Kotrbova, M., Kadečková, S., Novak, J., Bradler, J., Smirnov, G. V., & Shvydko, Y. V., "Growth and perfection of flux grown FeBO3 and 57FeBO3 crystals," *Journal of crystal growth,* vol. 71, no. 3, pp. 607-614, 1985.

[79] Joubert, J. C., Shirk, T., White, W. B., & Roy, R., "Stability, infrared spectrum and magnetic properties of FeBO3," *Materials Research Bulletin,* vol. 3, no. 8, pp. 671-676, 1968.

[80] Muller, O., O'Horo, M. P., & O'Neill, J. F., "FeBO3 solid solutions: Synthesis, crystal chemistry, and magnetic properties," *Journal of Solid State Chemistry,* vol. 23, no. 1-2, pp. 115-128, 1978.

[81] Webster, L., & Yan, J. A., "Strain-tunable magnetic anisotropy in monolayer CrCl 3, CrBr 3, and CrI 3," *Physical Review B,* vol. 98, no. 14, p. 144411, 2018.

[82] Kim, H. H., Yang, B., Li, S., Jiang, S., Jin, C., Tao, Z., ... & Tian, S., "Evolution of interlayer and intralayer magnetism in three atomically thin chromium trihalides," *Proceedings of the National Academy of Sciences,* vol. 116, no. 23, pp. 11131-11136, 2019.

[83] I. Schoenes, "Lanthanide and actinide compounds with record magneto-optical effects," *Journal of the Magnetics Society of Japan,* vol. 11, no. S_1_ISMO, pp. 99-105, 1987.

[84] M. W. Shafer, "Preparation and crystal chemistry of divalent europium compounds," *Journal of Applied Physics,* vol. 36, no. 3, pp. 1145-1152, 1965.

[85] Dentz, D. J., Puttbach, R. C., & Belt, R. F. , "Terbium gallium garnet for Faraday effect," *AIP Conference Proceedings,* vol. 18, no. 1, pp. 954-958, 1974.

[86] Villaverde, A. B., Donatti, D. A., & Bozinis, D. G., "Terbium gallium garnet Verdet constant measurements with pulsed magnetic field," *Journal of Physics C: Solid State Physics,* vol. 11, no. 12, p. L495, 1978.

[87] Yasuhara, R., Snetkov, I., Starobor, A., Zheleznov, D., Palashov, O., Khazanov, E., ... & Yanagitani, T., "Terbium gallium garnet ceramic Faraday rotator for high-power laser application," *Optics letters,* vol. 39, no. 5, pp. 1145-1148, 2014.

[88] Chen, Z., Yang, L., Hang, Y., & Wang, X., "Faraday effect improvement by Dy3+-doping of terbium gallium garnet single crystal," *Journal of Solid State Chemistry,* vol. 233, pp. 277-281, 2016.

[89] Vojna, D., Slezák, O., Lucianetti, A., & Mocek, T., "Verdet Constant of Magneto-Active Materials Developed for High-Power Faraday Devices," *Applied Sciences,* vol. 9, no. 15, p. 3160, 2019.

[90] Yasuhara, R., Tokita, S., Kawanaka, J., Kawashima, T., Kan, H., Yagi, H., ... & Nakatsuka, M., "Cryogenic temperature characteristics of Verdet constant on terbium gallium garnet ceramics," *Optics express,* vol. 15, no. 18, pp. 11255-11261, 2007.

[91] Kekesi, R., Royer, F., Jamon, D., Mignon, M. B., Abou-Diwan, E., Chatelon, J. P., ... & Tombacz, E., " 3D magneto-photonic crystal made with cobalt ferrite nanoparticles silica composite structured as inverse opal.," *Optical Materials Express,* vol. 3, no. 7, pp. 935-947, 2013.

[92] Gangopadhyay, P., Foerier, S., Koeckelberghs, G., Vangheluwe, M., Persoons, A., & Verbiest, T. , "Efficient Faraday rotation in conjugated polymers," *Proc. SPIE,* vol. 6331, p. 63310Z, 2006.

[93] Belotelov, V. I., Akimov, I. A., Pohl, M., Kotov, V. A., Kasture, S., Vengurlekar, A. S., ... & Bayer, M., " Enhanced magneto-optical effects in magnetoplasmonic crystals," *Nature Nanotechnology,* vol. 6, no. 6, p. 370, 2011.

[94] Floess, D., Hentschel, M., Weiss, T., Habermeier, H. U., Jiao, J., Tikhodeev, S. G., & Giessen, H., "Plasmonic analog of electromagnetically induced absorption leads to giant thin film Faraday rotation of 14°," *Physical Review X,* vol. 7, no. 2, p. 021048, 2017.

[95] Zhou, X., Zhang, K. H., Xiong, J., Park, J. H., Dickerson, J. H., & He, W., "Size-and dimensionality-dependent optical, magnetic and magneto-optical properties of binary europium-based nanocrystals: EuX (X= O, S, Se, Te)," *Nanotechnology,* vol. 27, no. 19, p. 192001, 2016.

[96] Y. Hasegawa, "Magnetic semiconductor EuO, EuS, and EuSe nanocrystals for future optical devices," *Chemistry Letters,* vol. 42, no. 1, pp. 2-7, 2012.

[97] Tsukahara, Y., Kataoka, T., Hasegawa, Y., Kaizaki, S., & Wada, Y., "The first observation of the magnetic circular dichroism in EuS nanocrystals," *Journal of alloys and compounds,* vol. 408, pp. 203-206, 2006.

[98] Thongchant, S., Hasegawa, Y., Tanaka, K., Fujita, K., Hirao, K., Wada, Y., & Yanagida, S., "First observation of Faraday effect of EuS nanocrystals in polymer thin film," *Japanese journal of applied physics,* vol. 42, no. 7B, p. L876, 2003.

[99] Kataoka, T., Tsukahara, Y., Hasegawa, Y., & Wada, Y., "Size-controlled synthesis of quantum-sized EuS nanoparticles and tuning of their Faraday rotation peak," *Chemical Communications,* no. 48, pp. 6038-6040, 2005.

[100] Kawashima, A., Nakanishi, T., Kitagawa, Y., Fushimi, K., & Hasegawa, Y. , "Photoswitchable faraday effect in EuS–Au nanosystems," *physica status solidi (a),* vol. 213, no. 1, pp. 178-182, 2016.

[101] Jung, J. S., Lim, J. H., Choi, K. H., Oh, S. L., Kim, Y. R., Lee, S. H., ... & O'Connor, C. J., "Co Fe 2 O 4 nanostructures with high coercivity," *Journal of Applied Physics,* vol. 97, no. 10, p. 10f306, 2005.

[102] Royer, F., Jamon, D., Rousseau, J. J., Zins, D., Cabuil, V., Neveu, S., & Roux, H., "Magneto-optical properties of CoFe 2 O 4 ferrofluids. Influence of the nanoparticle size distribution," *Trends in Colloid and Interface Science XVII - Springer, Berlin, Heidelberg.,* pp. 155-158, 2004.

[103] Miles, A., Gai, Y., Gangopadhyay, P., Wang, X., Norwood, R. A., & Watkins, J. J., "Improving Faraday rotation performance with block copolymer and FePt nanoparticle magneto-optical composite," *Optical Materials Express,* vol. 7, no. 6, pp. 2126-2140, 2017.

[104] Demir, V., Gangopadhyay, P., Norwood, R. A., & Peyghambarian, N. , "Faraday rotation of cobalt ferrite nanoparticle polymer composite films at cryogenic temperatures," *pplied optics,* vol. 53, no. 10, pp. 2087-2092, 2014.

[105] Lopez-Santiago, A., Grant, H. R., Gangopadhyay, P., Voorakaranam, R., Norwood, R. A., & Peyghambarian, N, "Cobalt ferrite nanoparticles polymer composites based all-optical magnetometer," *Optical Materials Express,* vol. 2, no. 7, pp. 978-986, 2012.

[106] Zamani, M., & Hocini, A., "Large Faraday rotation in magnetophotonic crystals containing SiO2/ZrO2 matrix doped with CoFe2O4 magnetic nanoparticles," *Optical Materials,* vol. 58, pp.

306-309, 2016.

[107] Jain, P. K., Xiao, Y., Walsworth, R., & Cohen, A. E., " Surface plasmon resonance enhanced magneto-optics (SuPREMO): Faraday rotation enhancement in gold-coated iron oxide nanocrystals," *Nano letters,* vol. 9, no. 4, pp. 1644-1650, 2009.

[108] Chin, J. Y., Steinle, T., Wehlus, T., Dregely, D., Weiss, T., Belotelov, V. I., ... & Giessen, H. , "Nonreciprocal plasmonics enables giant enhancement of thin-film Faraday rotation," *Nature communications,* vol. 4, p. 1599, 2013.

[109] Araoka, F., Abe, M., Yamamoto, T., & Takezoe, H., "Large Faraday rotation in a π-conjugated poly (arylene ethynylene) thin film," *Applied physics express,* vol. 2, no. 1, p. 011501, 2009.

[110] Peyghambarian, N., Norwood, R. A., & Persoons, A., "In-Fiber Magneto-Optic Devices Based on Ultrahigh Verdet Constant Organic Materials and Holey Fibers," *ARIZONA UNIV BOARD OF REGENTS TUCSON,* 2009.

[111] Gangopadhyay, P., Voorakaranam, R., Lopez-Santiago, A., Foerier, S., Thomas, J., Norwood, R. A., ... & Peyghambarian, N., "Faraday rotation measurements on thin films of regioregular alkyl-substituted polythiophene derivatives," *The Journal of Physical Chemistry C,* vol. 112, no. 21, pp. 8032-8037, 2008.

[112] Wang, P., Jeon, I., Lin, Z., Peeks, M. D., Savagatrup, S., Kooi, S. E., ... & Swager, T. M., "Insights into magneto-optics of helical conjugated polymers," *Journal of the American Chemical Society,* vol. 140, no. 20, pp. 6501-6508, 2018.

[113] Serga, A. A., Chumak, A. V., & Hillebrands, B., "YIG magnonics," *Journal of Physics D: Applied Physics,* vol. 43, no. 26, p. 264002, 2010.

[114] Stadler, B. J., & Hutchings, D. C., "Sputter-deposited magneto-optical garnet for all-mode (transverse electric/transverse magnetic) Faraday rotators," *MRS Bulletin,* vol. 43, no. 6, pp. 430-435, 2018.

[115] Wolfe, R., Hegarty, J., Dillon, J., Luther, L., Celler, G., & Trimble, L., "Magneto-optic waveguide isolators based on laser annealed (Bi, Ga) YIG films," *IEEE Transactions on Magnetics,* vol. 21, no. 5, pp. 1647-1650, 1985.

[116] Ghosh, S., Keyvavinia, S., Van Roy, W., Mizumoto, T., Roelkens, G., & Baets, R., "Ce: YIG/Silicon-on-Insulator waveguide optical isolator realized by adhesive bonding," *Optics express,* vol. 20, no. 2, pp. 1839-1848, 2012.

[117] C. F. Buhrer, "Wideband temperature-compensated optical isolator or circulator configuration using two Faraday elements," *Optics letters,* vol. 14, no. 21, pp. 1180-1182, 1989.

[118] Kamada, O., & Higuchi, S., "Magnetic field sensors using Ce: YIG single crystals as a Faraday element," *IEEE Transactions on magnetics,* vol. 37, no. 4, pp. 2013-2015, 2001.

[119] Kamada, O., Nakaya, T., & Higuchi, S., "Magnetic field optical sensors using Ce: YIG single crystals as a Faraday element," *Sensors and Actuators A: Physical,* vol. 119, no. 2, pp. 345-348,

2005.

[120] Galstyan, O., Lee, H., Babajanyan, A., Hakhoumian, A., Friedman, B., & Lee, K., "Magneto-optical visualization by Bi: YIG thin films prepared at low temperatures," *Journal of Applied Physics,* vol. 117, no. 16, p. 163914, 2015.

[121] J. F. Dillon Jr, " Observation of domains in the ferrimagnetic garnets by transmitted light," *Journal of Applied Physics,* vol. 29, no. 9, pp. 1286-1291, 1958.

[122] Wettling, W., Andlauer, B., Koidl, P., Schneider, J., & Tolksdorf, W., "Optical absorption and Faraday rotation in yttrium iron garnet," *Physica status solidi (b),* vol. 59, no. 1, pp. 63-70, 1973.

[123] Tobita, E., Shinagawa, K., Saito, T., & Tsushima, T., "Faraday effects in Rh4+-and Ir4+-substituted magnetic garnets," *Journal of the Magnetics Society of Japan,* vol. 20, no. S_1_MORIS_96, pp. S1_439-444, 1996.

[124] Gomi, M., Satoh, K., & Abe, M., "Giant Faraday rotation of Ce-substituted YIG films epitaxially grown by RF sputtering," *Japanese journal of applied physics,* vol. 27, no. 8A, p. L1536, 1988.

[125] Dillon Jr, J. F., Albiston, S. D., & Fratello, V. J., "Magnetooptical rotation of PrIG and NdIG," *Journal of the Magnetics Society of Japan,* vol. 11, no. S_1_ISMO, pp. S1_241-244, 1987.

[126] Lage, E., Beran, L., Quindeau, A. U., Ohnoutek, L., Kucera, M., Antos, R., ... & Ross, C. A., "Temperature-dependent Faraday rotation and magnetization reorientation in cerium-substituted yttrium iron garnet thin films," *APL Materials,* vol. 5, no. 3, p. 036104, 2017.

[127] Wittekoek, S., Popma, T. J., Robertson, J. M., & Bongers, P. F., "Magneto-optic spectra and the dielectric tensor elements of bismuth-substituted iron garnets at photon energies between 2.2-5.2 eV," *Physical review B,* vol. 12, no. 7, p. 2777, 1975.

[128] Hansen, P., Witter, K., & Tolksdorf, W., "Magnetic and magneto-optic properties of bismuth-and aluminum-substituted iron garnet films," *Journal of applied physics,* vol. 55, no. 4, pp. 1052-1061, 1984.

[129] Hansen, P., Witter, K., & Tolksdorf, W., "Magnetic and magneto-optic properties of lead-and bismuth-substituted yttrium iron garnet films," *Physical Review B,* vol. 27, no. 11, p. 6608, 1983.

[130] Hansen, P., Witter, K., & Tolksdorf, W., "Magnetic and magneto-optical properties of bismuth-substituted gadolinium iron garnet films," *Physical Review B,* vol. 27, no. 7, p. 4375, 1983.

[131] Matsumoto, K., Yamaguchi, K., Ueno, A., & Fujii, T., "Preparation of Bi-substituted YIG garnets by sol-gel synthesis and their magnetic properties," *IEEE Translation Journal on Magnetics in Japan,* vol. 6, no. 1, pp. 15-22, 1991.

[132] Huang, M., & Xu, Z. C., "Liquid phase epitaxy growth of bismuth-substituted yttrium iron garnet thin films for magneto-optical applications," *Thin Solid Films,* vol. 450, no. 2, pp. 324-

328, 2004.

[133] Görnert, P., Aichele, T., Lorenz, A., Hergt, R., & Taubert, J., "Liquid phase epitaxy (LPE) grown Bi, Ga, Al substituted iron garnets with huge Faraday rotation for magneto-optic applications," *physica status solidi (a),* vol. 201, no. 7, pp. 1398-1402, 2004.

[134] Hayashi, H., Iwasa, S., Vasa, N. J., Yoshitake, T., Ueda, K., Yokoyama, S., ... & Nakahara, M., "Fabrication of Bi-doped YIG optical thin film for electric current sensor by pulsed laser deposition," *Applied surface science,* vol. 197, pp. 463-466, 2002.

[135] Popova, E., Deb, M., Bocher, L., Gloter, A., Stéphan, O., Warot-Fonrose, B., ... & Keller, N., "Interplay between epitaxial strain and low dimensionality effects in a ferrimagnetic oxide," *Journal of Applied Physics,* vol. 121, no. 11, p. 115304, 2017.

[136] Gomi, M., Utsugi, K., & Abe, M., "RF sputtered films of Bi-substituted garnet for magneto-optical memory," *IEEE Transactions on Magnetics,* vol. 22, no. 5, pp. 1233-1235, 1986.

[137] Abe, M., & Gomi, M., "Magneto-optical recording on garnet films," *Journal of magnetism and magnetic materials,* vol. 84, no. 3, pp. 222-228, 1990.

[138] Nur-E-Alam, M., Vasiliev, M., & Alameh, K., "High-performance RF-sputtered Bi-substituted iron garnet thin films with almost in-plane magnetization," *Optical Materials Express,* vol. 7, no. 3, pp. 676-686, 2017.

[139] Galstyan, O., Lee, H., Lee, S., Yoo, N., Park, J., Babajanyan, A., ... & Lee, K., "Effect of pre-crystallization on the preparation of thick Bi-YIG films by the metal–organic decomposition method," *Journal of Magnetism and Magnetic Materials,* vol. 366, pp. 24-27, 2014.

[140] Galstyan, O., Lee, H., Babajanyan, A., Hakhoumian, A., Friedman, B., & Lee, K., "Magneto-optical visualization by Bi: YIG thin films prepared at low temperatures," *Journal of Applied Physics,* vol. 117, no. 16, p. 163914, 2015.

[141] Ishibashi, T., Yoshida, T., Kobayashi, T., Ikehara, S., & Nishi, T., "Preparation of Y0. 5Bi2. 5Fe5O12 films on glass substrates using magnetic iron garnet buffer layers by metal-organic decomposition method," *Journal of Applied Physics,* vol. 113, no. 17, p. 17A926, 2013.

[142] R. C. Linares, "Epitaxial growth of narrow linewidth yttrium iron garnet films," *Journal of Crystal Growth,* vol. 3, pp. 443-446, 1968.

[143] Hergt, R., Pfeiffer, H., Görnert, P., Wendt, M., Keszei, B., & Vandlik, J., "Kinetic segregation of lead impurities in garnet LPE films," *Physica status solidi (a),* vol. 104, no. 2, pp. 769-776, 1987.

[144] Dijkkamp, D., Venkatesan, T., Wu, X. D., Shaheen, S. A., Jisrawi, N., Min-Lee, Y. H., ... & Croft, M., "Preparation of Y-Ba-Cu oxide superconductor thin films using pulsed laser evaporation from high T c bulk material," *Applied Physics Letters,* vol. 51, no. 8, pp. 619-621, 1987.

[145] "www.rbnano.com," [Online].

[146] S. N. Mastromatteo, "Development of a Magneto-Optic Spectrometer," Carnegie Mellon University, Pittsburgh, Pennsylvania, 1996.

[147] Wittekoek, S., Popma, T. J., Robertson, J. M., & Bongers, P. F., "Magneto-optic spectra and the dielectric tensor elements of bismuth-substituted iron garnets at photon energies between 2.2-5.2 eV," *Physical review B,* vol. 7, no. 12, p. 2777, 1975.

[148] Ishibashi, T., Mizusawa, A., Nagai, M., Shimizu, S., Sato, K., Togashi, N., ... & Kuriyama, K., "Characterization of epitaxial (Y, Bi) 3 (Fe, Ga) 5 O 12 thin films grown by metal-organic decomposition method," *Journal of applied physics,* vol. 97, no. 1, p. 013516, 2005.

[149] Kojima, N., & Sugano, S., "Magneto-optics," *Springer - Verlag, Berlin, Heidelberg, New York,* vol. ch. 5, pp. 137-177, 2000.

[150] Geller, S., Williams, H. J., Espinosa, G. P., Sherwood, R. C., & Gilleo, M. A., "Reduction of the preparation temperature of polycrystalline garnets by bismuth substitution," *Applied Physics Letters,* vol. 3, no. 2, pp. 21-22, 1963.

[151] Strocka, B., Holst, P., & Tolksdorf, W., "An empirical formula for the calculation of lattice constants of oxide garnets based on substituted yttrium-and gadolinium-iron garnets," *Philips Journal of Research,* vol. 33, pp. 186-202, 1978.

[152] Fu, Y. P., Hung, D. S., Cheng, C. W., Tsai, F. Y., & Yao, Y. D., "Non-isothermal crystallization kinetics and microwave properties of Bi0. 75Y2. 25Fe5O12 prepared by coprecipitation," *Ceramics International,* vol. 35, no. 2, pp. 559-564, 2009.

[153] Fu, Y. P., & Lew, K. K., "Crystallization behavior of Bi1. 25Y1. 75Fe5O12 prepared by coprecipitation process," *Ceramics International,* vol. 35, no. 8, pp. 3235-3239, 2009.

[154] Lux, R., Heinrich, A., Leitenmeier, S., Körner, T., Herbort, M., & Stritzker, B., "Pulsed-laser deposition and growth studies of Bi 3 Fe 5 O 12 thin films," *Journal of applied physics,* vol. 100, no. 11, p. 113511, 2006.

Facsimile of the paper:

"Limits of the magneto-optical properties of Bi: YIG films prepared on silica by metal-organic decomposition"

Ceramics International 45 (2019) 21409–21412

Contents lists available at ScienceDirect

Ceramics International

journal homepage: www.elsevier.com/locate/ceramint

Limits of the magneto-optical properties of Bi: YIG films prepared on silica by metal organic decomposition

Issatay Nadinov*, Oleksandr Kovalenko, Jean-Luc Rehspringer, Mircea Vomir, Loïc Mager

CNRS/IPCMS - Institut de Physique et Chimie des Matériaux de Strasbourg, 23 Rue Du Loess, BP 43, 67034 STRASBOURG CEDEX 2, France

ARTICLE INFO

Keywords:
A. Films
C. Optical properties
B. Thermal properties
E. Sensors

ABSTRACT

Different bismuth-substituted yttrium iron garnet thin films were prepared on silica substrates by metal organic decomposition of propionic salts with varied initial amounts of bismuth, annealing time, and temperature. The magneto-optical properties were monitored continuously during the annealing step, yielding access to the activation energy of the garnet film crystallization. These measurements coupled with X-ray diffraction spectra of the final products show that the magneto-optical properties of the films deposited on silica are limited by the saturation of bismuth substitution and appearance of side products with high initial bismuth contents.

1. Introduction

Bismuth-substituted yttrium/iron garnets (Bi: YIG) have long been recognized as one of the most efficient materials for magneto-optical (MO) applications in the visible/NIR spectral range [1]. They can be grown by different processes such as liquid phase epitaxy [2], pulsed laser deposition [3], sputtering [4], sol-gel [5,6], or the metal organic decomposition (MOD) [7–9] method used in the present work. The MOD process has the advantages of simplicity and low costs as it can be performed under normal atmosphere and does not require heavy preparation devices.

Motivated by the possibility of preparing a Bi: YIG directly on an optical fiber for MO sensing applications, we studied the MOD synthesis process of Bi: YIG films deposited on silica. Seeking maximum performances, we measured the Faraday rotation during the annealing step for different temperatures and initial compositions. By doing so, we determined the activation energies of crystallization and degradation for the garnet films by optical measurements, whereas for calorimetric analysis, the very low contribution of a thin nano-layer is concealed by the response of the substrate. We show that the MO performances for Bi: YIG prepared by MOD on silica are limited by the effective substitution of bismuth, the appearance of side products for high initial concentrations of bismuth, and the progressive degradation of garnet at high temperatures.

2. Experimental procedures

2.1. Preparation of Bi: YIG films

The initial products iron(III) propionate ($Fe(C_3H_5O_2)_3$), yttrium(III) propionate ($Y(C_3H_5O_2)_3$), and bismuth(III) propionate ($Bi(C_3H_5O_2)_3$) were produced by acid-base reaction [10]. They were dissolved in propionic acid according to desired stoichiometries by varying the initial amount of bismuth, x_{ini}, and of yttrium, $3\text{-}x_{ini}$, with a constant amount of iron. The total amount of metal chelates was fixed at 1 M to avoid recrystallisation of the yttrium precursor.

The solutions were spin-coated on 1 cm × 1 cm silica substrates at 2000 rpm for 1 min. Initial drying was followed by 40 min of pyrolysis at 300 °C to eliminate residual organics. Immediately after spin coating, the solution layer was typically 500 nm thick, and after pyrolysis, the thickness decreased to 50 nm. This cycle was repeated 5 times to reach a final 250 nm thickness. Finally, the film was annealed between 640 °C and 740 °C for a duration varying between 4 h and 20 h. All operations were performed in air.

2.2. Characterizations

A 3D optical surface profiler (Zygo NewView 6300) was used to measure the thicknesses of the films, and a UV–Vis–NIR spectrometer (PerkinElmer Lambda 950) was used to acquire optical absorption spectra of the different samples in the 250 nm–800 nm range. The static MO properties were measured using a custom setup via modulation of light polarization [11,12]. In the custom setup, the light provided by a

* Corresponding author.
E-mail address: issatay.nadinov@ipcms.unistra.fr (I. Nadinov).

https://doi.org/10.1016/j.ceramint.2019.07.129
Received 30 April 2019; Received in revised form 9 July 2019; Accepted 11 July 2019
Available online 12 July 2019
0272-8842/ © 2019 The Authors. Published by Elsevier Ltd. This is an open access article under the CC BY-NC-ND license (http://creativecommons.org/licenses/BY-NC-ND/4.0/).

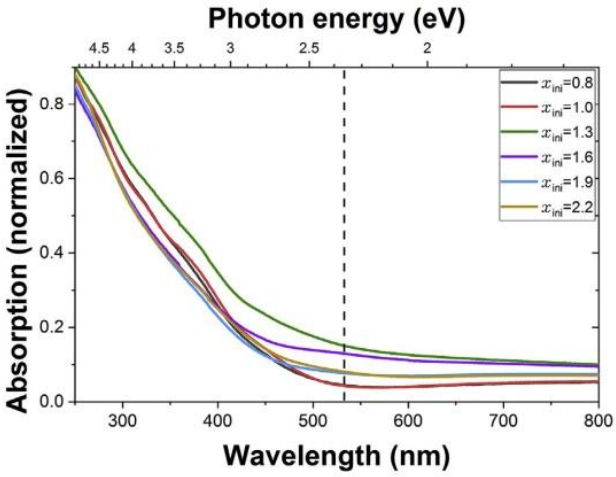

Fig. 1. Optical absorption spectra of Bi: YIG films on silica substrates with different initial amounts of bismuth (x_{ini}) annealed at 700 °C for 1 h.

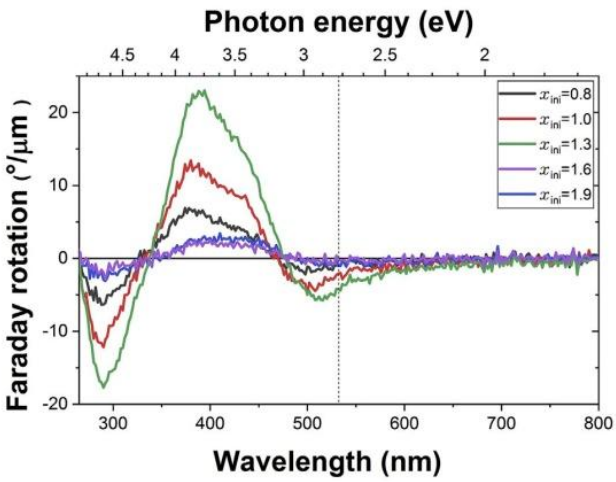

Fig. 2. Faraday rotation spectra at saturation for Bi: YIG films on silica substrates with different x_{ini} annealed at 700 °C for 1 h.

150 W Xe arc lamp is polarized by a Rochon polarizer. Subsequently, a photo-elastic modulator (Hinds PEM-100) modulates the polarization state at a 50 kHz frequency. The beam is then focused on the sample, and the transmitted light is collimated and analyzed by a second Rochon polarizer. The light is then focused on the entrance slit of a monochromator covering the 200 nm–900 nm spectral range. The output light is detected by a photomultiplier connected to a lock-in amplifier (Stanford SR810) for synchronous detection of the second harmonic signal, which is proportional to the polarization rotation. This setup allows for measurement of rotation angles below 1′. The sample is placed in a hot stage (LINKAM Scientific TS1500) that controls the temperature between ambient and 1500 °C at a heating rate of 200 °C/min. The size of the hot plate permits its positioning in the air gap of an electromagnet (GMW Associates 5403), which provides a static magnetic field up to 1 T.

The crystalline phases and lattice parameters of the samples were characterized by X-ray diffractometry (XRD, Bruker D8 Advance) using Cu $K_{\alpha 1}$ radiation (1.54056 Å).

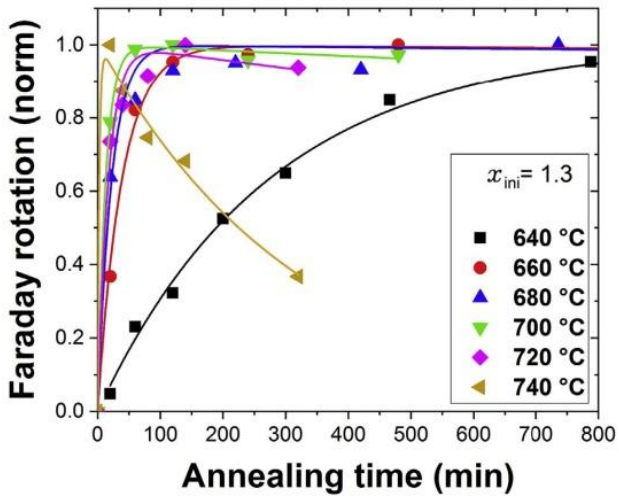

Fig. 4. Time-dependent Faraday rotations for x_{ini} = 1.3 at different annealing temperatures. Lines are fits to the solution of equation (1).

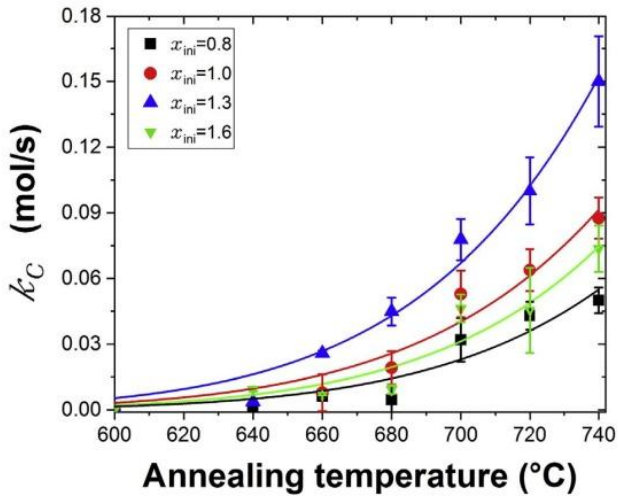

Fig. 5. Variation in crystallization rate with temperature for different x_{ini}. The curves correspond to Arrhenius fittings.

3. Results and discussion

We prepared a first set of samples by varying x_{ini} (amount of

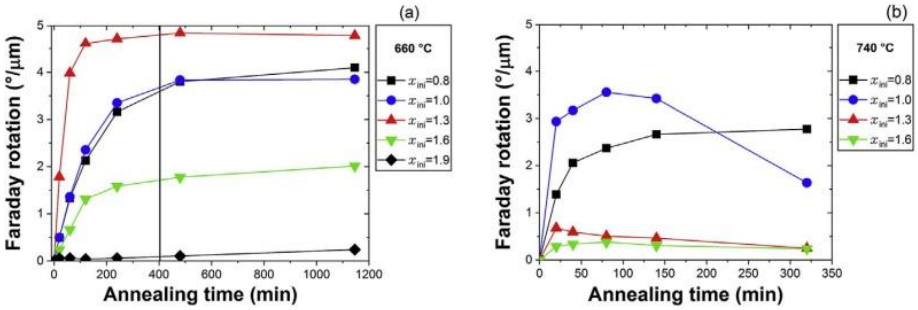

Fig. 3. Evolution of the Faraday rotation at 532 nm with annealing time for different initial amounts of bismuth at (a) 660 °C and (b) 740 °C. Black squares: x_{ini} = 0.8, blue disks: x_{ini} = 1.0, red up triangles: x_{ini} = 1.3, green down triangles: x_{ini} = 1.6, black diamonds: x_{ini} = 1.9. . (For interpretation of the references to colour in this figure legend, the reader is referred to the Web version of this article.)

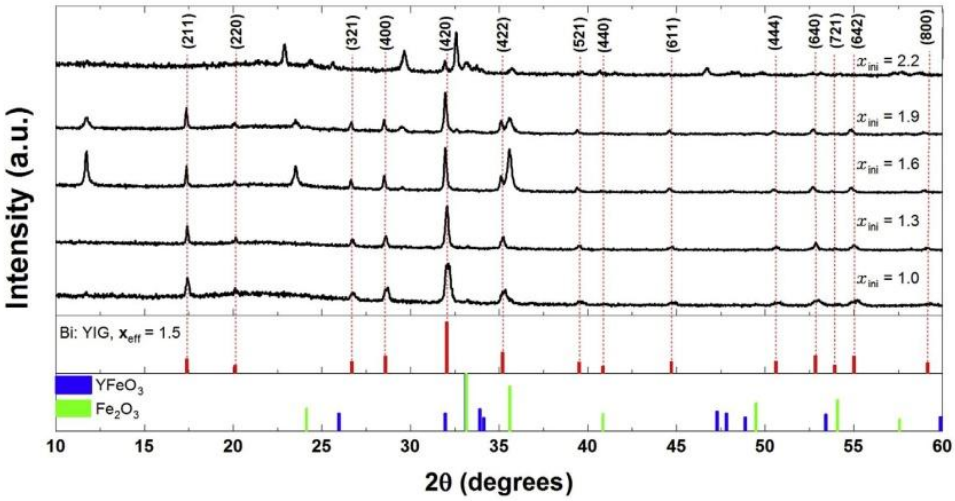

Fig. 6. XRD patterns of the Bi: YIG films with different initial amount of bismuth x_{ini}. All the samples were identically annealed at 660 °C for 400 min. At the bottom, the histograms give the tabulated positions and relative intensities of the diffraction peaks for $Bi_{1.5}Y_{1.5}Fe_5O_{12}$, $YFeO_3$, and Fe_2O_3. At the top, the indexes correspond to the $Bi_{1.5}Y_{1.5}Fe_5O_{12}$ diffraction peaks.

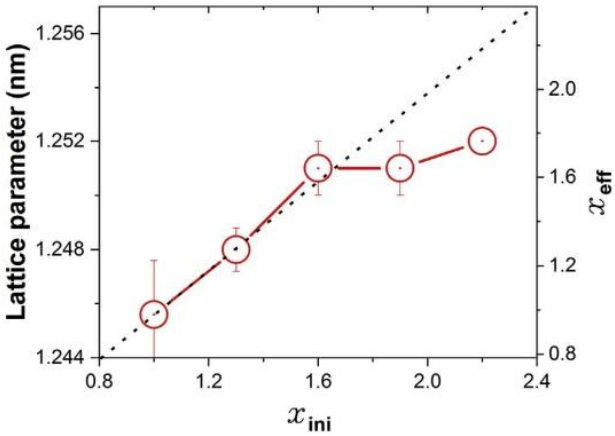

Fig. 7. Evolution of the lattice parameter of garnet with x_{ini}. The dashed line corresponds to $x_{eff} = x_{ini}$. The effective substitution x_{eff} (right) is obtained from the lattice parameter through Vegard's law.

bismuth) in the initial solution.

The absorption spectra of the samples (Fig. 1) and MO spectra at saturation (Fig. 2) show a dependency on x_{ini} similar to those observed for other Bi: YIGs prepared either by MOD or by other methods [13–15].

We investigated this dependency by a systematic study of the MO response and by varying the amounts of bismuth in the initial solution. and annealing time duration and temperature. The Faraday rotation values at saturation were measured at a wavelength of 532 nm, where the magnitude of the Faraday effect and the optical losses related to the absorption lead to a large signal to noise ratio which insures the accuracy of the optical measurements. Considering the high MO performances of the Bi: YIG samples, we assume that it is critically responsible for the Faraday rotation. As the crystallization progressed with the annealing time, the concentration of garnet increased and improved the MO response up to a saturation value that was dependent on x_{ini} and on the temperature.

Fig. 3 shows two examples of the dependence of the Faraday rotation angle on annealing time at 660 °C and 740 °C for samples with different amounts of bismuth in the initial solution. As the annealing temperature was increased above the Curie point ($T_c \approx 315$ °C), the sample was cooled to room temperature for each MO measurement. Owing to the low speed of the crystallization process compared with the high variation rate of the hot plate, no significant differences were observed between the evolution dynamics for a given annealing temperature and time either with or without cooling/heating cycles that were completed in less than 10 min.

As crystallization progressed, the MO response increased up to a saturation level that was dependent on x_{ini} and temperature. By extending the annealing time, a decay in the response occurred, which is related to degradation of the garnet. This degradation became more pronounced as the temperature further increased. This temporal evolution of the crystallization can be fitted by the solution of the system of differential equations given by equation (1) (Fig. 4):

$$\begin{cases} \frac{dN_I(t)}{dt} = -k_C(T)\cdot N_I(t) \\ \frac{dN_G(t)}{dt} = k_C(T)\cdot N_I(t) - k_D(T)\cdot N_G(t) \end{cases}, \quad (1)$$

where $N_I(t)$ and $N_G(t)$ are, respectively, the time-dependent amount of initial products and amount of crystallized garnet, and $k_C(T)$ and $k_D(T)$ are the temperature-dependent crystallization rate and garnet degradation rate, respectively. The exponential factor of the growing part of the solution is associated with the crystallization rate for different temperatures, and the exponential factor of the decreasing part is associated with the rate of decomposition. For the different initial compositions, these rates were fitted by Arrhenius' law (Fig. 5) to yield activation energies of 175 ± 5 kJ/mol for crystallization and 660 ± 20 kJ/mol for degradation. Previous measurements of the activation energies of $Bi_{1.25}Y_{1.75}Fe_5O_{12}$ powders prepared by coprecipitation process by differential scanning calorimetry [16] gave values approximately 4 times greater than those measured in this study. We suggest that this discrepancy can be explained by an intimate cation distribution confined in the initial amorphous layer. As a result, the cation diffusion energy does not have to overcome the grain size barriers.

To further investigate the crystallization process, we measured the XRD patterns [7,9,17] of samples annealed for 400 min at 660 °C, the conditions leading to the highest MO properties (Fig. 6). Bi: YIG was the only phase detected up to $x_{ini} = 1.3$. A further increase in annealing time or temperature triggered competing side reactions [6,8], causing yttrium orthoferrite ($YFeO_3$) and iron oxide (Fe_2O_3) to coexist with the homogenous Bi: YIG phase, as evidenced by the narrow peak widths. At $x_{ini} = 2.2$, the garnet phase was barely detectable.

This evolution and poor efficiency of the garnet synthesis for high bismuth concentrations raises the question of an effective substitution rate for the final product. This can be directly determined from the lattice parameter that follows Vegard's law [3,18,19] (Fig. 7). The results show that the effective substitution of yttrium by bismuth, x_{eff}, increased with x_{ini} up to 1.6 and became progressively saturated for higher values [6,18]. As the MO properties of Bi: YIGs increase with x_{eff}, this saturation limits the efficiency of the garnet. Furthermore, as the concentration decreases with the appearance of side products, the MO

properties of the Bi: YIG films also decrease. The best trade-off for the highest Faraday rotation was achieved at $x_{ini} = 1.3$ with a value of $-5°/\mu m$ at 532 nm. For comparison, the same value was obtained for garnets with the same substitution rate prepared by MOD on $Gd_3Ga_5O_{12}$, where the garnet was grown epitaxially [14]. On this substrate, a full effective bismuth substitution, $x_{eff} = 3$, was reached via the MOD process, and a Faraday rotation of $-22°/\mu m$ at 532 nm was obtained.

4. Conclusions

We have studied the crystallization of Bi: YIG films prepared on silica substrates using the MOD process by systematically varying the initial composition and annealing temperature and time. By measuring the film MO properties during the crystallization process, we were able to extract a crystallization activation energy of 175 ± 5 kJ/mol. A maximum Faraday rotation of $-5°/\mu m$ at 532 nm was obtained for a bismuth initial concentration $x_{ini} = 1.3$ after 10 h of annealing at 660 °C. The performances were limited by the maximum effective substitution of bismuth that saturated at $x_{eff} = 1.7$ and by the appearance of side products that limited the garnet concentration for high initial bismuth contents.

Declarations of interest

None.

Acknowledgements

The authors acknowledge financial support from the French National Research Agency via the project FOGAMO [grant number: ANR-16-CE08-0014-01] and the project Equipex UNION [grant number: ANR-10-EQPX-52].

References

[1] D. Lacklison, G. Scott, H. Ralph, J. Page, Garnets with high magnetooptic figures of merit in the visible region, IEEE Trans. Magn. 9 (1973) 457–460 https://doi.org/10.1109/TMAG.1973.1067670.
[2] P. Görnert, T. Aichele, A. Lorenz, R. Hergt, J. Taubert, Liquid phase epitaxy (LPE) grown Bi, Ga, Al substituted iron garnets with huge Faraday rotation for magneto-optic applications, Phys. Status Solidi A 201 (2004) 1398–1402 https://doi.org/10.1002/pssa.200304410.
[3] E. Popova, M. Deb, L. Bocher, A. Gloter, O. Stéphan, B. Warot-Fonrose, B. Berini, Y. Dumont, N. Keller, Interplay between epitaxial strain and low dimensionality effects in a ferrimagnetic oxide, J. Appl. Phys. 121 (2017) 115304 https://doi.org/10.1063/1.4978508.
[4] M. Gomi, K. Utsugi, M. Abe, RF sputtered films of Bi-substituted garnet for magneto-optical memory, IEEE Trans. Magn. 22 (1986) 1233–1235 https://doi.org/10.1109/TMAG.1986.1064475.
[5] J.L. Rehspringer, J. Bursik, D. Niznansky, A. Klarikova, Characterisation of bismuth-doped yttrium iron garnet layers prepared by sol-gel process, J. Magn. Magn. Mater. 211 (2000) 291–295 https://doi.org/10.1016/S0304-8853(99)00749-0.
[6] K. Matsumoto, K. Yamaguchi, A. Ueno, T. Fujii, Preparation of Bi-substituted YIG garnets by sol-gel synthesis and their magnetic properties, IEEE Transl. J. Magn. Jpn. 6 (1991) 15–22 https://doi.org/10.1109/TJMJ.1991.4565101.
[7] O. Galstyan, H. Lee, S. Lee, N. Yoo, J. Park, A. Babajanyan, B. Friedman, K. Lee, Effect of pre-crystallization on the preparation of thick Bi-YIG films by the metal-organic decomposition method, J. Magn. Magn. Mater. 366 (2014) 24–27 https://doi.org/10.1016/j.jmmm.2014.04.045.
[8] O. Galstyan, H. Lee, A. Babajanyan, A. Hakhoumian, B. Friedman, K. Lee, Magneto-optical visualization by Bi:YIG thin films prepared at low temperatures, J. Appl. Phys. 117 (2015) 163914 https://doi.org/10.1063/1.4918907.
[9] T. Ishibashi, T. Yoshida, T. Kobayashi, S. Ikehara, N. Shigehiro, T. Nishi, Preparation of $Y_{0.5}Bi_{2.5}Fe_5O_{12}$ films on glass substrates using magnetic iron garnet buffer layers by metal-organic decomposition method, J. Appl. Phys. 113 (2013) 17A926 https://doi.org/10.1063/1.4798480.
[10] RBNano company, http://www.rbnano.com , Accessed date: 4 April 2019.
[11] M. Deb, M. Vomir, J.L. Rehspringer, J.-Y. Bigot, Ultrafast optical control of magnetization dynamics in polycrystalline bismuth doped iron garnet thin films, Appl. Phys. Lett. 107 (2015) 252404 https://doi.org/10.1063/1.4938538.
[12] J.P. Krumme, V. Doormann, C.P. Klages, Measurement of the magnetooptic properties of bismuth-substituted iron garnet films using piezobirefringent modulation, Appl. Opt. 23 (1984) 1184–1192 https://doi.org/10.1364/AO.23.001184.
[13] J.M. Robertson, S. Wittekoek, T.J.A. Popma, P.F. Bongers, Preparation and optical properties of single crystal thin films of bismuth substituted iron garnets for magneto-optic applications, Appl. Phys. 2 (1973) 219–228 https://doi.org/10.1007/BF00889503.
[14] E. Jesenska, T. Yoshida, K. Shinozaki, T. Ishibashi, L. Beran, M. Zahradnik, R. Antos, M. Kučera, M. Veis, Optical and magneto-optical properties of Bi substituted yttrium iron garnets prepared by metal organic decomposition, Opt. Mater. Express 6 (2016) 1986–1997 https://doi.org/10.1364/OME.6.001986.
[15] S. Wittekoek, T.J.A. Popma, J.M. Robertson, P.F. Bongers, Magneto-optic spectra and the dielectric tensor elements of bismuth-substituted iron garnets at photon energies between 2.2-5.2 eV, Phys. Rev. B. 12 (1975) 2777–2788 https://doi.org/10.1103/PhysRevB.12.2777.
[16] Y.P. Fu, K.K. Lew, Crystallization behavior of $Bi_{1.25}Y_{1.75}Fe_5O_{12}$ prepared by co-precipitation process, Ceram. Int. 35 (2009) 3235–3239 https://doi.org/10.1016/j.ceramint.2009.05.038.
[17] O. Galstyan, H. Lee, J. Park, J.H. Lee, A. Babajanyan, B. Friedman, K. Lee, Influence of bismuth substitution on yttrium orthoferrite thin films preparation by the MOD method, J. Magn. Magn. Mater. 397 (2016) 310–314 https://doi.org/10.1016/j.jmmm.2015.08.112.
[18] S. Geller, H.J. Williams, G.P. Espinoza, R.C. Sherwood, M.A. Gilleo, Reduction of the preparation temperature of polycrystalline garnets by bismuth substitution, Appl. Phys. Lett. 3 (1963) 21–22 https://doi.org/10.1063/1.1753858.
[19] B. Strocka, P. Holst, W. Tolksdorf, An empirical formula for the calculation of lattice constants of oxide garnets based on substituted yttrium- and gadolinium-iron garnets, Philips J. Res. 33 (1978) 186–202.

UNIVERSITÉ DE STRASBOURG

Issatay NADINOV **ED 182**

Fonctionnalisation de fibres optiques par des grenats pour les applications magnéto-optiques

Summary

My Ph.D. thesis work is dedicated to the functionalization of an optical fiber with a bismuth-substituted yttrium/iron garnet (Bi: YIG) for magneto-optic (MO) sensing applications, using the Faraday effects. During my research, I developed an original way to perform the synthesis of garnet microcrystal directly on the core of optical fiber by Metal-Organic Decomposition (MOD) method.

I started with studying the MO and structural properties (XRD, SEM, AFM) of the material during the preparation process. The results showed a strong dependence of these properties on the temperature of annealing, duration time of the annealing and composition of the initial solution. This allowed me to refine the Bi: YIG synthesis and to find the optimal conditions to achieve the largest Faraday rotation. In addition, these studies gave me the possibility to determine the activation energy of Bi: YIG films crystallization, while calorimetric experiments (DSC, DTA) fail due to the presence of the substrate.

Presently, I am able to prepare not only the garnet thin layers but also microcrystals with 2 - 3 µm size on the core of the optical fiber. I have developed an optical fiber sensor for magnetic measurement using this functionalized fiber. The obtained results showed that magnetic fields from 100 mT down to a few µT for such fibered MO sensor can be easily detected. Moreover, the used setup allows me to make measurements of the magnetic field based not only on Faraday rotation but Faraday ellipticity. And this fact gives the opportunity to significantly simplify the detection system and open new perspective ways in magnetic field measurements.

Résumé

Mon projet de thèse est consacré à la fonctionnalisation d'une fibre optique par un grenat d'yttrium / fer substitué bismuth (Bi: YIG) pour les applications à la détection magnéto-optique (MO) utilisant l'effet Faraday. Au cours de ce travail, j'ai développé une méthode originale pour réaliser la synthèse de grenats directement à l'extrémité d'une fibre optique, préparés par la méthode de décomposition métallo-organique (MOD).

J'ai étudié les propriétés MO et les propriétés structurelles (DRX, SEM, AFM) du matériau en fonction des conditions de préparation. Les résultats ont montré une forte dépendance de ces propriétés à la température de recuit, à sa durée et à la composition de la solution initiale. Variant ces paramètres, j'ai affiné la synthèse du Bi: YIG et déterminé les conditions optimales permettant d'accéder aux rotations de Faraday maximales. De plus, ces études m'ont donné la possibilité de déterminer l'énergie d'activation de la cristallisation des films Bi: YIG, alors que les expériences colorimétriques (DSC, DTA) sont inopérantes du fait de la présence d'un substrat.

Actuellement, je suis en mesure de préparer non seulement les couches minces de grenat sur la fibre, mais également des microcristaux, dont la taille est de 2 à 3 µm, alignés précisément sur le cœur du guide optique. J'ai également développé un capteur à fibre optique pour la mesure de champ magnétique utilisant cette fibre fonctionnalisée. Les performances de ce détecteur permettent la mesure de champs magnétiques allant de 100 mT à quelques µT. De plus, la configuration utilisée me permet de mesurer le champ magnétique non seulement à partir de la rotation de Faraday, mais aussi de l'ellipticité de Faraday, ce qui permet de simplifier considérablement le système de détection et d'ouvrir de nouvelles perspectives pour la mesure du champ magnétique.